Universidade de Aveiro
Year 2011/2012

Mechanical Engineering Department

Universidad Carlos III,
Madrid
Year 2011/2012

Elder Alexandre de Sousa Hernández

Final degree project: A dynamic study of fractured shafts submitted to only gravity load

Universidade de Aveiro
Ano 2011/2012

Mechanical Engineering Department

Elder Alexandre de Sousa Hernández

Projecto de fim do grau: Estudo dinâmico de um eixo fracturado submetido apenas a carga gravítica

Final degree project: A dynamic study of fractured shafts submitted to only gravity load

Final degree project worked and defended at Universidad Carlos III, Madrid. Presented to the Universidade de Aveiro for the fulfilment of the requirements to accomplish the Master degree in Mestrado Integrado em Engenharia Mecânica, tutored by Professor Doctor Maria Belén Muñoz Abella, Titular Professor Doctor from the Mechanical Engineering Department at Universidad Carlos III, Madrid.

Project developed under the Erasmus Program at Universidad Carlos III, Madrid

To my parents, Mayra Hernández de Sousa and António Saraiva de Sousa, for the support and love they gave me.
To my sister, Miriam Nayelli de Sousa Hernández, for always being there to make me achieve my objectives.

The Jury

president

Prof. Dr. Lourdes Rubio Ruiz Aguirre
Profesora titular at Universidad Carlos III, Madrid

Prof. Patricia Manresa de Lorenzo
Profesora investigadora at Universidad Carlos III, Madrid

Prof. Dr. Shirley Garcia Castillo
Profesora ayudante at Universidad Carlos III, Madrid

Acknowledgments

To my Master degree thesis tutor from the University Carlos III of Madrid, **Profesora Doctora Maria Belén Muñoz Abella**, for having trusted me and supported me on my work during the thesis.
The teachers, students and staff of the Department of Mechanic Engineering from the University of Aveiro for providing my academic background and the perception on how to be an engineer.
To the Erasmus program.
To my host Erasmus university – Universidad of Carlos III, Madrid.

Key Words *Rotor dynamics, cracked shaft, gravity, breathing mechanism, FEM, ABAQUS, mesh*

Abstract

This work is a reflection of the investigation on the field of rotor dynamics. The study of the dynamic behaviour of a cracked shaft is important not only to predict when the failure might occur but also to know at what extent it can still work in safe conditions. The nonlinearity of this behaviour can be studied through a FEM model and can provide a breakthrough to get raw data analysis of the breathing mechanism that occurs in dynamic cracked shafts submitted only to gravity load. The study of the breathing mechanism has been one of the directions that the field of rotor dynamics uses to obtain more data for an overall analysis of a cracked shaft behaviour.

Content

Notation

Basic SI units given in parenthesis

N_c	critical speed (rad/s)
g	gravity (9,8066 m/s^2)
δ_{st}	shaft total maximum deflection
w	shaft weight (kg)
L	shaft length (m)
E	Young elastic module (Pa)
I	moment of inertia (m^4)
X	X-axis
Y	Y-axis
ϕ	Angular position (radians)

Figure content

Table Content

Chapter 1

Introduction

1.1 Motivation and objectives

In the recent three decades the field of rotor dynamics has been increasingly established as an important area in applied mechanics. This field has thrived because significant part of actual machinery in most of the industries is based on the use of a rotor. Thus it has become essential to peruse the inner workings of rotors, as well as their behaviour.

There are factors that can reduce the performance of a rotor: instabilities, cracks, material properties. Detecting and analysing cracks in order to replace flawed material has been the normal direction of study pursued by rotor dynamic. It gave the necessary tools technological and analytical to detect, replace and prevent near system failures. There are two different approaches to identify the presence of a crack in rotating structures. The first approach is based on the fact that the presence of a crack in the rotating shaft reduces the stiffness of the structure causing a reduction of the natural frequencies of the original un-cracked shaft. The other approach of crack identification rests upon the modification of the dynamic responses of the crack rotor during its rotation.

But the "system" of preventing near system failure is not reliable. Sometimes shafts that are in perfect condition and still have working life spam are just simply replaced and discarded, increasing the maintenance costs of such machinery. So in order to avoid this problem the study of the behaviour of already cracked rotating structures has been developed to a further extent.

The study of the shafts changing periodic stiffness near the fractured area proves to be an important tool to comprehend the dynamic behaviour of cracks (Al-Shudeifat and Butcher 2011)[1]. The breathing mechanism is a special feature originated by the existence of cracks in a rotating structure. The breathing mechanism basically consists in the opening and closing of the cracks during each revolution. This shifting between opening and closing creates different points of pressure between the opposing crack faces that vary according to the rotational angles (Dimarogonas 1996)[1]. To get to know better this mechanism and its relation to the shifting of stiffness to get a better and more accurate cracked rotor model, there is a need for more precise data of the stiffness values. However, as a new area of science there still is not enough information regarding this mechanism leading towards the necessity of more experimental and simulation investigation.

There are many models to analyse the nonlinearity of the crack breathing mechanism [2]. Nonetheless, in order to get the full data analysis of this mechanism, models have to be even more sophisticated. The Finite Element Method, FEM, gives a precise and reliable simulation of the shafts cracked behaviour, but due to the amount of calculus it is required for this method to be paired with a 3D FEM simulation computer programming. The computational problems within this Master degree project were solved with simulation software, the Computer-Aided-Engineering CAE/ABAQUS, that permits to model and analyse mechanical components.

The aim of this work is to study the different stress zones created by the breathing mechanism in different crack depths and rotational speed. Major objectives have been drawn to accomplish the main purpose of this research.

- Study past models and create a study model for the simulation (creation of a case study):
  - Take into account the specifications of the desired data;
  - Create models with different crack depths;
  - Establish the rotational velocity parameters;
- Simulate the models and acquire data.
- Analyse the data collected from the different case studies.
- Conclusion of the investigation.
- Future works.

1.2. Thesis organization

Chapter 1, this chapter, has the acknowledgments, motivations and objectives that led to the investigation of this work.

Chapter 2 consists of a review of the history of research done so far in the field of rotor dynamics. It contains a special part about the Finite Element Method and the program ABAQUS/CAE.

Chapter 3 develops all the model details and the background work in order to obtain them.

Chapter 4 contains the simulation data collected from the different model case study. It has a brief analysis of the data.

Chapter 5 presents a data review and general discussion.

Chapter 6 includes the future works based on the data obtained in this work.

Chapter 2

Rotor-dynamics

The rotor dynamics field is one of the applied mechanics areas that study the behaviour of dynamic structures. The provided analysis is used to investigate the behaviour of turbines, motor engines and even computer discs.

The rotating shaft is one of the main parts of all nowadays machinery. It is submitted to strong vibrations, overextending forces (torsion, bending or compressing) and in extreme conditions to working instabilities. The failure of this part can cause huge prejudice. So it is very important to study it and create boundaries of functionality and failure prevention.

Some of the reasons appointed as causes that lead to failure of shafts are: the low harmonic frequency of the material properties, excessive weight, or instabilities from the motor parts or material.

In order to have a perfectly working rotor is necessary to have study material from behaviour analysis. To know "what went wrong" and "how it went wrong" is important. Adding up this information is needed to find equilibrium between material and design conception.

2.1 Historical overview

The first documented studies in the field of rotor dynamics date back as 1896, during the industrial age. This study was written by William John Macquorn *Rankine*[3] and it was about the dynamic movement of a rotor. It was based on a simple model with two degrees of freedom that had a rigid bulk in a gyroscopic movement and an elastic spring

in a radial position, as shown in Fig.1. With this simple model it was possible to notice that under a certain angular velocity – later called whirling speed – the shaft enters into a plastic state, bending itself and starting to rotate under this new bended form. This was an important breakthrough at that time because it explained some of the system failures that occurred on steam engine machines. But it was still somehow inconclusive mainly because it didn't foresee the Coriolis acceleration and its effects on the gyroscopic movements of a rotor.

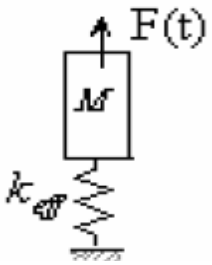

Figure 2.1 - Rankine Model [4]

Using the Rankine model, the researchers at the time begin to expand the field of rotor dynamics. They started to compile more data and increasing the rotor angular velocity until they reach a barrier in velocities – the first critical velocity.

The theoretical and experimental studies of Laval that even led to the building of an experimental prototype that could reach supercritical velocities showed that it was able to cross the critical velocity and maintain the operation of rotors. It helped to conclude that a rotor can have a huge variety of critical velocities in accordance to its natural frequencies (when the rotor is fully stopped) [4].

In 1894, Dunkerley derived for the first time a way to calculate the lower supercritical velocities of a rotor – Dunkerley method. In his work we can paraphrase the following statement [4].

"It is well known that every shaft, however nearly balanced, when driven at a particular speed, bends, and, unless the amount of deflection is limited, might even break, although at higher speeds the shaft again runs true. This particular speed or "critical speed" depends on the manner in which the shaft is supported, its size and modulus of elasticity, and the sizes, weights, and positions of any pulleys it carries."

But the strong influence of Rankine works and a certain misconception regarding "whirling spin" and "critical velocity" concepts, led to a stall in the development and application of super rotor until late 1916.

In 1916, Kerr showed that there existed a second supercritical velocity and shatters this way the stalemate. In 1921, Holtz formulated through calculation an approximate way to obtain the natural frequencies [4].

The first real study model for rotor dynamics was introduced in 1895 by Foppl. It was a model based on a central disc (with mass) on a shaft without any damping, as illustrated in Fig. 2.2. His study was later on published on a low rate German engineering newspaper making it impossible to be right away known in the rotor dynamics community. Later on his studies helped to develop a formula to calculate vibrational instabilities [4].

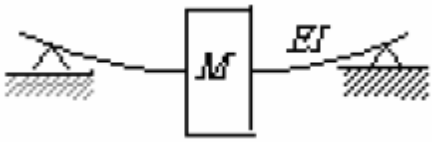

Figure 2.2 - Foppl model [4]

In 1919, Jeffcott [5] presented a similar model as the Foppl model but with damping. He published his work in a renowned English newspaper and so was credited by his discovery. Although is a simplified model it allows a study important parameters like the study of super critic velocities, gyroscopic movement, instability caused by damping. It gave an impressive leap in getting to know the behaviour of rotors under huge stresses.

Stodola [6], in 1924, published a compendium of all that was achieved until then in the rotor dynamics field. In his book he takes into approach the dynamics of the shaft with discs, the dynamics of rotors without gyroscopic effect, 2^{nd} degree of resonance caused by gravity, rotor imbalance and some methods to calculate critical velocities (in this field he demonstrates graphically that the super critical velocities are stable because of the Coriolis acceleration that can lead to the gyroscopic effect).

After determining the possibility of reaching the first critical velocity, the researchers started to verify that a great deal of cinematic energy was being stored in the rotor shaft leading to intense internal vibrations of the parts. This kind of instability was closely studied by Kimbal and Newark in 1924 that explained this effect as internal damping between parts. Newirk and Taylor described it as a nonlinear instability derived by the oil whip. Other researchers like Robertson (1959) studied the rotor instabilities, Baker (1933) studied the vibration between the stator and the rotor, Kapitsa (1939) studied probable instabilities caused by friction between the couplings and the shaft. Other

kinds of instabilities were later studied like the stiffness of couplings, or even the fluid flow in a gas turbine [4].

In the 50's and 60's, during the Cold War was developed a considerable impulse in the rotor dynamics field. The necessity to improve rotors became a necessity in order to obtain the lead military (war machines, and plane turbine) or civil (power generators).

Bishop (1959), Bishop and Gladwell (1959), Bishop and Parkinson (1965), Dimentberg (1961) and Tondl (1965) Bishop (1959) published their works on instability and calibration of continuous rotors. Eshleman and Banks obtained the general equations of movement; these equations could explain the rotational inertia, the deformation and the gyroscopic movement [4].

As light weight rotors that could reach high velocities begin to being developed there was a growing concern regarding the appearance of sub-harmonic resonance. Yamamoto in 1955 studied these kinds of waves [4].

Another problem was the impossibility to apply the Jeffcott model to study the gas turbines in planes. This problem impeded to calculate the natural frequencies and the response do instabilities or deformation. The vibrational torsional method suggested by Holzer, in 1921, could resolve part of the problem. But there was still the need to obtain a more general equation.

Prohl, in 1945, presented in his work a fair approach about evaluation of super-critic velocities in turbine shafts. Myklestd, in the same year, suggested a similar approximation about obtaining natural frequencies in stationary structures. Both Myklestd and Prohl formulation later provided the basis in the 60's to create a wider method – the Transfer Method Matrix (TMN). This formulation is still very much used nowadays in the industry that works with rotors [4].

Another method that later appeared and would soon begin to be the ruling method in structure analysis is the Finite Element Method.

2.2 Fracture study in rotor-dynamics

The investigation in rotor fracture began in the 60's, when steam engine rotor began to show fractures while still operating. There was a study about the behavior of rotors submitted to failure tests or even the simulation of impending failure cracks. These

kinds of studies proved to be an important tool in order to prevent them to occur – prognostic technics and technology to monitor rotor dynamic systems.

Gash (1976) and Okah-Ave (1976) [7], analysed the vibration in nonlinear rigid systems with breathing (open-close) mechanism. They proved that instable regions appear and disappear according to when the rotor is submitted to near super-critic velocities and is dependable to the direction of the rotor instability.

Edwards, in 1998, published his works regarding the state of art in all prognostic technics in rotor dynamics. He concluded that the most important factor that leads to failure was mass disequilibrium, shaft curvature and cracked shafts [8].

Later, in 1999, Pusey and Roemer published a study about diagnosis, monitoring and flaws regarding the prognostic techniques applied in rotor dynamics of high performance [8].

Today there is a great challenge to improve the prognostic technics. Over the years the enhancements and breakthroughs in technology provided numerous ways of measuring and collecting data. But there is lacking a more confident way to read all the information obtained and so the technique is still yet to be perfected.

2.3 The finite element method

The Finite Element Method, FEM, is a numeric procedure that can be used to obtain solutions to a great number of engineering and physics problems. It can goes from stress analysis, to thermodynamics transfer, electromagnetism and fluid flux [1].

2.3.1 F.E.M. History

This method was developed in the last century. The first similar use of this method was made by Richard Courant in 1943, using the Ritz method of analytical numeric minimizations of variables calculated solutions to a vibrational problem.

In the early 50's Olgierd Zienkiewicz came up with a new method based upon the works of Alexander Hernnikoff (1941) and Courant (1943). This new method was developed by creating a mesh into a structure and after words its discretization from a

continuous domain into finite discreet sub-domain of elements. This new method was called Finite Element Method – FEM [9].

Later on Turner, Clough, Martin and Topp published in 1956 their work on stiffness and deformation of complex structures. This was made using a discretization of structure into small linear type bar elements. It used a new system of equation to calculate the equilibrium equation of the structure links (known as nods) of the elements. The formulation is:

$$\vec{f} = k \cdot \vec{u} \tag{2.1}$$

Here, "u" represents the unknown quantities of nods displacements. "f" represents the forces that are applied in the nods and "k" refers to the stiffness matrix.

Although this method was used to calculate simple geometries or applying simplified surfaced geometries using bars. There still remained a greater problem that was to calculate complex geometries, continuous structures (like volumes and surfaces) and the great challenge that was to solve all the equations generated by the multiple nods. That was basically what the industry demanded to be achieved.

The first step forwards on revitalizing this method was given in the aerospace field. In 1956, the National Aeronautics and Space Administration-NASA developed its first computer and computer program NASTRAN to calculate space engineer problems.

During the 60's calculus centres thrived intensively around the world and so did the first commercial program based on FEM surfaced. This method was keenly adopted by most industries and its theory begun to be taught at universities.

In the 70's there was a huge leap in FEM studies. The first mathematical bases were established for FEM. But still only aerospace, aeronautics, automobile, military and some renamed universities had access to FEM computer programs.

In the 80's when personal computer became a reality so did the commercial version of FEM, and lately begun to be more generalized. This method expanded its use in the behavior analysis of fracture, plasticity and even in error analysis.

Nowadays the FEM method is used in par as the Matricidal Method. Programs tend to use both methods, in order to diminish the high processing request of very long consuming time calculations. As computer processing is increasing so highly, the FEM method achieves higher precision in its calculus and can give an almost exact solution to the many types of analysis.

2.3.2 The method

The method bases itself in creating a mesh, which consists in a finite number of elements that take the properties of the material of the part it represents. These elements have some links that unify them; these links are known as nods. The behaviour of each element is defined by the behaviour of the nods, the "interpolation function" or the "form function" represents this behaviour. This set of functions give in an approximate way the displacements or tensions that occur. The system formed by these lineal equations is known as the stiffness matrix system.

To make some order in this complex method there are some steps [11][12] that need to be followed:

1) Pre-processing step – in this step the model is prepared. The model geometry is drawn. The geometry is imbued with the material properties. Loads and border controls are added. And the program generates a mesh that can fit the geometry.
2) Resolution step – in this step the program calculates all the variables, defined unknowns and assumptions that each nod has (the number of nods will determine the number of equations and its solution that need to be calculated). Here we have the type of calculation to be done (stress, pressure, temperature). Define the number of steps and time intervals. Applying loads to the nods, form functions, building the stiffness matrix, solving the equations and obtaining a solution.
3) Post process step – In this step we can obtain all the graphic representation of the solutions and indirect solutions of the model. We can even obtain in some program the full simulation of the problem.

2.4 ABAQUS program

ABAQUS program is a software application for Finite Element analysis and Computer Aided Engineering. It was developed in 1978 by Hibbit, Karlsson & Sorensen, Inc. It has been widely used to solve complex engineering problems, ranging from fracture mechanics, material resistance, heat transfer and other engineering utilities [13].

ABAQUS program is divided into 4 modules:

- ABAQUS/Standard – The general problem resolution. It can take on all the analysis types except dynamic analysis.
- ABAQUS/explicit – The dynamic problem resolution. It is a very powerful and efficient computing tool able to take on big and complex models. It can be used to semi-static analysis.
- ABAQUS/CAE – The interactive model that can mesh using the FEM.
- ABAQUS/Viewer – The final virtual simulation of the problem.

2.4.1 ABAQUS units

ABAQUS does not have any built-in system of units. So basically, we must input all introduced data in consistent units. It is shown in Table 2.1 some common systems of consistent units.

Table 2.1 – ABAQUS working units

Quantity	SI	SI (mm)	US Unit (ft)	US Unit (inch)
Length	m	mm	ft	in
Force	N	N	lbf	lbf
Mass	kg	tonne (10^3 kg)	slug	lbf s^2 /in
Time	s	s	s	S
Stress	Pa (N/m^2)	MPa (N/mm^2)	lbf/ft^2	psi (lbf/in^2)
Energy	J	mJ (10^{-3} J)	ft lbf	in lbf
Density	kg/m^3	$tonne/mm^3$	$slug/ft^3$	lbf s^2 /in^4

For other depended parameters we have chosen consistent units for example velocity (m/s) or stiffness N/m^2 (Pa).

2.4.2. Processing steps

The numerical program has followed the same processing steps as the method on which it was based: pre-process step, resolution step and post process step.

The pre-processing step, in ABAQUS program, was constructed by the following walkthrough [14].

- Geometry – this is by all means the first thing to be done. Sketching up the geometries – parts.
- Material – creating the material properties and later assigning to the sections of the parts.
- Parts and assembly – putting into position and assembling all the sketched parts.
- Initial conditions – assigning all the initial conditions of the parts. Constraints, reference points, degrees of freedom.
- Boundary Conditions – Movement restrictions, displacement values, rotational values and symmetry conditions.
- Interactions – collision between parts.
- Loads – adding external loads to the piece, for example gravity.
- Output – assigning the type and time of analysis to be made.
- Meshing – choosing the parts to mesh and the type of mesh.

Afterwards we have concluded these laborious steps; we submitted the job for analysis – resolution step. This is an internal process of ABAQUS.

Then finally we arrived to the post process, where we can visualize the results (the odb. files) and get the behaviour analysis. We can obtain simulation viewer, data output files, graphics and result tables.

Chapter 3

FEM Model

In this chapter the modelling of the rotor system is described; all the assumptions made in order to obtain a final model are presented and demonstrated. From choosing a base model, geometry assumptions, crack design, to the final meshed model. This chapter is an overview of the pre-process in ABAQUS programming.

3.1 The Jeffcott model

The Jeffcott model is the most used and studied model in the field of rotor dynamics.
The extended Jeffcott rotor analytical model[15] with instability and a crack is the type of model which this investigation will be based upon recurring ABAQUS simulation program.
This analytical type of model has the following properties:

- A shaft that is flexible, uniform and weightless. The shaft doesn't have any misalignments.
- Transversal crack at the half of the shaft length.
- A rigid mass disc at the half of the shaft length.
- Two identical couplings at the shaft end.

3.2 Adapting the model

Some adaptations to the original Jeffcott model had to be done in order to obtain the appropriate ABAQUS model.

1. The shaft will maintain the original properties. The flexibility and the material uniformity will be maintained. But the rigid disk will be discarded and the shaft will have its own weight.
2. The transversal crack will still be in the middle of the shaft length and will vary from 50% of the Radius, 75% of the Radius and 90% of the Radius.
3. The couplings will not be considered in this work. Only the distance of were the rotation should be placed will be accounted for.

3.3 Defining the geometry

3.3.1. Shaft

As said at the chapter 2, the ABAQUS program does not have defined units. So the units worked on are the SI units in order to obtain final balanced results. The shaft has the following sketching properties:

Table 3.2 – Shaft geometric properties

	Real Measurements	**ABAQUS units**
Length	90 cm	0.9 (m)
Radius	1 cm	0.01 (m)

3.3.2. Material

The material properties are taken from a set of experimental steel cylinders. The properties of this cylinder are given in table 3.2.

Table 3.3 – Shaft material properties

	ABAQUS units
Mass density	2840 (kg/m3)
Young Modulus	7.25E10 (Pa)
Poisson Ratio	0.33

Applying the geometric and material properties the basic model of the shaft is obtained, figure 3.3.

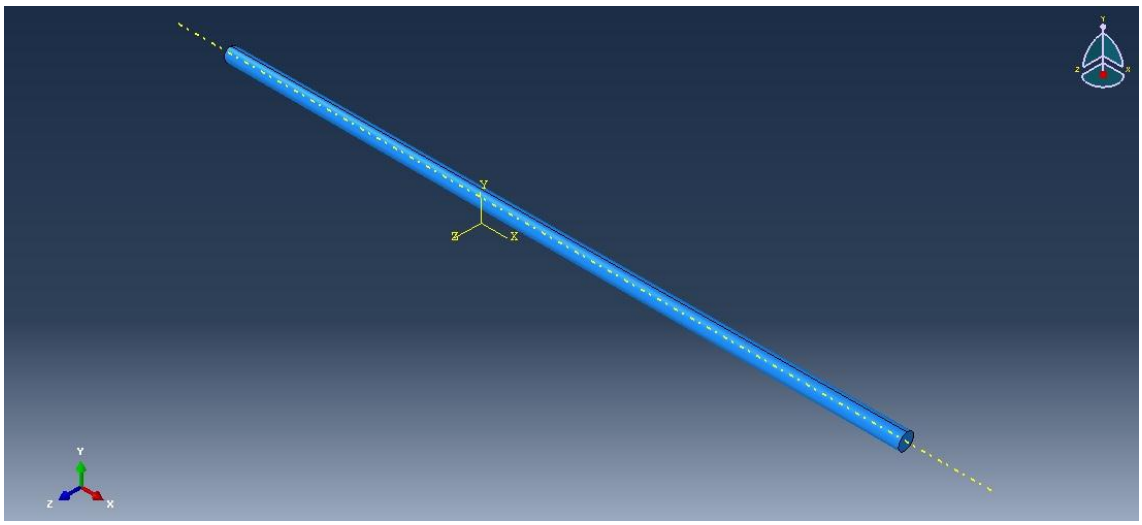

Figure 3.3 - Cylindrical rod

3.3. Couplings and rotation

In many rotor dynamics studies the position of the coupling is always taking into account. The coupling can have the effect to cause different types of imbalance in the rotating shaft.

3.5.1. Constraints

In this simulation, due to computational cost, we decided to avoid the adverse effects of coupling by not taking them into account.

To avoid creating couplings unbalance added to the rotation mechanism two reference points are assigned on which the shaft will turnabout and other two reference points will give the shafts angular velocity. In order to do that it is need to assign to them constraints to tie them to the shafts ends and border conditions.

The two reference points on which the shaft will turnabout are reference point 1 and reference point 2. The constraint applied to them will tie them to the two shaft ends faces. As seen in Fig.3.4 these points don't have any degrees of freedom in relation to the shaft.

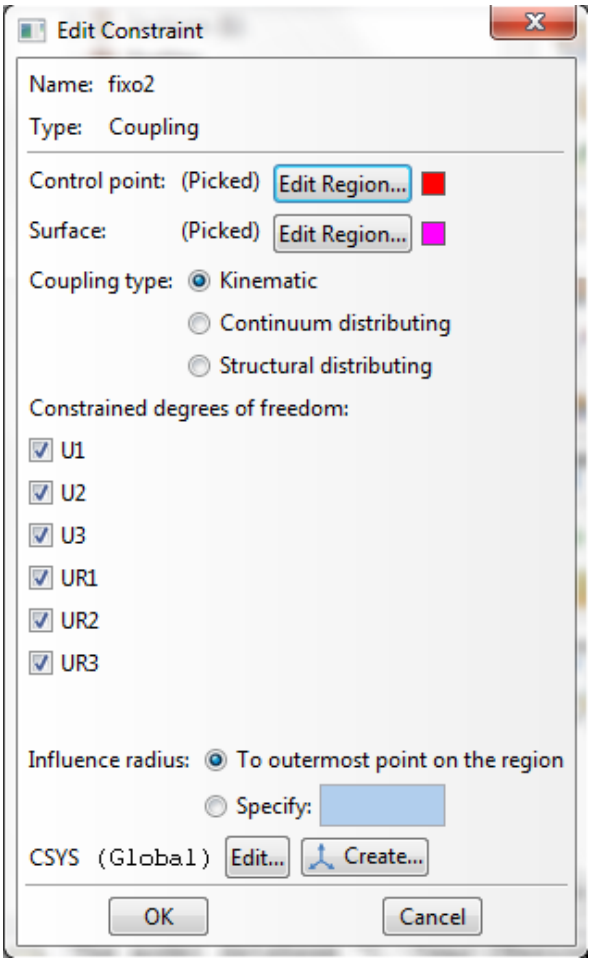

Figure 3.4 - Reference Point 1 and 2 constraint editing

The Boundary conditions of reference point 1 and reference point 2 have to be in accordance to the role they play. The type has to be a Displacement/ Rotation and managing the shafts degrees of freedom, as seen in figure 3.5.

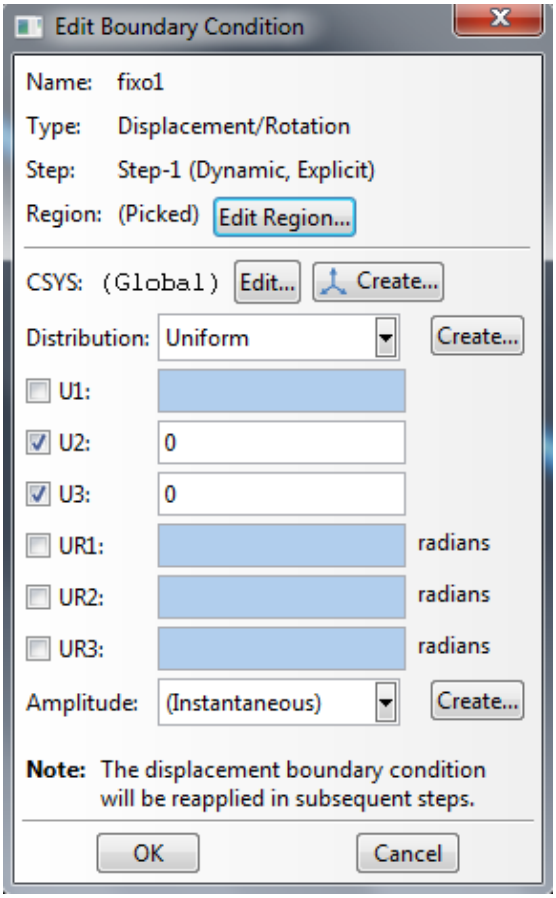

Figure 3.5 - Reference point 1 and 2 Boundary conditions editing

Other reference points are added to work as angular velocity couplings. Reference point 3 and reference 4 will behave as such. The constraints applied to them will be the same as seen in fig. 3.1 and to the two shaft ends faces. The Boundary condition will be a velocity/angular velocity type. The angular velocity is applied in the VR1 direction, as seen in fig. 3.6.

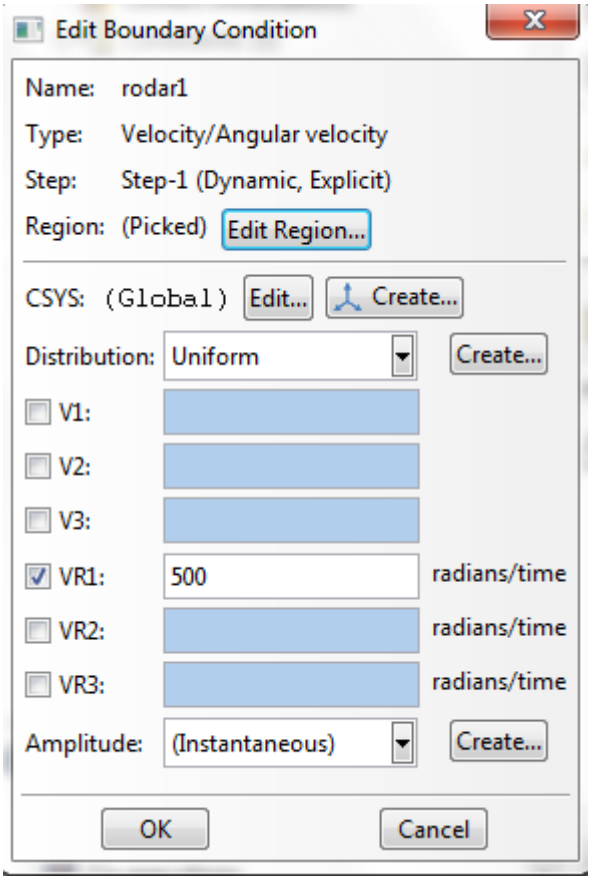

Figure 3.6 - Reference points 3 and 4 boundary condition editing

Some previous studies are done to know if the position of the reference point has some effects on the final results. We can see the results of the compare in the following subchapter.

3.5.2 Placement of reference points with rotating behaviour

An important aspect of the dimensioning of the selected model is achieving a reasonable placement of the reference point that will behave as the angular velocity engine.
As past investigations demonstrated, the couplings that input the angular motion to the shafts create instabilities that affect the natural harmonic resonance of the shaft.
In the model, we are trying to reduce the effects of the unbalance derived from rotation so in order to focus just the main objectives. A brief analysis was made in order to study of the influence of the rotating reference points. As said before, there are two reference

points, reference point 3 and reference point 4, that will give the model the angular velocity each one is going to be applied to the shaft –X and +X shaft end. Under the presumption that a higher unbalance may generate higher stress in the fracture area we build the study on that.

Using two models with reference points at different distances from the shaft end is achievable course to study the unbalance provoked. The properties of the model are:

- Model A, has a distance of the reference points in relation to the shaft face: X=0 and –X=0; Model B, has a distance of the reference points in relation to the shaft face X=0, 05 and –X=0, 05.
- Both models have a fracture of 50% of the Radius and an angular velocity of 500 rad/s.
- Both models have a hexahedral mesh with a seed instance of 0, 0245 with a maximum deviation of 0, 01.
- We use 9 nodes from different areas of the fracture to do the comparison.

Afterwards, the same local node stress in the fracture area of each model was compared using a statistical tool. We have used the following statistical formula,

$$\partial = \frac{nodal\ value\ of\ model\ B - nodal\ value\ of\ model\ A}{mean(nodal\ value\ of\ model\ B; nodal\ value\ of\ model\ A)} \quad (3.1)$$

Where,

$$\begin{cases} if\ 2 \geq \partial > 0\ nodal\ B\ has\ the\ higher\ stress\ value \\ if\ \partial = 0\ nodal\ B\ and\ A\ have\ the\ same\ stress\ value \\ if\ -2 \leq \partial < 0\ nodal\ A\ has\ the\ higher\ stress\ value \end{cases}$$

Knowing that each node has 20 values during the time interval of one second we compare each value from model A and model B. After we do the mean of each compared values and apply the same above property. The results given from this investigation are in the following table 3.3.

Table 3.4

	+z nodes	**Central nodes**	**-z nodes**
Border fracture	1,63E+00	4,00E-01	-1,14E+00
Mid fracture	-3,21E-01	1,16E-01	1,47E+00
Near fracture line	-1,31E+00	-4,93E-01	6,26E-01

Using the values in table 3.4, we have obtained the mean of the positive values and a mean of the negative values, table 3.5.

Table 3.5

Mean of table positive values	**0,8572**
Mean of table negative values	-0,816

Basically the values are very close meaning that both models may register different nodal values but in the overall study of stresses applied on the fracture area the values are basically the same. So coming to the conclusion that the distance of the reference point can have a slight effect on a singular node results but in the overall network of nodal values the changes are the similar.

Into the creation of this work final study model, the distance of the reference points is allocated to X=0, 05 and -X= 0,05 distant from the shaft ends.

As final conclusion to this study, the position of the reference point does not have impact in the results of the overall study.

In the model the distance of these reference points are 10 mm distant from the shaft end.

3.4. Rotation parameters

Each model will be submitted to analysis with two predefined angular velocities:

i) 500 radians/s and,

ii) 1000 radian/s.

The reason for choosing these angular velocities is due to 1st critical velocity. To obtain the value of the 1st critical velocity for a shaft with these material properties it is calculated using the Rayleigh-Ritz method [16].

The Rayleigh-Ritz method is an approximation to calculate the first natural frequency of vibration that is considered to be equal to the rotational critical speed. The following equation will be used to calculate the 1st critical speed of a rotating shaft.

$$Nc = \sqrt{\frac{5}{4} \cdot \frac{g}{\delta_{st}}}\ rad/s \qquad (3.2)$$

Where:

- g is the gravity acceleration which is valued 9,8066 m/s^2.
- δ_{st} is the shaft total maximum static deflection.

To calculate the maximum static deflection on the shaft without any load it was used the following equation,

$$\delta_{stl} = \frac{5 \cdot w \cdot L^3}{384 \cdot E \cdot I}\ s^{-2} \tag{3.3}$$

- w is the shaft weight, obtained through the density and shaft volume eq. (3.3).

$$w = d \cdot V = d \cdot (\pi \cdot R^2 \cdot L) \tag{3.4}$$

$$\Leftrightarrow w = 2840 \left(\frac{kg}{m^3}\right) \cdot \pi \cdot 0{,}01^2(m^2) \cdot 0{,}89(m) \Leftrightarrow$$

$$\Leftrightarrow w = 0{,}794\ kg$$

- L is the shaft length, taken as 0,89 m;
- E is the Young elastic module, which for the current shaft material has the value of 7,25x10^{10} Pa;
- I is the shaft moment of inertia, with the value 7,85x10^{-9} m^4.

$$\delta_{stl} = \frac{5 \cdot 0{,}794(kg) \cdot 0{,}89^3(m^3)}{384 \cdot 7{,}25x10^{10}\left(\frac{kg}{m \cdot s^2}\right) \cdot 7{,}85x10^{-9}(m^4)} \tag{3.5}$$

$$\delta_{stl} = 1{,}28x10^{-5}\ \ s^{-2}$$

To calculate the 1st critical speed of the rotating shaft,

$$Nc = \sqrt{\frac{5}{4} \cdot \frac{9{,}8066\ (kg \cdot \frac{m}{s^2})}{1{,}28x10^{-5}\ \ (s^{-2})}} \tag{3.6}$$

$$Nc = 978{,}6\ rad/s$$

So, under these circumstances, the study of the shaft behaviour is focused before and after the critical speed.

3.7 Fracture

The main reason of this work is to study the instability derived by a fracture in the beam.

But there are a numerous kinds of fracture and to problem is how to achieve a similar model that can simulate the behaviour of a fracture.

There are different types of fracture that occur on beams, the ductile fracture and the brittle fracture [17].

3.7.1 Ductile fracture

First we have the ductile fracture that occurs normally in high tenacity materials (pure materials).

This kind of "fracture" reduces by plastic deformation the hardened part of the material into a point or line called the Chisel Edge. This reduction of the area of material causes a type of fracture with its own characteristics and can then lead to the rupture of the element. For this kind of fracture a very high energy is needed to breakdown the metallic links so it is a much appreciated property.

3.7.2 Brittle fracture

This kind of fracture occurs with little or any plastic deformation prior. Metallic materials with high hardness are considered weak and have high risk to this kind of fractures to occur.

Major factors that can lead to this type of fracture are a high concentration of localized tensions, tensions in the elastic limit or high temperatures.

In this kind of fracture, the cracks run perpendicular to where the tension is applied leaving an almost flat surface with the patterns of propagation. Steels for example have V-shaped patterns pointing to the origin of the crack.

There are two kinds of Brittle fracture, Trans granular Fracture and Inter granular Fracture.

In the Trans granular Fracture the crack travels through the grains of material structure. The crack changes direction because of the different atomic orientations in each grain and the path with least resistance. In this fracture the cracked surface is bumpier.
In the Inter granular Fracture the path taken by the cracks is near the borders of the grain. The main reason is because the phase between grains is very weak and brittle.

3.7.3 Shaft fracture

In this case scenario the shaft is submitted to a rotation and flexile force (weight). The type of fracture is stationary meaning that it will maintain specific periphery localization.
In rotating shafts the periphery points are under specific stresses and are very responsive to unbalance that is created. Other issue is that the rotation causes the fracture to point out the direction of the rotation.
This kind of fracture is normally modelled two ways:

- The first case we have a plane front of fracture (straight line), figure 3.7.
- The second case is the elliptic front fracture, figure 3.7.

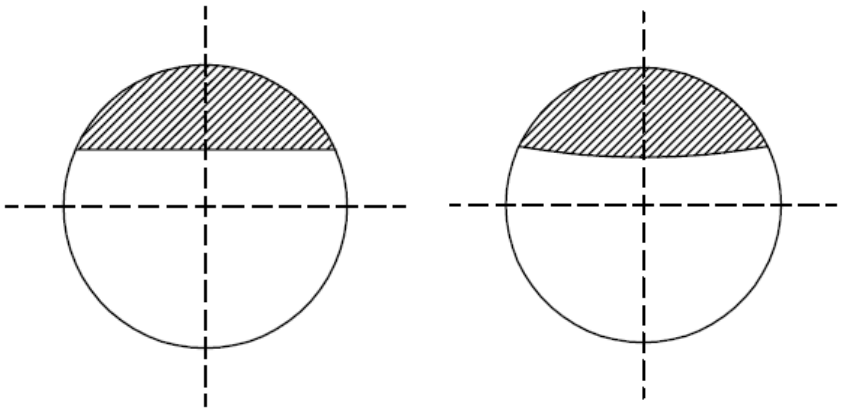

Figure 3.7 – Straight line fracture and Elliptic front fracture

In this type of study the first case is normally most used [15]. It is easier to manage in the model simulation and can give a fair proximate results but not as precise as the elliptic front fracture.
This work will analyse 3 types of fractures:

- 50% of the Radius fracture;
- 75% of the Radius fracture;
- 90% of the Radius fracture.

3.8 Adding the fracture to the model

In order to add the behaviour of a fracture into the shaft simulation it was remodelled the initial model.

Assuming that is a mid-transversal crack, it was added the behaviour of the rough contact between the two faces of the fractured part, figure 3.8. To manage that, it was divided the shaft into two equal parts and assembled with specific constraints during the Assembly step.

In the non-fractured face of the half-shaft it was unified them to behave like one shaft. To that to happen it was applied a "Tie" constraint, figure 3.9.

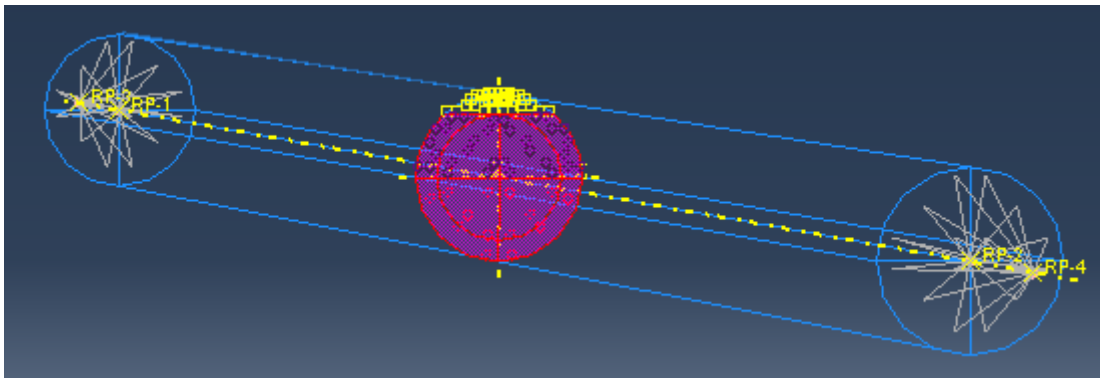

Figure 3.8 – Unified area highlighted in purple

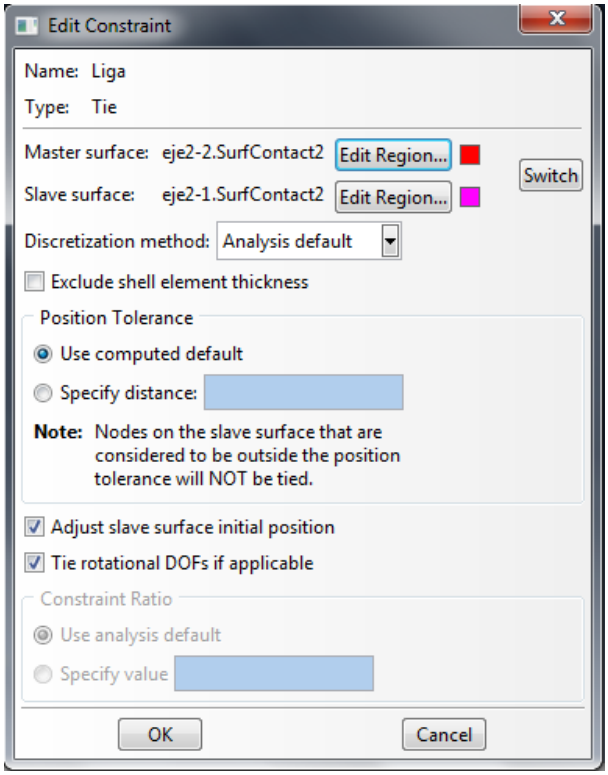

Figure 3.9 – Constraints edition

In the fractured area, figure 3.10, it was assigned a different kind of interaction, figure 3.11.

The contact between the two fractured areas had to behave like a "Rough" contact. It was added the following mechanical properties:

The tangential behaviour –Friction formulation: **"Rough"**

The normal behaviour – Pressure-over closure: **"Hard Contact**"

Constraint enforcement method: **"Default"**

Allow separation after contact: **checked**

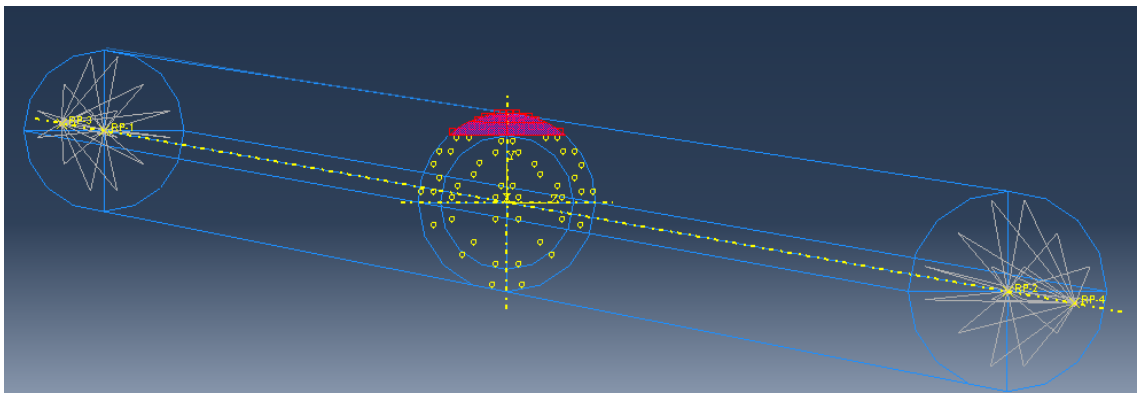

Figure 3.10 – Fracture area highlighted in purple

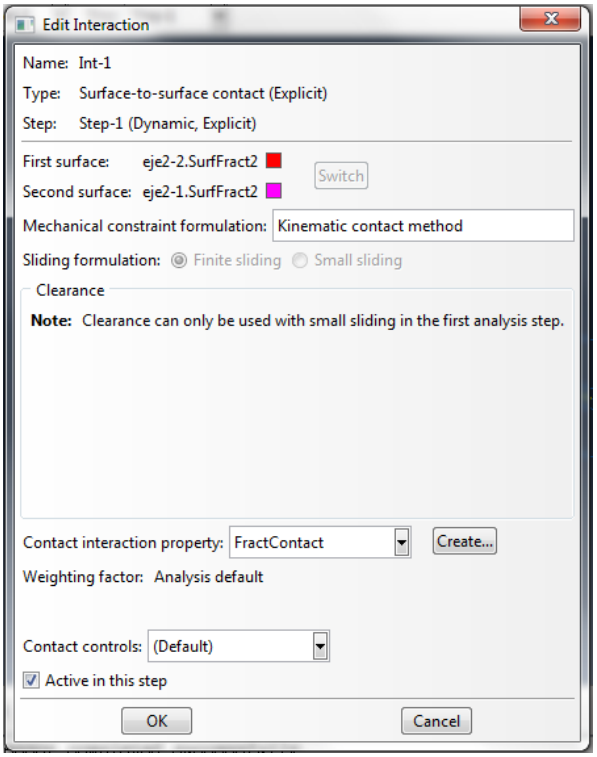

Figure 3.11 – Interaction edition

3.9 Adding the gravity force

The gravity force plays a major role in the opening and closing of the shaft crack.

On ABAQUS we have added the gravity as a Load throughout the whole model. The considered gravity value is 9, 8066 in the Y axis. This value is positive since in the case studies the shaft begins in an "Open" position.

The expected weight of the shaft is 7, 56 N.

3.10 Meshing

An important issue in working with ABAQUS simulation is to create an appropriate mesh in the model. It is seen as an important aspect for investigators to get a mesh that outputs accurate results in less time possible. To many it is an "art or a science" to create a functional and working mesh, it is achievable by studying other successful models or trial and error [18].

In a simple overview of the meshing problem it is needed to take into account that:

- A higher level of meshing can layer the geometry accurately.
- A higher level of meshing generates more proximate and reliable results.
- An increase of elements demands a higher processing potency and time.
- A higher or a lower level of meshing can create errors in the analysis step (for example overlapping elements, element distortion).

So basically the solution time, convergence and accuracy of the results of the simulation rely highly on the mesh quality.

3.10.1 Types of meshes

The ABAQUS program offers a variety of meshing techniques [14]. Types of meshes:

- Hexahedral mesh;
- Hexahedral dominated mesh;
- Tetrahedral mesh TET4;
- Wedge;

The wedge type mesh is basically a type of geometrical meshing that ABAQUS has available. It uses a known geometry by ABAQUS and uses quadratic hexahedral or tetrahedral mesh to try to approximate the shape of the model. This type of meshing is not available in a Dynamic Explicit analysis.

So mainly there is only the option between **tetrahedral mesh** and **hexahedral mesh**. In the geometric order parameter there is available between linear or quadratic.

3.10.1.1 Choosing the appropriate grid type

The **hexahedral mesh** is the most commonly used because of its benefits. It has can give a higher accuracy of the solution because of the low truncation error (*see Annex*). To give a better approximation of the experimental results the geometry must consist of structured hexahedral mesh and the mesh must be aligned with the flow direction. Distorted cells occur frequently on other meshes than the hexahedral mesh and can lead to a harm convergence, leading to solution divergence due to large source terms.

The downfall of this mesh can be for complex geometries this type of mesh can be high time consuming or even impossible. Other problem in this meshing type resides in the computational expense. In order to achieve a good meshing technic, it is important to work out the model in order to apply an able mesh in the flow direction.

The **tetrahedral mesh** can be quite helpful in order to obtain a good optimization of the geometric shape. It consists of the most basic meshing element the first-order four-node tetrahedron, or TET4. And because of the tetrahedral element it generates it allows a high degree of automatized process and the clustering of the cells in the desired area of study. It provides a good response and excellent elemental stabilization.

But for more complex shapes the computing is highly increased and therefore this mesh type loses the advantage of being an automatic meshing.

Other important aspect to take into account using the tetrahedral mesh is the numerical diffusion derived from the truncation error of this mesh type (see Annex).

3.11 Meshing the model

The model is going to work in an "**Explicit step**", so the meshing Element type has to be changed in order to be able to work under those conditions. The rest was left into default settings. The **geometric order** of the mesh was linear for both mesh types. The settings can be seen in fig 3.12.

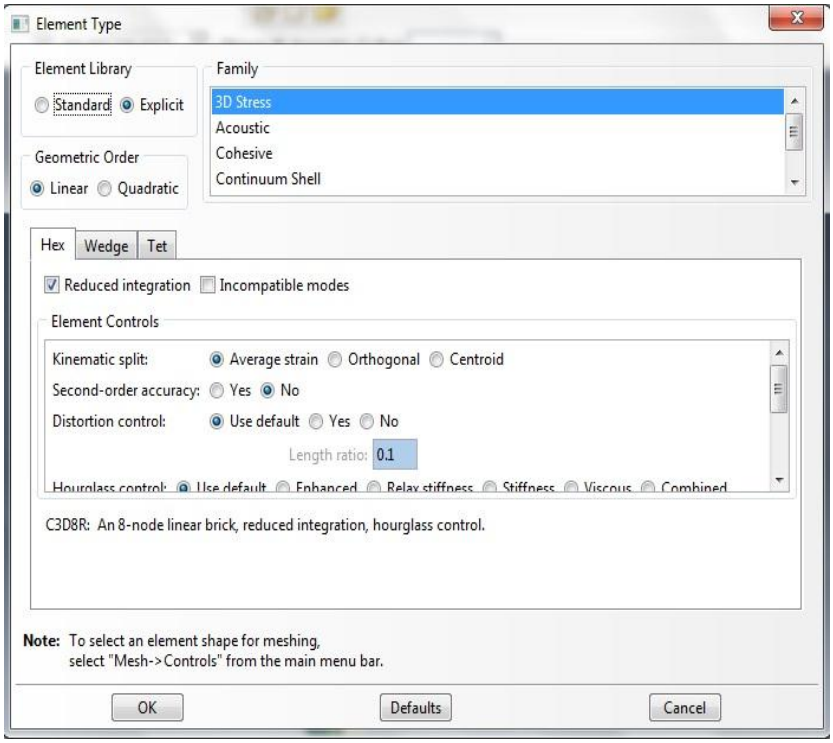

Figure 3.12 – Mesh controls

3.12 Partitioning the model

Partitioning the model plays a major role to improve calculus performance, increase speed, the creation of a path for the mesh technique and to establish the desired nodes of study [19]. The application of partitioning on the model became more refined after identifying the errors, computer loops and the results given after each job submitted for simulation. The final model had 3 types of partitioning.

- Without any partitioning, as shown in fig.3.13 and fig.3.14

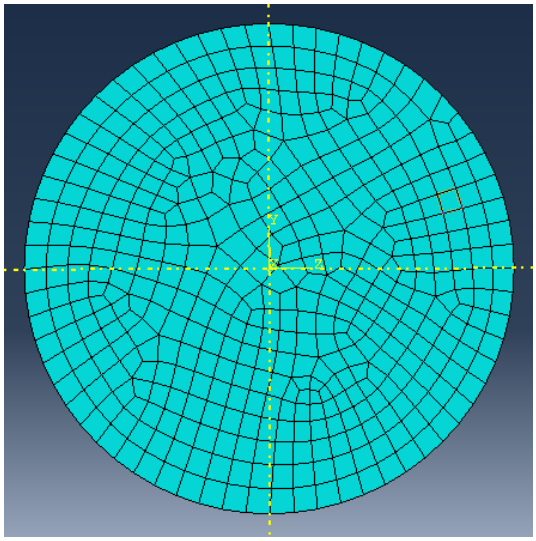

Figure 3.13 - Model with 50% Radius fracture meshed with hexahedral mesh without any partitioning

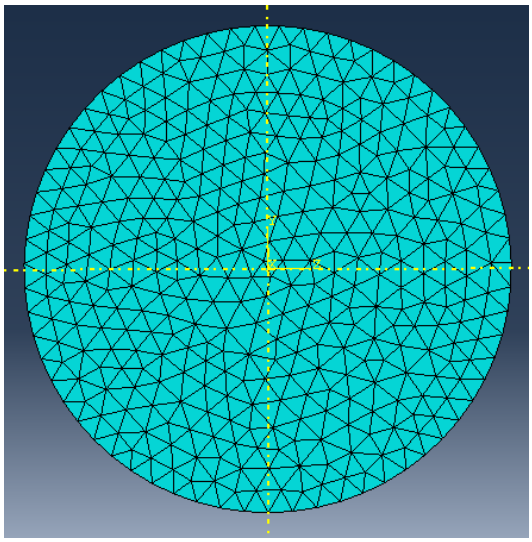

Figure 3.14 - Model with 50% Radius fracture meshed with tetrahedral mesh without any partitioning

- **Partition A**, the model was partitioned into quarters in order to create some node uniformity, fig. 3.15 and fig. 3.16.

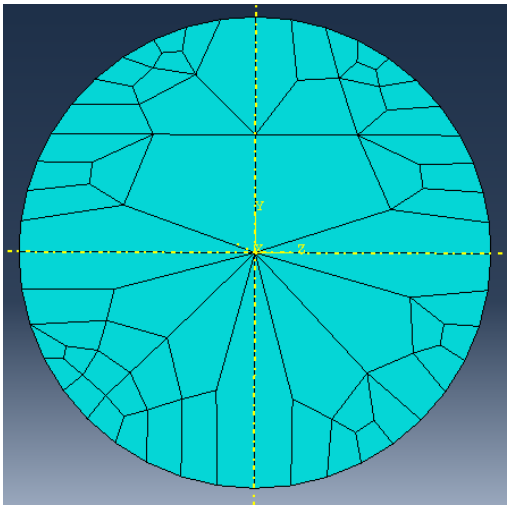

Figure 3.15 - Model with 50% Radius fracture meshed with hexahedral mesh with cross section partitioning and fracture line

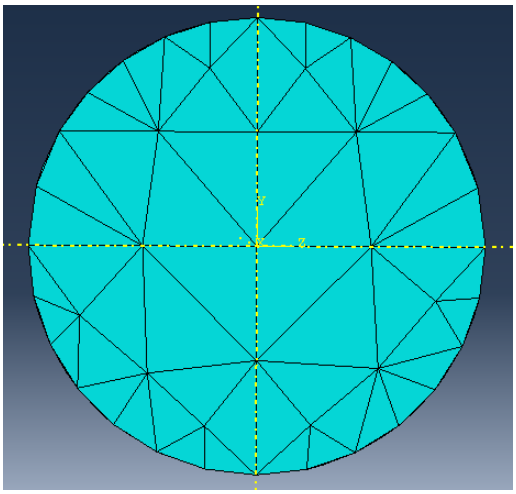

Figure 3.16 - Model with 50% Radius fracture meshed with tetrahedral mesh with cross section partitioning and fracture line

- **Partition B-1**, an inner circle was designed to give a circular path for elements outside this circle that included the fracture area and give order to the mesh elements inside the inner circle area. With this partitioning it was permitted to decrease the number of elements outside the study area and the circular path created a smooth meshing reducing any distorted element error during the job submission, fig. 3.17 and fig. 3.18.

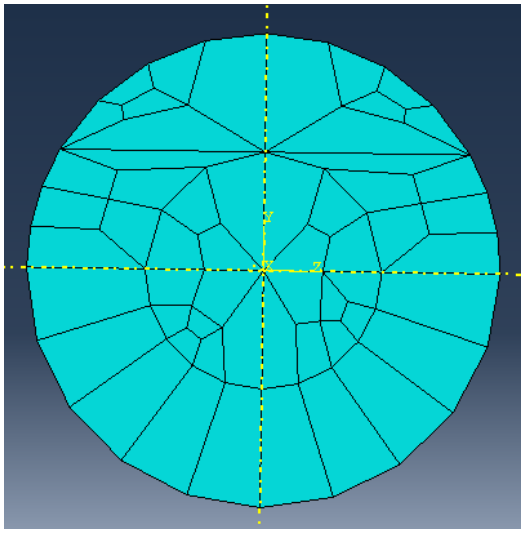

Figure 3.17 - Model with 50% Radius fracture meshed with hexahedral mesh with cross section, inner circle and fracture partitioning

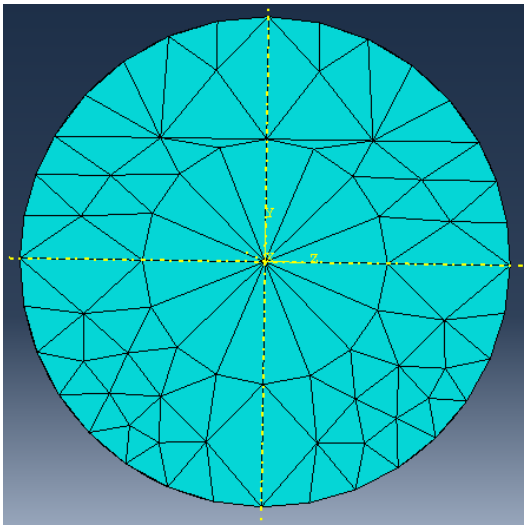

Figure 3.18 - Model with 50% Radius fracture meshed with tetrahedral mesh with cross section, inner circle and fracture partitioning

- **Partition B-2**, for the 10% fracture radius model some variations of the partition B-1 was applied. The inner circle had a lower dimension so that the outer circle area can be meshed with larger nodes, reducing the number of elements needed.
- **Partition C**, in the fracture areas a zonally partitioning was applied. This partitioning was to create the study nodes that are needed for each case study, fig. 3.19 and fig. 3.20.

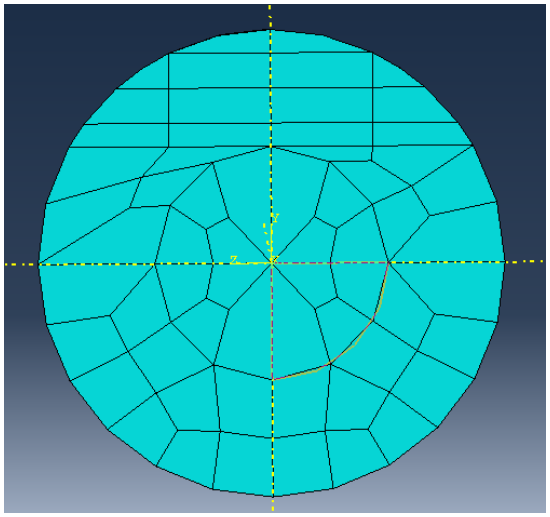

Figure 3.19 - Model with 50% Radius fracture meshed with hexahedral mesh with cross section, inner circle and divided fracture partitioning

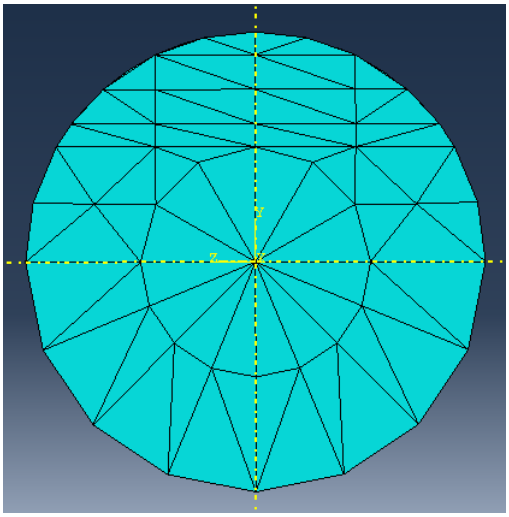

Figure 3.20 - Model with 50% Radius fracture meshed with tetrahedral mesh with cross section, inner circle and divided fracture partitioning

3.13 Tetrahedral meshing of the model

In the controls panels we have to assign what kind of mesh each part will have. Assuming that this is a not a complex model and in order to avoid having to add extra partitioning to the model, the tetrahedral meshing seemed a fair enough mesh to be assigned. The “Free” Tetrahedral meshing was assigned, fig. 3.21 .

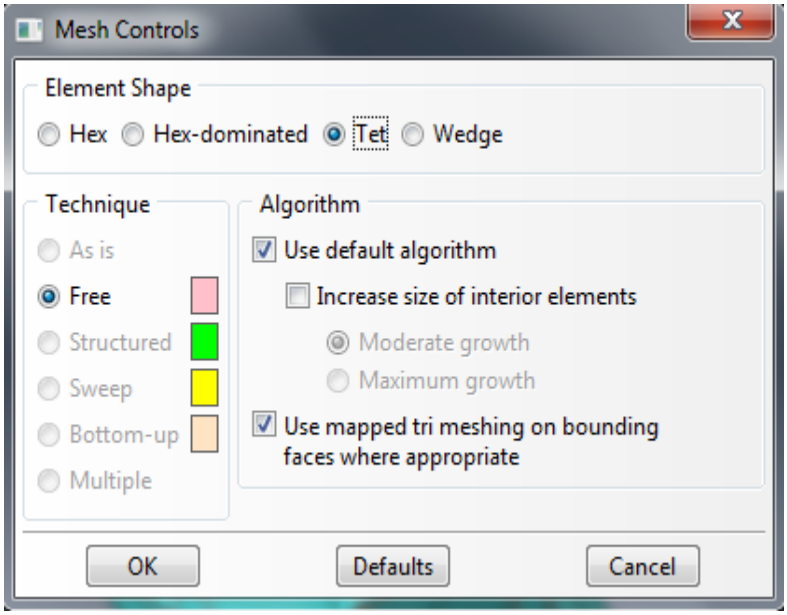

Figure 3.21 – Mesh control

Although this type of meshing is automatic, there was a need achieving an optimal element size and contour smoothness in order to avoid obtaining distorted elements and just enough information in the area of study.

Later during the processing stage some types of part seed would not work. The calculation step came to a stop because of Errors derived by distorted elements or entered a Looping increment.

Other assumptions later acknowledge was that the seeding had to change in accordance to the rotation of the shaft and crack percentage.

For higher rotational speeds the gap between the maximum element size for the edge seeding and the minimum instance seeding should be lowered. This was needed to avoid distortion of the elements in transition between the two seeding.

The crack percentage affected mainly the edge seeding. The lower percentage of crack the lower should be the seeding of the fractured area. This increased the number of elements around the surrounding area.

- **Model 50% Radius fracture, 1000 rad/s**

With partition C and B-1,

Table 3.6 –Job submitted for tetrahedral mesh with 50% radius fracture, 1000 rad/s

Seed instance	Max instance seed deviation	Edge Seed	Max edge seed deviation	Final job work (%)
0,022	0,01	-	-	100%
Comments	N/A the use of tri meshing Job: Tet50V1000ir			

- **Model 50% Radius fracture, 500 rad/s**

With partition C and B-1,

Table 3.7 –Job submitted for tetrahedral mesh with 50% radius fracture, 500 rad/s

Seed instance	Max instance seed deviation	Edge Seed	Max edge seed deviation	Final job work (%)
0,022	0,01	-	-	100
Comments	N/A the use of tri meshing Job: Tet50V500			

- **Model 25% Radius fracture, 1000 rad/s**

With partition B-1,

Table 3.8 –Job submitted for tetrahedral mesh with 25% radius fracture, 1000 rad/s

Seed instance	Max instance seed deviation	Edge Seed	Max edge seed deviation	Final job work (%)
0,03	0,01	0,01	0,01	32,3 - error
0,03	0,01	0,005	0,01	13 - error

With partition C and B-1,

Table 3.9 –Job submitted for tetrahedral mesh with 25% radius fracture, 1000 rad/s

Seed instance	Max instance seed deviation	Edge Seed	Max edge seed deviation	Final job work (%)
0,022	0,01	-	-	50 - loop
0,02	0,01	-	-	13
0,019	0,01	-	-	100
Comments	N/A the use of tri meshing; nrº elements 2651/2651 Job: Tet75V1000-B			

- **Model 25% Radius fracture, 500 rad/s**

With partition B-1,

Table 3.10 – Job submitted for tetrahedral mesh with 25% radius fracture, 500 rad/s

Seed instance	Max instance seed deviation	Edge Seed	Max edge seed deviation	Final work (%)
0,04	0,01	0,0008	0,01	error
0,04	0,01	0,00075	0,01	error
0,03	0,01	0,00075	0,01	error
0,03	0,01	0,00085	0,01	50 - loop
0,03	0,01	0,0009	0,01	50 - loop
0,03	0,01	0,0008	0,01	40
0,03	0,01	0,0009	0,01	100

With partition C and B-1,

Table 3.11 – Job submitted for tetrahedral mesh with 25% radius fracture, 500 rad/s

Seed instance	Max instance seed deviation	Edge Seed	Max edge seed deviation	Final job work (%)
0,022	0,01	-	-	100
Comments		N/A the use of tri meshing Job: Tet75V500		

- **Model 10% Radius fracture, 1000 rad/s**

With partition C and B-1,

Table 3.12 – Job submitted for tetrahedral mesh with 10% radius fracture, 1000 rad/s

Seed instance	Max instance seed deviation	Edge Seed	Max edge seed deviation	Final job work (%)
0,022	0,01	-	-	100
Comments		N/A the use of tri meshing Job: Tet90V1000ir		

- **Model 10% Radius fracture, 500 rad/s**

With partition C and B-1,

Table 3.13 – Job submitted for tetrahedral mesh with 10% radius fracture, 500 rad/s

Seed instance	Max instance seed deviation	Edge Seed	Max edge seed deviation	Final job work (%)
0,022	0,01	-	-	100
Comments		N/A the use of tri meshing Job: Tet90V500ir		

With partition C and B-2,

Table 3.14 – Job submitted for tetrahedral mesh with 10% radius fracture, 500 rad/s

Seed instance	Max instance seed deviation	Edge Seed	Max edge seed deviation	Final job work (%)
0,022	0,01	-	-	50
Comments	N/A the use of tri meshing Job: Tet90V500ir3			
0,022	0,01	-	-	16
Comments	using tri meshing			
0,02	0,01	-	-	50
Comments	N/A the use of tri meshing			
0,015	0,01	-	-	4 - aborted
Comments	N/A the use of tri meshing; nr. of elements 5 648/5 648			
0,01	0,01	-	-	Small step increase - aborted
Comments	N/A the use of tri meshing; nr. of elements 14 000/14 000			

3.14 Hexahedral meshing of the model

The hexahedral meshing has to consider a numerous of modelling assumptions. The partitioning has to be considered in order seed a smooth meshing in the flow direction. If not meshed correctly this type of mesh is more prawn for distortion errors and computing loops when the cells suffer huge increase in the energy applied to them.
By applying some of the partitions referred in subchapter 3.12 results were obtained for the 50% radius fracture model at 500 rad/s and 1000 rad/s and for the 75% radius fracture model at 500 rad/s. The other models had high energy increase that caused element distortion and abortion of the simulation.

- **Model 50% radius fracture, 1000 rad/s**

With partition C and B-1,

Table 3.15 – Job submitted for hexahedral mesh with 50% radius fracture, 1000 rad/s

Seed instance	Max instance seed deviation	Edge Seed	Max edge seed deviation	Final job work (%)
0,022	0,1	-	-	32
Comments	Advanced front; N/A the use of mapped meshing; nr. of elements 588/588			
0,02	0,1	-	-	14
Comments	Advanced front; N/A the use of mapped meshing			
0,025	0,1	-	-	94
Comments	Advanced front; N/A the use of mapped meshing; nr. of elements 504/504 Job: Quad50V1000-A			
0,0245	0,01	-	-	100
Comments	Advanced front; N/A the use of mapped meshing; nr. of elements 630/630 Job: Quad50V1000-C			

- **Model 50% radius fracture, 500 rad/s**

With partition B-1,

Table 3.16 – Job submitted for hexahedral mesh with 50% radius fracture, 500 rad/s

Seed instance	Max instance seed deviation	Edge Seed	Max edge seed deviation	Final job work (%)
0,022	0,1	-	-	14,4 – error
0,04	0,01	-	-	4,8 – error
0,02	0,01	-	-	22,9 – error
0,01	0,01	-	-	4,2 – error
0,04	0,001	-	-	58 – loop

With partition C and B-1,

Table 3.17 – Job submitted for hexahedral mesh with 50% radius fracture, 500 rad/s

Seed instance	Max instance seed deviation	Edge Seed	Max edge seed deviation	Final job work (%)
0,0245	0,01	-	-	100
Comments	Advanced front; N/A the use of mapped meshing; nr. of elements 1159/1159 Job: Quad50V500-A			

- **Model 25% radius fracture, 500 rad/s**

With partition B-1,

Table 3.18 – Job submitted for hexahedral mesh with 25% radius fracture, 500 rad/s

Seed instance	Max instance seed deviation	Edge Seed	Max edge seed deviation	Final job work (%)
0,06	0,01	-	-	28,5 – error
0,05	0,01	-	-	30 – error
0,03	0,01	-	-	100
0,022	0,01	-	-	44,3 – error
0,02	0,01	-	-	32 – loop

With partition C and B-1,

Table 3.19 – Job submitted for hexahedral mesh with 25% radius fracture, 500 rad/s

Seed instance	Max instance seed deviation	Edge Seed	Max edge seed deviation	Final job work (%)
0,0245	0,01	-	-	100
Comments	Advanced front; N/A the use of mapped meshing; nr. of elements 1159/1159 Job: Quad75V500-A			

- **Model 25% Radius fracture, 1000 rad/s**

With partition B-1,

Table 3.20 – Job submitted for hexahedral mesh with 25% radius fracture, 1000 rad/s

Seed instance	Max instance seed deviation	Edge Seed	Max edge seed deviation	Final job work (%)
0,022	0,1	-	-	20 – error
0,02	0,1	-	-	53 – error
0,01	0,1	-	-	63 – error
0,005	0,1	-	-	50 – error
0,022	0,01	-	-	52,56 – loop
0,02	0,01	-	-	17,33 - error

With partition C and B-1,

Table 3.21 – Job submitted for hexahedral mesh with 25% radius fracture, 1000 rad/s

Seed instance	Max instance seed deviation	Edge Seed	Max edge seed deviation	Final job work (%)
0,0245	0,01	-	-	30
Comments	Advanced front; N/A the use of mapped meshing; nr. of elements 1159/1159 Job: Quad75V1000-A			
0,025	0,01	-	-	32
Comments	Advanced front; N/A the use of mapped meshing; nr. of elements 1059/1059 Job: Quad75V1000-B			
0,023	0,01	-	-	21
Comments	Advanced front; N/A the use of mapped meshing; nr. of elements 1459/1459 Job: Quad75V1000-C			

3.15 Meshing Error

As stated before the meshing of the model can produce some error during the meshing process or even the type and refinement of the mesh used. In this subchapter some of these cases will be shown.

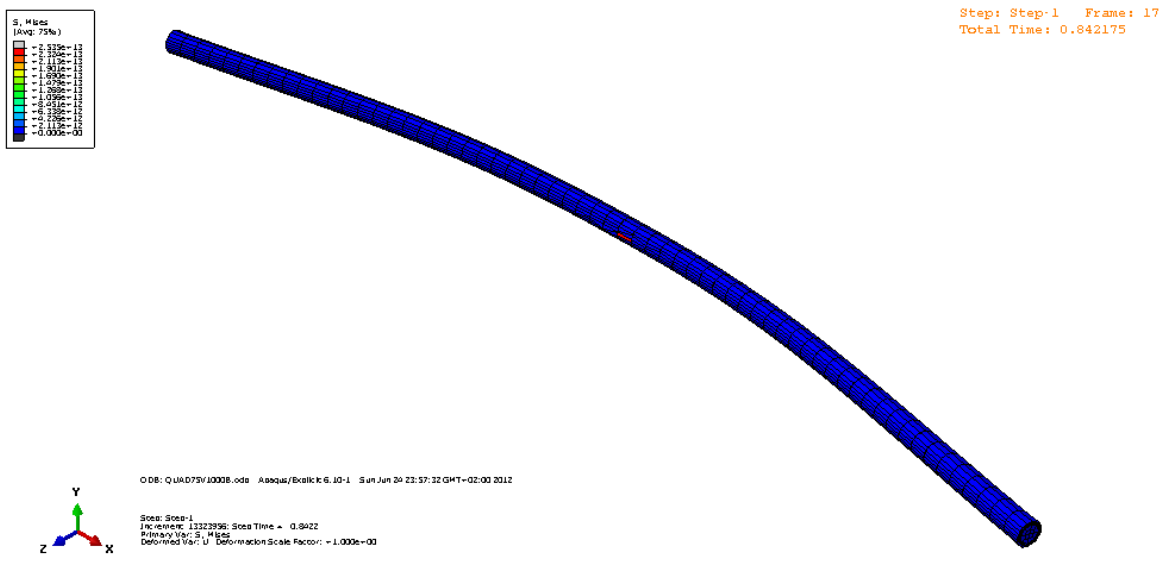

Figure 3.22 – Element distortion and simulation abortion on hexahedral meshed model

In figure 3.22 the distortion that occurs in one of the study models with a hexahedral mesh leads to a job abortion. The model tends to bend due to an excessive strain, noticeable in the centre of the shaft (fracture zone) using the Von Misses stress tool.

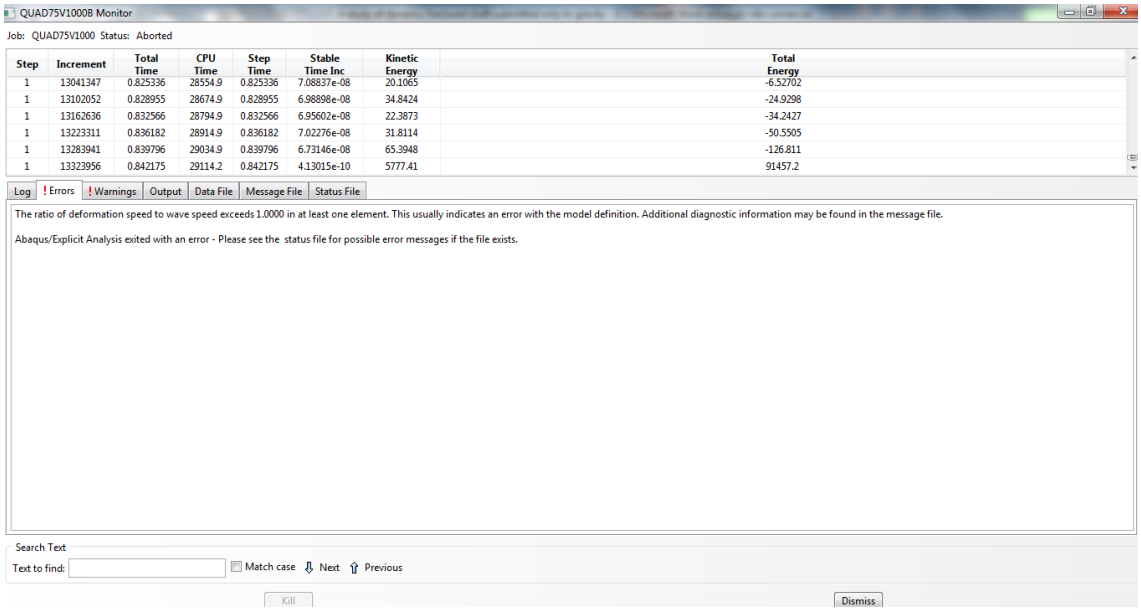

Figure 3.23 – Monitoring the job process

For the same job of figure 3.22 we can see in figure 3.23 the sudden spike of total energy in the last step processing. The program consequently aborted and appointed an error as shown.

This occurs normally due to the mesh type or poor meshing technics. Special attention has to be paid to the model partitioning too.

Chapter 4

Results

In this chapter the simulation results are going to be analysed and discussed.

As said in chapter I, the expected final results are the stress analysis in the fractured area. To do that, we are going to extrapolate points that can show the shifting tensions that take in the fractured area. This study will be done in 6 different study models:

- Shaft with 50% Radius fracture at speed rotation of 500 radians/s and 1000 radians/s;
- Shaft with 25% Radius fracture at speed rotation of 500 radians/s and 1000 radians/s;
- Shaft with 10% Radius fracture at speed rotation of 500 radians/s and 1000 radians/s.

So in order to obtain a complete overview of the analysis we are going to establish some criteria to choose the desired nodes of study.

First criteria: is to obtain nodes in specific positions of interest. For example, the behaviour of the stress near the fracture line or in the outer border of the fracture can give some insight of the stress analysis in extreme point of the shaft. In the larger fractures (the 50% and 25% radius fracture) we are going to analyse the inner mid area between the extreme points of the fracture.

Second criteria: study of the different rotating areas. We can divide this into 3 zones; the first zone is in the rotating direction of the shaft, is a zone that is the first to be submitted to the opening/closing mechanism of the shaft. The central zone has the

largest area of the fracture. And the 3rd zone is opposed to the rotating direction, is the zone that is the last one to enter the opening/closing mechanism.

Apart from the graphical results obtained and worked in this chapter. For more information regarding the nodal stress value during a time interval of 0 to 1 second, in Annex there is a table of contents for each case study and a more graphical overview of the shifting stress tensions in the fractured area for each case study.

4.1 Results with Tetrahedral mesh

4.1.1 Shaft with 50% Radius fracture

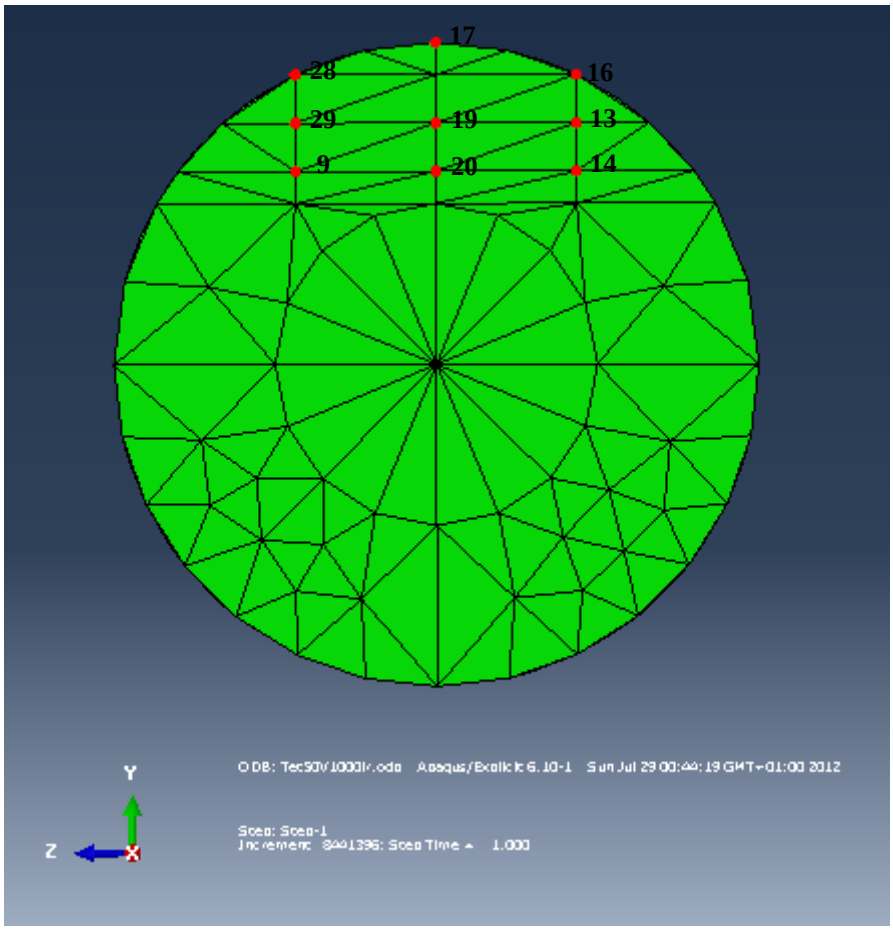

Figure 4.24 - Node number and position on the tetrahedral mesh for 50% radius fracture

4.1.1.1 Speed rotation 500 rad/s

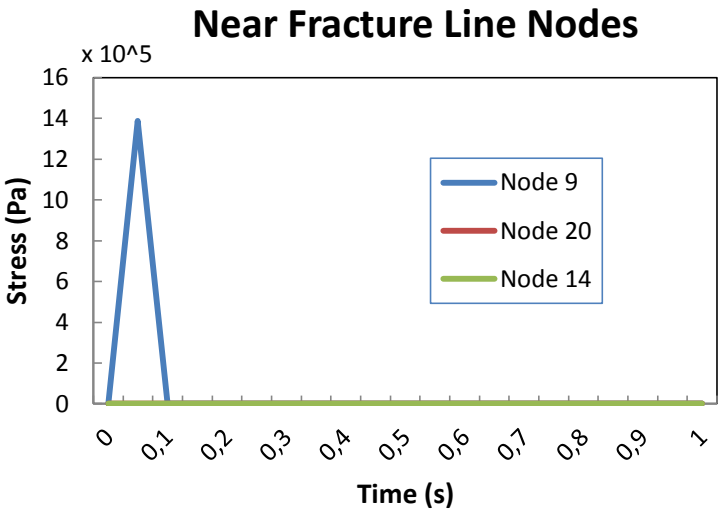

Figure 4.25 - Stress analysis for near fracture line nodes of 50% radius fracture at a 500 radians/s

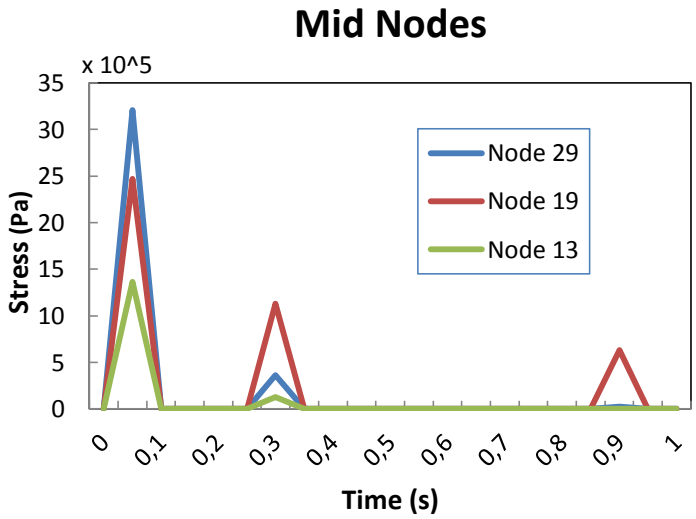

Figure 4.26 - Stress analysis for mid nodes of 50% radius fracture at a 500 radians/s

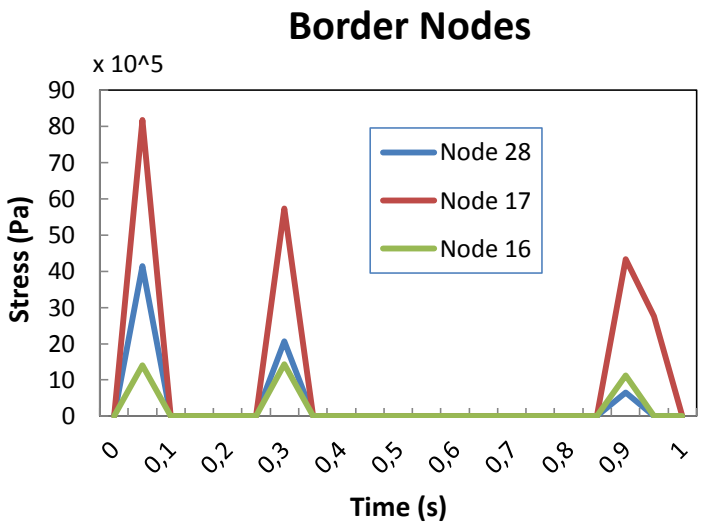

Figure 4.27 - Stress analysis for border nodes of 50% radius fracture at a 500 radians/s

1st case study is the **50% radius fracture model with a 500 radians/s rotation**.

In figure 4.25, the near fracture line nodes, only the node 9 is submitted to a huge stress, almost 1,4 MPa in the 0-0,1 sec. time interval. The other nodes aren't submitted to that stress value so there isn't reliable information. There is to notice that this node belongs to the zone that is first submitted to the breathing mechanism.

In figure 4.26, the mid nodes, all the nodes are submitted to a reasonable amount to stress but node 29 is the node that is affected the most, submitted to a stress above 3 MPa in the 0-0,1 sec. time interval. This node belongs to the zone that is first submitted to the breathing mechanism. Afterwards there are other stress spikes during the revolution of the shaft that mainly affect the central node, above 1 MPa at 0,25-0,4 sec and above 0,5 MPa 0,85-1 sec.

In figure 4.27, the outer border fracture nodes there is a change. There are 3 stress spikes being the biggest spike in the 0-0,1 sec time interval. In this stress spike the central zone node 17 is submitted to the maximum stress above 8 MPa. The other 2 spikes, the central zone node is submitted to the highest stress, above 5 MPa at the 0,25-0,4 sec and above 4 MPa 0,85-1 sec.

4.1.1.2 Speed rotation 1000 rad/s

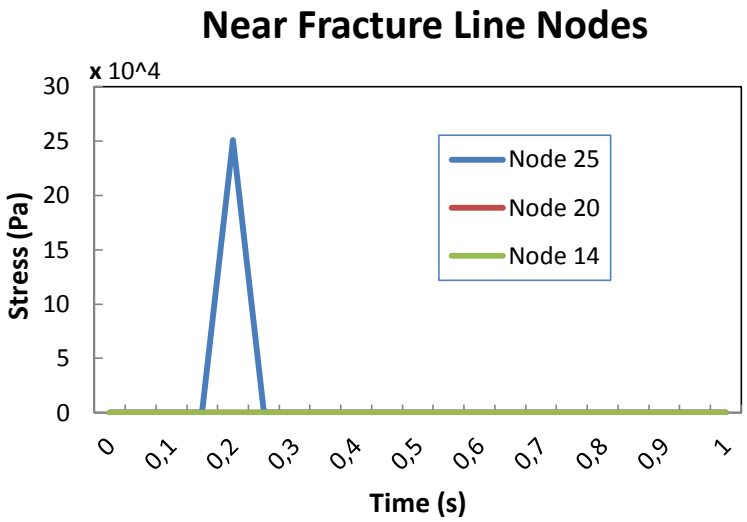

Figure 4.28 - Stress analysis for near fracture line nodes of 50% radius fracture at a 1000 radians/s

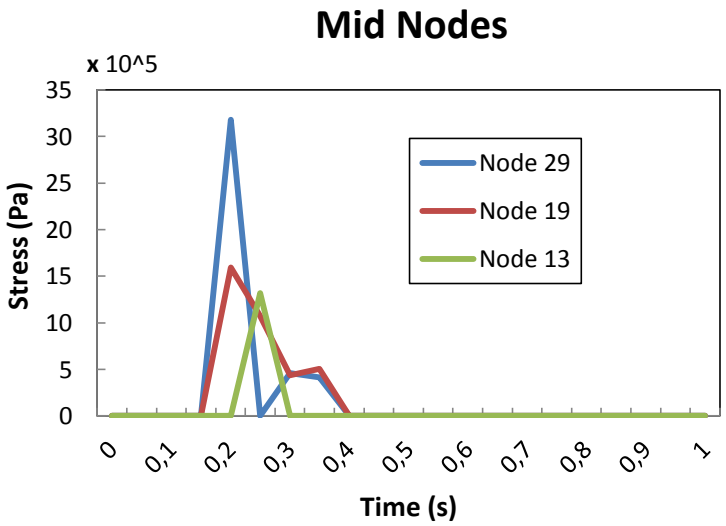

Figure 4.29 - Stress analysis for mid nodes of 50% radius fracture at a 1000 radians/s

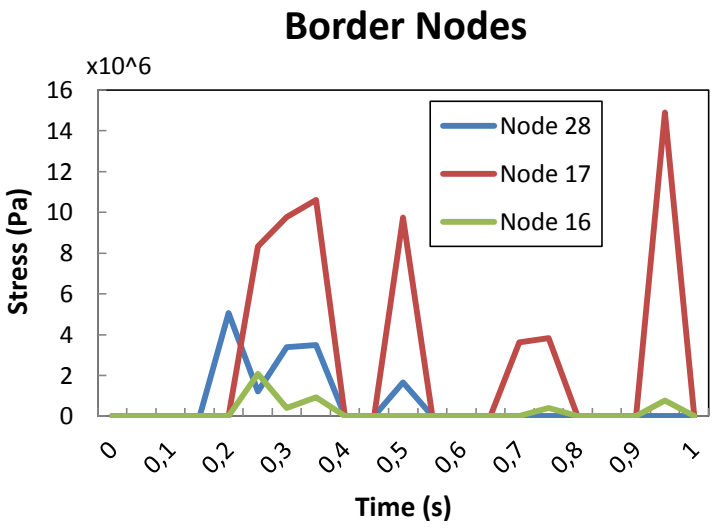

Figure 4.30 - Stress analysis for border nodes of 50% radius fracture at a 1000 radians/s

2nd case study is the **50% radius fracture model with a 1000 radians/s rotation**.

In this case the shaft is working after the first critical speed, so is expected a higher stress on the nodes.

In figure 4.28, the near fracture line nodes, we find something similar as figure 4.2. The only node submitted to a higher stress is node 25 (same as node 9 from the previous case study) located in the zone that is first submitted to the breathing mechanism. The value of stress is 0,25 MPa in the time interval 0,15-0,3 sec.

In figure 4.29, the mid nodes, all 3 nodes analysed in this zone register some stress value on the 0,15-0,45 sec time interval. Node 29 registers the highest stress, above 3,0 MPa, and the other nodes values between 1,6 MPa and 1,2 MPa.

In figure 4.30, the outer border of the fracture nodes, there are 4 stress spikes. The highest stress spike is registered in the 0,9-1 sec time interval, in central-node 17 the a stress above 14 MPa. Other spikes are in the time intervals of 0,15-0,45 sec with a value above 10 MPa, 0,45-0,6 sec with a value around 10 MPa and 0,65-0,85 sec with a value around 4 MPa, all belonging to central-node 17.

4.1.2 Shaft with 25% radius fracture

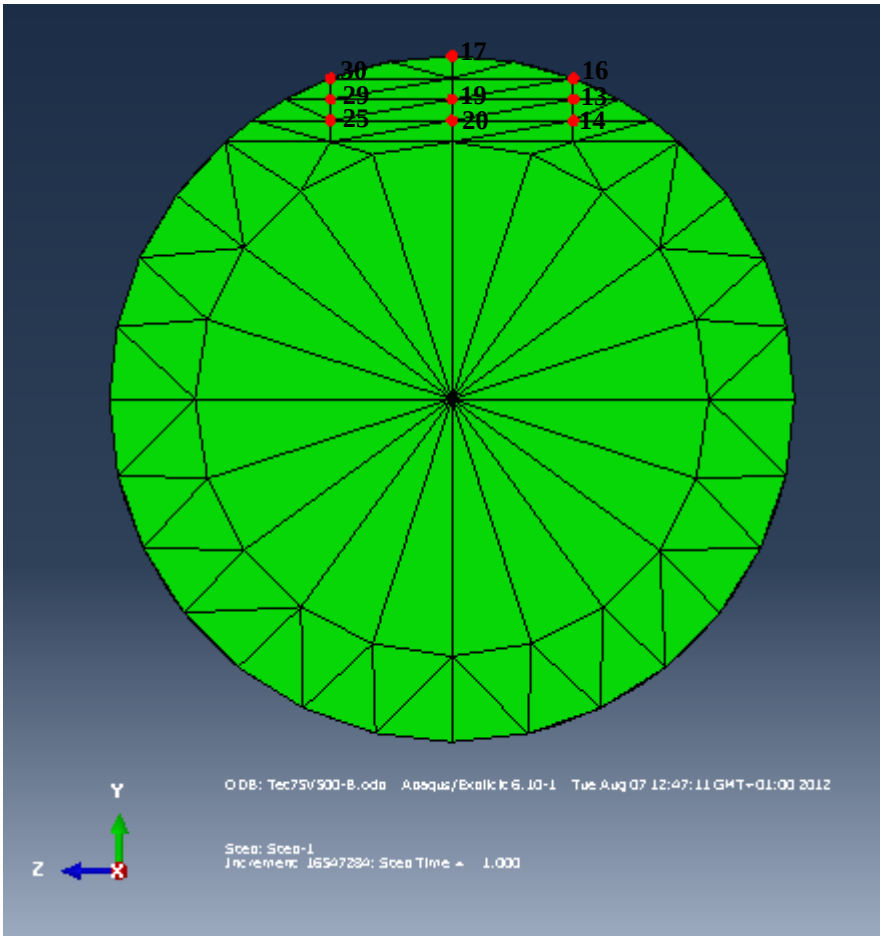

Figure 4.31 - Node number and position on the tetrahedral mesh for 75% Radius fracture

4.1.2.1 Speed rotation 500 rad/s

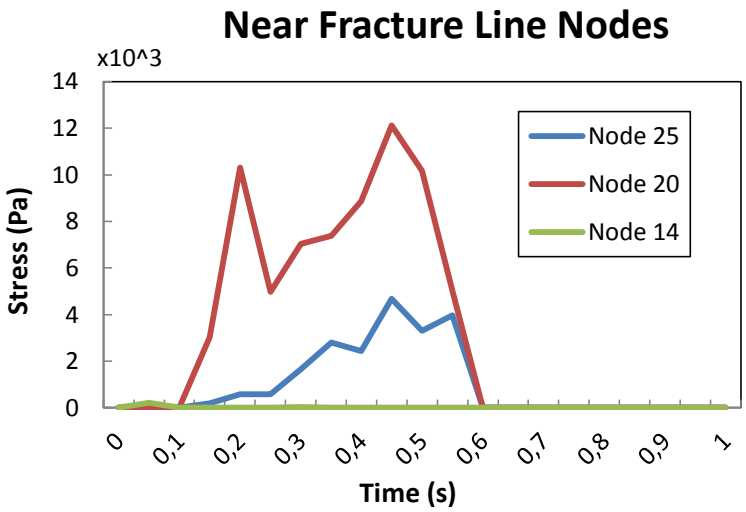

Figure 4.32 - Stress analysis for near fracture line nodes of 25% radius fracture at a 500 radians/s

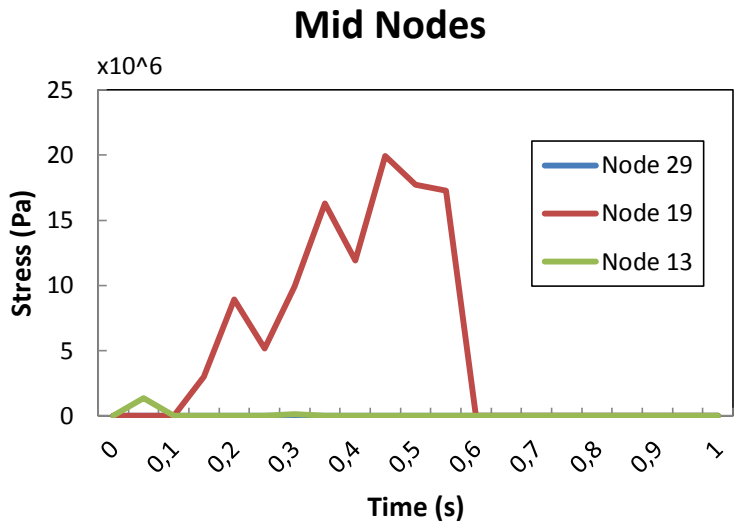

Figure 4.33 - Stress analysis for mid nodes of 25% radius fracture at a 500 radians/s

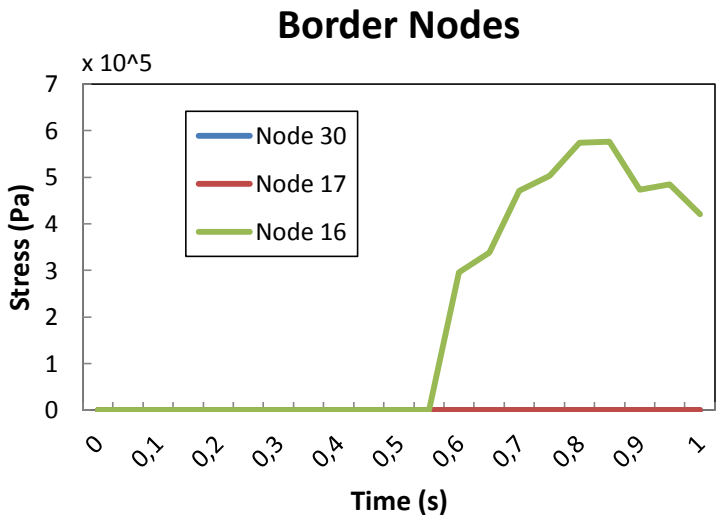

Figure 4.34 - Stress analysis for border nodes of 25% radius fracture at a 500 radians/s

3rd case study is the **25% radius fracture model with a 500 radians/s rotation**.

In figure 4.32, the near fracture line nodes, there is an area of graphical points between the time interval of 0,1-0,45 sec where the stress values vary for the node 20 and 25. Node 14 only registers a small residual stress between 0-0,15 sec. Node 20 has the higher stress values being the maximum value 12 kPa. Node 25 highest value is above 4 kPa.

In figure 4.33, the mid fracture nodes, there is an area of graphical points for node 19 in the time interval 0,1-0,65 sec where the highest stress value 20 MPa. Node 13 registers a small stress value in the interval 0-0,1 sec.

In figure 4.34, the near border fracture nodes; there is only registered one node to achieve having high stress value. Node 16 has an area of points that begins at 0,55 sec. The highest value of stress is lower than 0,6 MPa.

4.1.2.2 Speed rotation 1000 rad/s

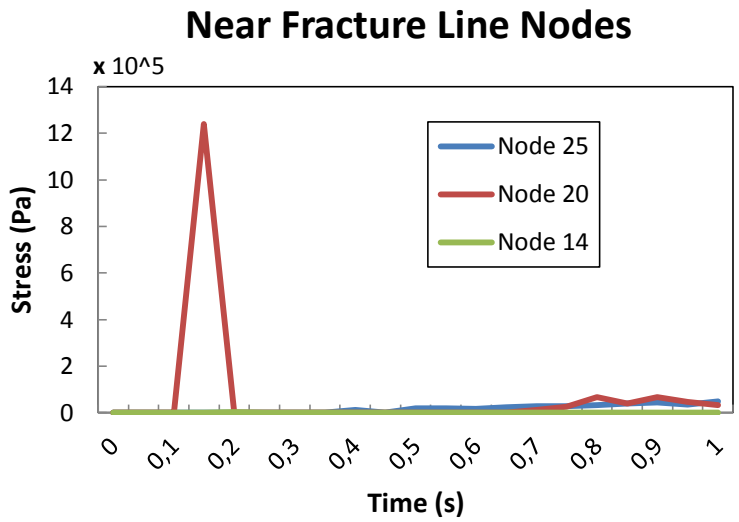

Figure 4.35 - Stress analysis for near fracture line nodes of 25% radius fracture at a 1000 radians/s

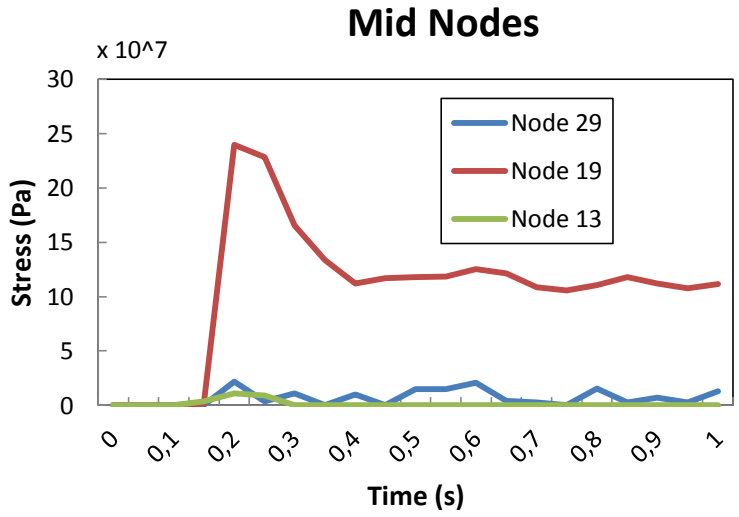

Figure 4.36 - Stress analysis for mid nodes of 25% radius fracture at a 1000 radians/s

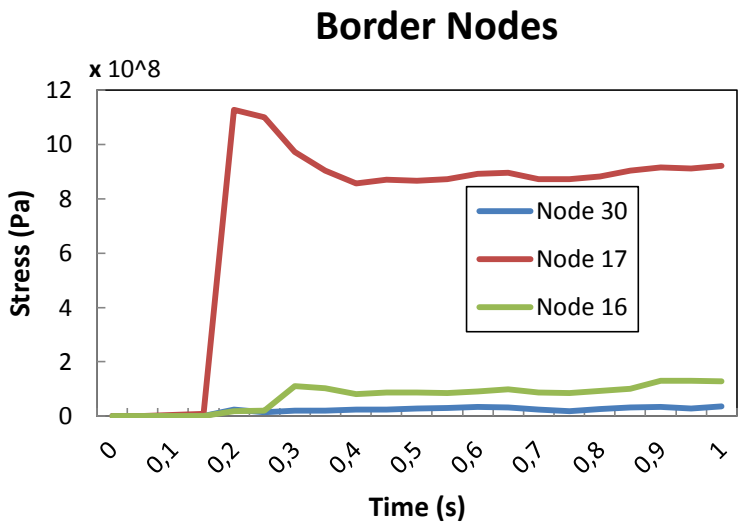

Figure 4.37 - Stress analysis for border nodes of 25% radius fracture at a 1000 radians/s

4th case study is the **25% radius fracture model with a 1000 radians/s rotation**.

In figure 4.35, near fracture line nodes, we register stress activity in 2 nodes. The central node 20 registers the highest stress in the interval 0,1-0,25 sec with 1,2 MPa. At 0,4 sec a small residual stress is registered for node 25. At 0,7 sec the same occurs for node 20.

In figure 4.36, the mid nodes, all 3 nodes register high stress activity. The central node 19 has the highest stress points, that start at 0,16 sec. The maximum point registered for that node is 250 MPa. Node 29 is submitted to continuous stress at 0,16 sec being its maximum around 25 MPa. Node 13 registers a residual stress in comparison to the other nodes.

In figure 4.37, the outer border fracture nodes, the 3 nodes are submitted to a continuous high stress. The central node 17 begins to be submitted to a high stress at 0,05 sec, having the highest maximum stress value of 1,1 GPa. Then afterwards it stabilizes between the values 1,0 GPa and 0,8 GPa beginning at 0,4 sec. Node 16 registers the 2nd highest stress values that begin at 0,05 sec. Its values stabilize near 0,1 GPa. Node 30 has a low stress value that begin to be register at 0,05 it stabilizes in low stress values.

4.1.3 Shaft with 10% radius fracture

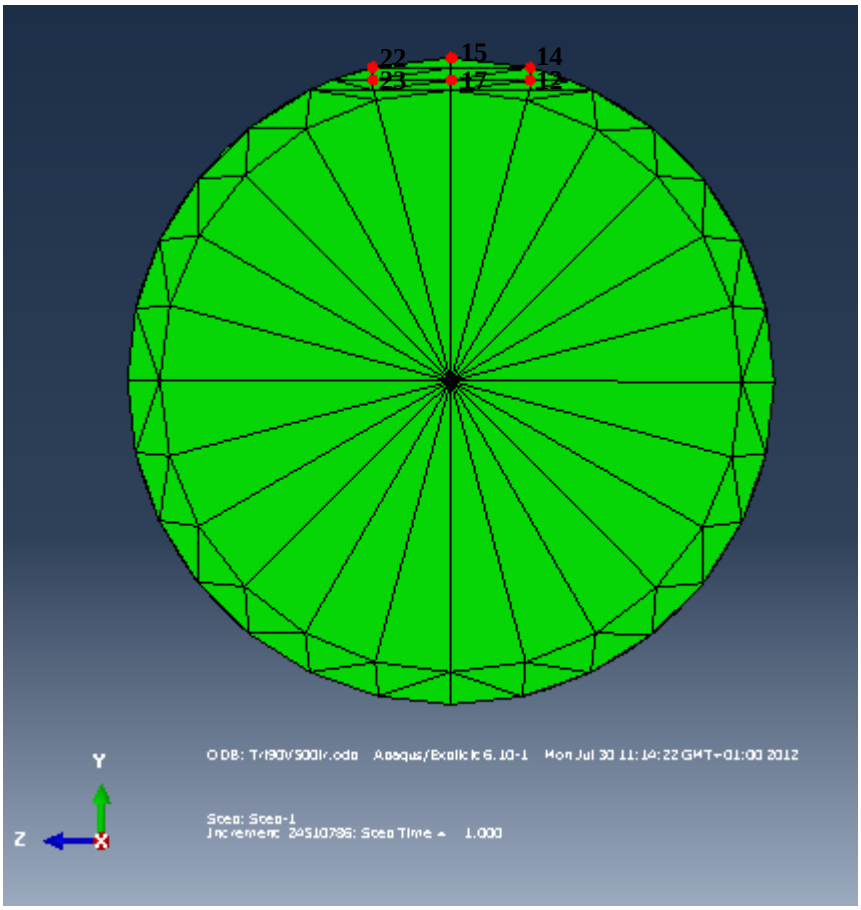

Figure 4.38 - Node number and position on the tetrahedral mesh for 10% Radius fracture

4.1.3.1 Speed rotation 500 rad/s

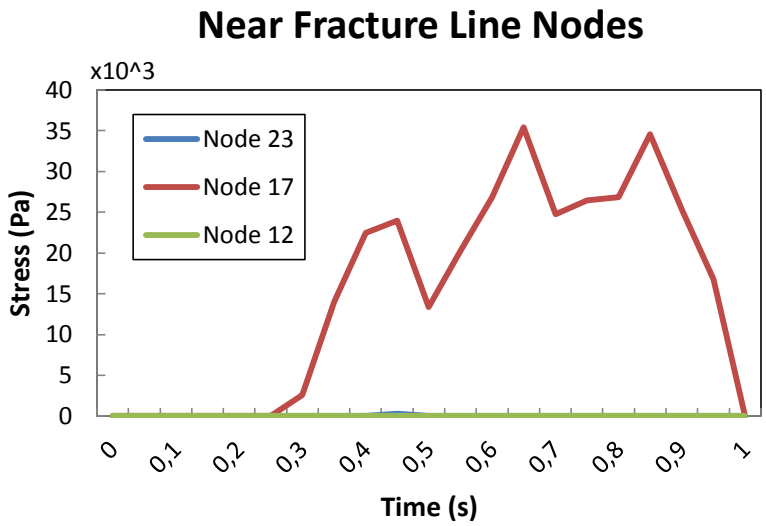

Figure 4.39 - Stress analysis for near fracture line nodes of 10% radius fracture at a 500 radians/s

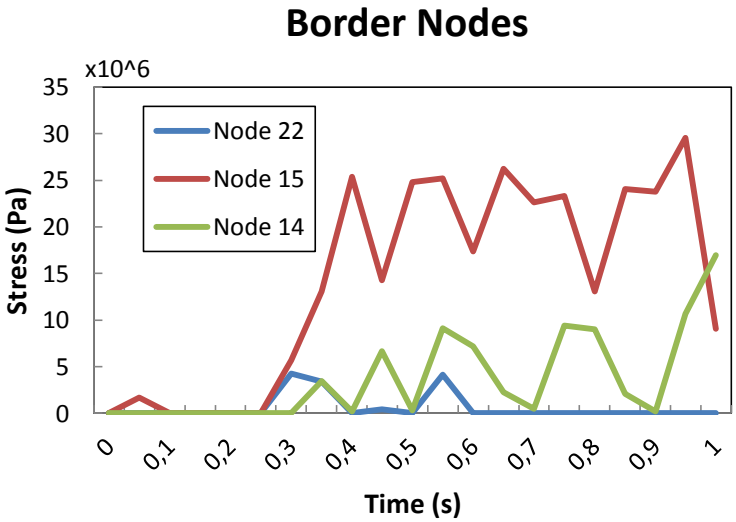

Figure 4.40 - Stress analysis for border nodes of 10% radius fracture at a 500 radians/

5th case study is the **10% radius fracture model with a 500 radians/s rotation**.

In figure 4.39, the near border fracture line nodes, we just register a reasonable stress activity on the central node 17. It is a continuous stress activity that begin at 0,25 sec and ends at 1 sec. Its highest point is in the region of 35 kPa at 0,65 sec, other similar high in the same region occurs at 0,85 sec.

In figure 4.40, the border nodes, there is a register of a continuous stress activity in the 3 nodes. The central node 15 activity has the hugest stress area. It starts with a small slope from 0-0,15 sec but than on it has a continuous activity starting at 0,25 sec. The maximum is reached at 0,95 sec with a stress of 30 MPa. Other high points from this node are around 25 MPa. The farther node 14 register the second highest stress area. Starting at 0,3 sec it reaches 3 spike points but are below 10 MPa. At 0,9 sec its stress values starts to increase reaching values above 15 MPa at 1 sec. The near point 22 registers small activity reaching 2 spike stress values below 5 MPa.

4.1.3.2 Speed rotation 1000 rad/s

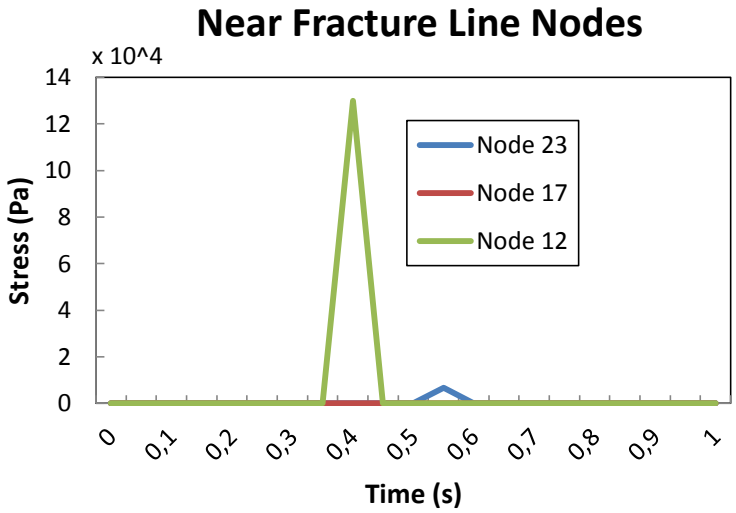

Figure 4.41 - Stress analysis for near fracture line nodes of 10% radius fracture at a 1000 radians/s

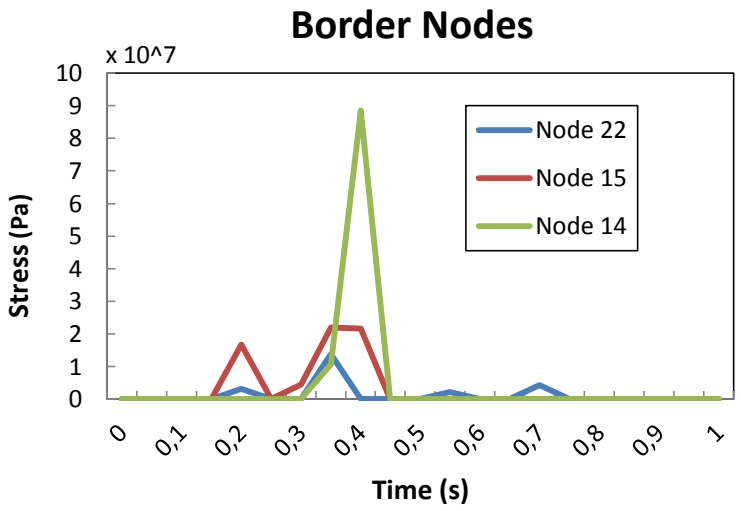

Figure 4.42 - Stress analysis for border nodes of 10% radius fracture at a 1000 radians/s

6th case study is the **10% radius fracture model with a 1000 radians/s rotation**.

In figure 4.41, the near fracture line nodes, we register a spike in the farther node 12 in the time interval between 0,35-0,5 sec. Being the highest value above 120 kPA. The near node 23register some small activity "slope" activity between 0,5-0,65 sec.

In figure 4.42, the outer fracture border nodes, the farther node 14 register the maximum stress spike value around time 0,4 sec with a 90 MPa. The central node 15 has 2 reasonable spike values reaching above 20 MPa. The near node 23 has small slope values being its maximum around 10 MPa.

4.3 Results discussion

The analysis of the graphical results of each of the study cases show us some interesting results. As said in chapter IV, the simplified tetrahedral meshing, TET4, was used in the models. Although the results it gives have a huge error, it is easy to apply giving less distorted elements or performance error. It provides a fair glimpse of the behaviour of distinct types of fracture submitted to rotating speeds above and under the critical velocity.

In the **1st case study and 2nd case study** we notice an increase of stress pointing outwards from the near fracture line nodes to the outer border of the fracture. The nodes that are in the zone that is first submitted to the breathing mechanism are the ones who have the higher stress, except in the outer border fracture zone were the central nodes experiment a higher stress. As expected the stress is higher in the **2nd case study** and there is just a small change in the time intervals on where it occurs. It is noticed too, that instead of just isolated high stress spikes like registered on the **1st case study**, the stress submitted on the nodes have an escalated behaviour, so to say the nodes reach a maximum stress and diminish along time to lower values. This so happens on the mid-nodes and outer border fracture nodes. The other border nodes are submitted to more stress spikes than in the lower rotating model.

A brief overview of the **3rd case study** we notice that near fracture line nodes don't reach any reasonable stress value in comparison with 1st case study. Taking into account that the mid fracture nodes register a higher stress values that what was given in border fracture nodes and based on past studies that isn't reasonable. So we need to exclude figure 11 from this analysis.

The analysis of figure 9 and 10 gave expected results comparing with the 1st and 2nd case studies. The value of stress begins to increase from the near border fracture nodes to the mid nodes. The central nodes have the higher stress values.

In comparison, the **3rd and 4th case study** registered a high stress variation values between the 500 radians/s and 1000 radians/s than to the previous case study models analysed until now. In the low rotational speed model we register low value stress spikes around 10 MPa but in the high rotational speed model we register around 10 GPa. Like in past studied model the central nodes are the ones that are under the highest

stress and the stress increases outwards, from the near fracture line nodes to the border nodes.

Using the 1st and 2nd case study as reference we come to the **5th case study**, were we can see that the time and quantity of stress applied to the nodes have a dramatic increase. Even the near fracture line nodes are affected by the decrease of the fracture size, the central node is the only node that registers a high stress. At the border nodes the central node is the one that registers higher stress but the other nodes register some reasonable stress. When there is an increase of the shaft rotational speed, **6th case study**, we notice an interesting shift on where the stress is localized. The nodes that are the last to enter the breathing mechanism state experiment higher stress values than the other nodes this is valid for the near fracture line nodes and the border nodes. As past studied high rotation speed models, from the **5th to the 6th case study**, we notice a huge increase in the strain applied and that the border nodes experiment the higher stress values. On both case study it is noticeable the same aspect from the other case studies, the stress direction tends to point outward from the fracture line nodes to the outer border nodes, the time where the stress values occur come more late and the period of stress tends to be more continuous.

4.4 Conclusions

An overall analysis of all the study case models we get to the following conclusions:

- The fracture stress is in an outwards direction. The near fracture nodes have small stress applied to them than in comparison to the outer border of the fracture nodes. This is verified in all studied models.
- The increase of the shaft rotational speed to after critical speeds produces an increase of stress values in all nodes. It also produces the occurrence of more stress spikes and an increase of the graphical area of the nodal stress.
- The decrease of the shaft fracture produces an increase in time of the shaft nodal stress.
    - Stress interval - In the 50% radius fracture we only have isolated "spikes" of nodal stress in short periods of time. As we decrease the shaft fracture to 25% radius we begin to have a more continuous stress applied in the nodes and get more elevated stress values. And at 10% radius fracture the time interval the applied stress to the nodes increases to stable values.
    - Time displacement – It is registered that there is a time displacement on when the stress occurs. This time displacement gets higher as the fracture decreases.
    - The value of the stress increases for 50% to 25% radius fracture and later decrease for 10% radius fracture. By viewing the maximum reached in each case study we can compare. In the 50% radius fracture the maximum stress value is 140 MPa for 1000 radian/s. In the 25% radius fracture it reaches to values above 1 GPa for 1000 radian/s. And at 10% radius fracture the maximum stress value is 90 MPa at 1000 radian/s.
    - There a shifting in the zones on where the highest stress is detected. The central nodes are the nodes that are always submitted to stress values; at higher speeds those nodes reach the maximum stress values. Other important information is that for the 50% radius fracture the near node to the shaft rotational direction is submitted to a fair amount of stress. The inverse occurs when the fracture is 10% radius, the node that experiment last the breathing mechanism are the nodes that are submitted to stress.

Chapter VI

Future Works

During the conception of the model there was a need to rule out or establish some properties and concepts in order to get a functional model.

One aspect of relevance is that there was a need to establish the distance rotating reference point would not affect directly the shaft stresses on the fracture area. Doing a brief study on the matter, the conclusion was the overall stresses are not affected when there is just a slight increase in distance of the rotating reference points in relation to the shaft end. And so in the final study model the distance of the reference point from the shaft end was 0, 05 m, all the results were obtained under that distance value. But as we put under scrutiny the results given by the study it is noticeable there are different nodal stress values given by each of the study model with different rotating reference point distance. The model with the 0,0 m distance has high stress values in the near border line fracture and mid nodes and the model with 0, 05 m distance have the higher of the nodal stress values, we can see that in the study tables in the Annex. In the studied bibliography of the subject we notice a variety of studies conducted under the field of the position and distance of the rotating coupling and the effects it produces in the stresses of the fractured area. It would be interesting to study this effects influence different fracture depths. Using different rotating velocities and varying the distance of the reference point for a same fracture would be another interesting study.

Other aspect of relevance is to do this study under more refined meshes. The size of the elements used in this study allowed the obtainment of results with swift and fast job processing time and with little complexity. Each job took around 2 days to process and the mesh application didn't give huge element distortion or errors. But the stress values for the same type of model differ with the use of a tetrahedral or hexahedral mesh. Knowing the different properties of each of the mesh types the results given were

expected. In a study apart, the application of a TET10 mesh type proved a better fed of results in stress areas and there were no element distortion. The only problem was that one study model took 5 days to be completed. An outstanding increase of the processing cost. The hypothesis of a more powerful computer processor would facilitate the application of more complex mesh types.

Chapter VII

Bibliography

[1]. Chandan Kumar and Vikas Rastogi, “A Brief Review on Dynamics of a Cracked Rotor”, Sant Longowal Institute of Engineering and Technology, Longowal, Punjab, 15 December 2009

[2]. IUTAM Symposium on Emerging Trends in Rotor Dynamics: proceedings of the IUTAM Symposium on Emerging Trends in Rotor Dynamics, held in New Delhi, India, March 23-March 26, 2009, K Gupta, Dr., Dordrecht : Springer, 2011

[3]. Rankine, W.J.M. (1869): “On the centrifugal force of rotating shafts”. Engineer, Vol. 27, pp. 249-249

[4]. Dr. Rajiv Tiwari, “A Brief History and State of the Art of Rotor Dynamics”, Department of Mechanical Engineering Indian Institute of Technology Guwahati, 19 Dec 2008

[5]. Jeffcott, H.H. (1919): “The lateral vibration of loaded shafts in the neighborhood of a whirling speed: the effect of want balance”. Philos. Mag, Vol. 37, pp. 304-315

[6]. Stodala, A. (1924): “Dampf- und Gas-Turbinen. Verlag von Julius Springer. Berlin

[7]. Gasch, R. A, 1993, “Survey of the Dynamic Behaviour of a Simple Rotating Shaft with a Transverse Crack”, Journal of Sound and Vibration Vol. 162, pp313-332

[8]. Sinou, J-J., Lees, A.W., “The influence of cracks in rotating shafts”, Journal of Sound and Vibration, Volume 285, Issues 4-5, 6 August 2005

[9]. Dias, Teixeira F., Pinho-de-Cruz , J., Valente Fontes, R.A., de Sousa, R.J. Alves, “Método dos Elementos Finitos” Lidel Editora February 2007

[10]. Urbano, Álvaro Melendo, “Estudio de la interacción fisura-desequilibrio en la evolución de las orbitas de ejes rotativos”, Universidad Carlos III Madrid, mayo de 2011

[11]. ANSYS, “Rotordynamic analysis guide”, ANSYS Inc.,April 2009

[12]. Megias, Javier Arrieta,“Estudio de los factores influyentes en el modelo numérico de transmisión de ondas en un eje fisurado”, Universidad Carlos III Madrid, Deciembre 2009

[13]. Brito, Arul M. “Running ABAQUS 6.4” October 7 2005

[14]. ABAQUS User’s Manual, Version 6.7. Hibbit Karlsson & Sorenssen. INc 2007

[15]. Bachschmid, N., Pennacchi, P., Tanzi, E., “Cracked Rotors: A survey on static and dynamic behaviour including modelling and diagnosis”, Springer, 2010

[16]. KRUGUER, “Technical bulletin TBN017.0/1998”, 1998

[17]. Monteiro, Fernando Luiz, “Análises de falhas em eixo de laminadora”, Guaratinguetá 2004

[18]. Baker, Timothy J., “Mesh generation Art or Science?”, Elsevier Ltd., 2005

[19]. Dalgarno Rick, “ Converging on Composites: ABAQUS Mesh Tutorial – Partitioning Geometry to Improve Mesh Quality”, Fire hole Composites Analysis software and services blog, May 2012

[20]. Steven E. Benzley, Ernest Perry, Karl Merkley, Brett Clark, “A Comparison of All Hexagonal and All Tetrahedral Finite Element Meshes for Elastic and Elasto-plastic Analysis”, Brigham Young University

[21]. Xavier BOURDIN, Xavier TROSSEILLE, Philippe PETIT, Philippe BEILLAS, “Comparision of tetrahedral and Hexahedral meshes for organ finite modelling: An application to kidney impact”, Paper Number 07-0424

[22]. Savvas Savvakis, Zissis Samaras, “Numerical simulation for improving a rotary motor efficiency by flow optimization inside the Motor’s Chambers”, Aristotle University of Thessaloniki/Laboratory of Applied Thermodynamics, September 9-11, 2009

[23]. Entrekin,“Accuracy of MSC/NASTRAN First- and Second-Order Tetrahedral Elements in Solid Modelling for Stress Analysis”, Bell Helicopter Textron Inc.

[24]. ANSYS, “ANSYS Fluent manual 6.3”, 2007

[25]. Papadopoulos, Chris A., “The strain energy release approach for modelling cracks in rotors: A state of the art review”, Science Direct, 17 November 2007

[26]. Lissenden, C.J., Tissot, S.P., Threthewey, M. W., Maynard,K. P., “Torsion response of a cracked stainless steel shaft”, 26 December 2006

Chapter VIII

Annex

Rotor dynamics Terms

Critical velocity – The critical velocity occurs when the frequency produced by the movement of the shaft – exciting frequency – equals the natural harmonic frequency of the shaft (when it's fully stopped). Under these circumstances the shaft will enter into a harmonic state, having amplified vibrations – resonance, eq. 8.7.

$$\omega = \omega_{nf} = \sqrt{\frac{k_{eff}}{M}} \tag{8.7}$$

Gyroscope effect - this effect tends to appear because of the distribution of mass on the shaft or in the disc. When it's given angular moment to the shaft, the small impulses that is created tend to give the mass a small velocity increase perpendicular to the momentum direction, making the velocity on a local point to change without changing its module.

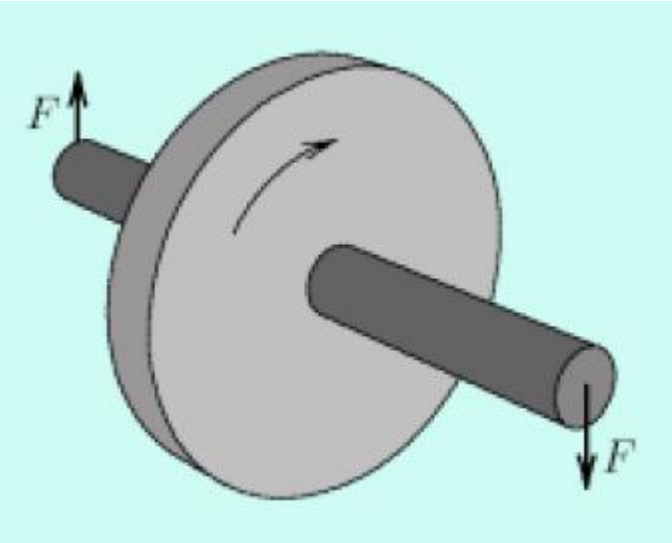

Figure 8.43 – Example of gyroscope effect

This effect is the main responsible of the link between natural frequencies and critical velocities on rotors. And can change the number of critical velocities.

Breathing mechanism – the type of rotor study taking into account the gravity is known as "weight dominated systems", figure 8.44. It can open and close according to its angular position and the stresses developed in the cracked surface. When the shaft rotates into higher speeds it is proved that the same forces that cause the static deflection components, excite also vibrations.

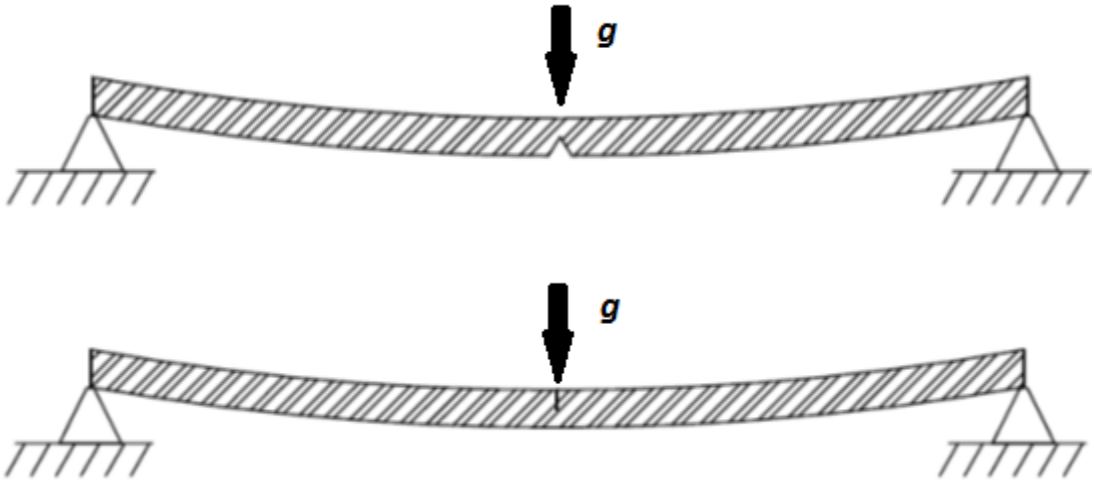

Figure 8.44 – "Weight dominated system". Open fracture (top), Closed fracture (bottom)

The opening and closing can be interpreted as a breathing mechanism. It causes to shift the stiffness and local compliance of the shaft according to the angular position. The maximum stiffness shaft is reached when the crack is totally closed (the crack position is at the top of the shaft), and equals the valour of the un-cracked. The minimum stiffness will be reached when the crack is totally opened (when the crack position is at bottom of the shaft). There is also an intermediate situation between opened and closed. We can understand better this mechanism through Mayes & Davies model [1], eq.8.8.

$$g(\phi) = \frac{1+\cos\phi}{2} \tag{8.8}$$

And shown on figure 8.45,

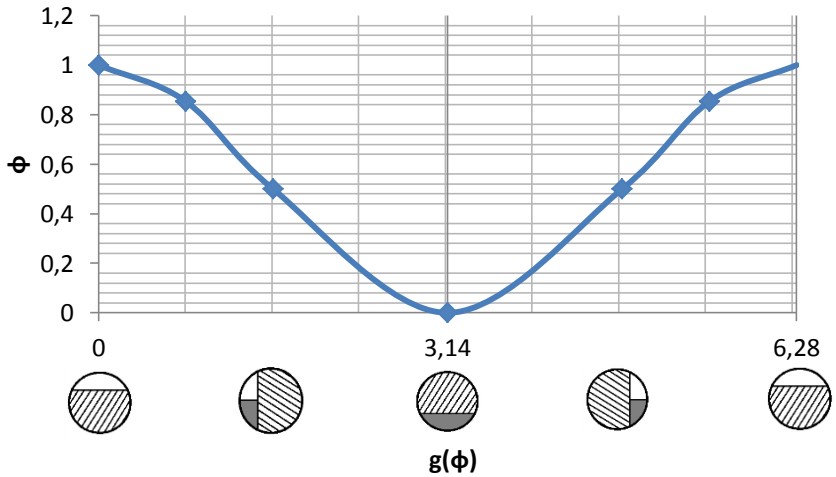

Figure 8.45 – Mayes & Davies breathing mechanism model

Truncation error – is the difference between the partial derivatives in the governing equations and their discrete approximations. Tetrahedral meshes have higher tendency to a have a higher error than the hexahedral mesh. The explanation for this can be shown on the following figure 8.3

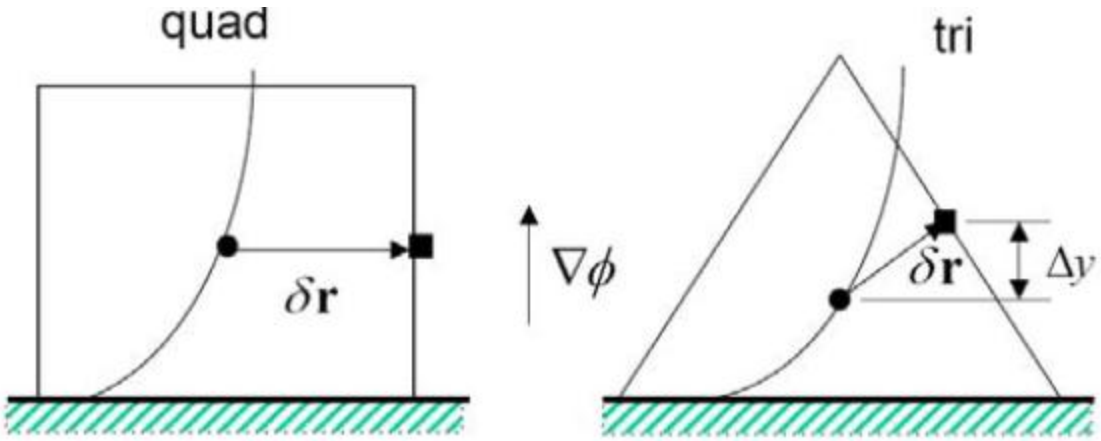

Figure 8.46 – Truncation error for tri/tetrahedral and quad/hexahedral mesh when aligned to the flow direction [22]

$$\varphi_{c0} + \underbrace{\underbrace{\delta r \cdot (\nabla\varphi)_{c0}}_{\neq 0 \; for \; tri/tetrahedral \; mesh}}_{=0 \; for \; quad/hexahedral \; mesh} + O(|\delta r|^2)$$

Other parameters that may contribute to the truncation error are the rapid changes in cell volume between adjacent cells translate into larger truncation errors.

8.1 Charts of nodal stress value

– TETRAHEDRAL MESH

Table 8.22 - 50% Radius Fracture, 1000 rad/s, near fracture line points

"-z"	Node 25	mid	Node 20	"+z"	Node 14
X (s)	Y (Pa)	X (s)	Y (Pa)	X (s)	Y (Pa)
0	0	0	0	0	0
0,05	0,00E+00	0,05	0	0,05	213,177
0,1	0	0,1	0	0,1	0
0,15	0	0,15	0	0,15	0
0,2	250659	0,2	8,22712	0,2	0
0,25	72,5362	0,25	0	0,25	0
0,3	180,119	0,3	0	0,3	26,4262
0,35	37,6827	0,35	21,1181	0,35	0
0,4	0	0,4	0	0,4	0
0,45	0	0,45	0	0,45	0
0,5	0	0,5	0	0,5	0
0,55	0	0,55	0	0,55	0
0,6	0	0,6	0	0,6	0
0,65	0	0,65	0	0,65	0
0,7	0	0,7	0	0,7	0
0,75	0	0,75	0	0,75	0
0,8	0	0,8	0	0,8	0
0,85	0	0,85	0	0,85	0
0,9	0	0,9	0	0,9	0
0,95	0	0,95	0	0,95	0
1	0	1	0	1	0

Table 8.23 - 50% Radius Fracture, 1000 rad/s, mid points

"-z"	Node 29	mid	Node 19	"+z"	Node 13
X (s)	Y (Pa)	X (s)	Y (Pa)	X (s)	Y (Pa)
0	0	0	0	0	0
0,05	0,00E+00	0,05	0,00E+00	0,05	0,00E+00
0,1	0	0,1	0	0,1	0
0,15	0	0,15	0	0,15	0
0,2	3,18E+06	0,2	1,60E+06	0,2	3,35642
0,25	244,989	0,25	1,07E+06	0,25	1,32E+06
0,3	458781	0,3	4,37E+05	0,3	0
0,35	416948	0,35	505860	0,35	18,8301
0,4	0	0,4	0	0,4	0
0,45	0	0,45	0	0,45	0
0,5	0	0,5	56,248	0,5	0
0,55	0	0,55	0	0,55	0
0,6	0	0,6	0	0,6	0
0,65	0	0,65	0	0,65	0
0,7	0	0,7	0	0,7	0
0,75	0	0,75	0	0,75	0
0,8	0	0,8	0	0,8	0
0,85	0	0,85	0	0,85	0
0,9	0	0,9	0	0,9	0
0,95	0	0,95	0	0,95	0
1	0	1	0	1	0

Table 8.24 - 50% Radius Fracture, 1000 rad/s, outer fracture border points

"-z"	Node 28	mid	Node 17	"+z"	Node 16
X (s)	Y (Pa)	X (s)	Y (Pa)	X (s)	Y (Pa)
0	0	0	1,01E-16	0	0
0,05	0,00E+00	0,05	0,00E+00	0,05	0,00E+00
0,1	0	0,1	0	0,1	0
0,15	0	0,15	0	0,15	0
0,2	5,06E+06	0,2	0	0,2	20054,5
0,25	1,20E+06	0,25	8,33E+06	0,25	2,07E+06
0,3	3,38E+06	0,3	9,76E+06	0,3	4,03E+05
0,35	3,49E+06	0,35	1,06E+07	0,35	922199
0,4	0	0,4	0	0,4	0
0,45	0	0,45	0	0,45	0
0,5	1,66E+06	0,5	9,74E+06	0,5	25,6294
0,55	0	0,55	0	0,55	0
0,6	0	0,6	0	0,6	0
0,65	0	0,65	0	0,65	0
0,7	0	0,7	3,61E+06	0,7	0
0,75	0	0,75	3,84E+06	0,75	390880
0,8	0	0,8	0	0,8	0
0,85	0	0,85	0	0,85	0
0,9	0	0,9	0,00E+00	0,9	0,00E+00
0,95	0	0,95	1,49E+07	0,95	776856
1	0	1	0	1	0

Table 8.25 - 50% Radius Fracture, 500 rad/s, near fracture line points

"-z"	Node 9	mid	Node 20	"+z"	Node 14
X (s)	Y (Pa)	X (s)	Y (Pa)	X (s)	Y (Pa)
0	0	0	0	0	0
0,05	1,39E+06	0,05	54,3244	0,05	213,177
0,1	0	0,1	0	0,1	0
0,15	0	0,15	0	0,15	0
0,2	0	0,2	0	0,2	0
0,25	0	0,25	0	0,25	0
0,3	71,7797	0,3	1,46272	0,3	26,4262
0,35	0	0,35	0	0,35	0
0,4	0	0,4	0	0,4	0
0,45	0	0,45	0	0,45	0
0,5	0	0,5	0	0,5	0
0,55	0	0,55	0	0,55	0
0,6	0	0,6	0	0,6	0
0,65	0	0,65	0	0,65	0
0,7	0	0,7	0	0,7	0
0,75	0	0,75	0	0,75	0
0,8	0	0,8	0	0,8	0
0,85	0	0,85	0	0,85	0
0,9	66,0348	0,9	175,209	0,9	0
0,95	0	0,95	0	0,95	0
1	0	1	0	1	0

Table 8.26 - 50% Radius Fracture, 500 rad/s, mid points

"-z"	Node 29	mid	Node 19	"+z"	Node 13
X (s)	Y (Pa)	X (s)	Y (Pa)	X (s)	Y (Pa)
0	0	0	0	0	0
0,05	3,20E+06	0,05	2,47E+06	0,05	1,37E+06
0,1	0	0,1	0	0,1	0
0,15	0	0,15	0	0,15	0
0,2	0	0,2	0	0,2	0
0,25	0	0,25	0	0,25	0
0,3	364902	0,3	1,13E+06	0,3	127310
0,35	0	0,35	0	0,35	0
0,4	0	0,4	0	0,4	0
0,45	0	0,45	0	0,45	0
0,5	0	0,5	0	0,5	0
0,55	0	0,55	0	0,55	0
0,6	0	0,6	0	0,6	0
0,65	0	0,65	0	0,65	0
0,7	0	0,7	0	0,7	0
0,75	0	0,75	0	0,75	0
0,8	0	0,8	0	0,8	0
0,85	0	0,85	0	0,85	0
0,9	24705,9	0,9	631636	0,9	0
0,95	0	0,95	0	0,95	0
1	0	1	0	1	0

Table 8.27 - 50% Radius Fracture, 500 rad/s, outer fracture border points

"-z"	Node 28	mid	Node 17	"+z"	Node 16
X (s)	Y (Pa)	X (s)	Y (Pa)	X (s)	Y (Pa)
0	0	0	1,01E-16	0	0
0,05	4,14E+06	0,05	8,18E+06	0,05	1,40E+06
0,1	0	0,1	0	0,1	0
0,15	0	0,15	0	0,15	0
0,2	0	0,2	0	0,2	0
0,25	0	0,25	0	0,25	0
0,3	2,07E+06	0,3	5,72E+06	0,3	1,43E+06
0,35	0	0,35	0	0,35	0
0,4	0	0,4	0	0,4	0
0,45	0	0,45	0	0,45	0
0,5	0	0,5	0	0,5	0
0,55	0	0,55	0	0,55	0
0,6	0	0,6	0	0,6	0
0,65	0	0,65	0	0,65	0
0,7	0	0,7	0	0,7	0
0,75	0	0,75	0	0,75	0
0,8	0	0,8	0	0,8	0
0,85	0	0,85	0	0,85	0
0,9	660765	0,9	4,33E+06	0,9	1,12E+06
0,95	0	0,95	2,76E+06	0,95	0
1	0	1	0	1	0

Table 8.28 - 75% Radius Fracture, 1000 rad/s, near fracture line points

"-z"	Node 25	mid	Node 20	"+z"	Node 14
X (s)	Y (Pa)	X (s)	Y (Pa)	X (s)	Y (Pa)
0	0	0	2,00E-14	0	0
0,05	0,00E+00	0,05	0	0,05	0
0,1	0	0,1	0	0,1	0
0,15	0	0,15	1,24E+06	0,15	1626,66
0,2	0	0,2	218,571	0,2	3537,29
0,25	0	0,25	0	0,25	0
0,3	0	0,3	0	0,3	0
0,35	0	0,35	0	0,35	0
0,4	13509,7	0,4	0	0,4	0
0,45	0	0,45	0	0,45	0
0,5	19548,4	0,5	0	0,5	0
0,55	19981,6	0,55	0	0,55	0
0,6	17462,2	0,6	0	0,6	0
0,65	23054,8	0,65	0	0,65	0
0,7	29542,7	0,7	13137,5	0,7	0
0,75	27782,4	0,75	27107,2	0,75	0
0,8	33170,7	0,8	66451,7	0,8	0
0,85	39762,5	0,85	39725,3	0,85	0
0,9	43907,4	0,9	68346,3	0,9	0
0,95	35926,6	0,95	46507,2	0,95	0
1	48190,9	1	33567	1	0

Table 8.29 - 75% Radius Fracture, 1000 rad/s, mid points

"-z"	Node 29	mid	Node 19	"+z"	Node 13
X (s)	Y (Pa)	X (s)	Y (Pa)	X (s)	Y (Pa)
0	7,52E-15	0	1,46E-14	0	0
0,05	0,00E+00	0,05	0,00E+00	0,05	0,00E+00
0,1	167,926	0,1	117,42	0,1	0
0,15	1071,49	0,15	1,49E+06	0,15	3,45E+06
0,2	2,17E+07	0,2	2,39E+08	0,2	1,08E+07
0,25	3,84E+06	0,25	2,28E+08	0,25	8,89E+06
0,3	1,12E+07	0,3	1,66E+08	0,3	21363
0,35	26005,2	0,35	1,34E+08	0,35	39197,5
0,4	1,02E+07	0,4	1,12E+08	0,4	41496,7
0,45	112404	0,45	1,17E+08	0,45	70976,8
0,5	1,51E+07	0,5	1,18E+08	0,5	33486,4
0,55	1,47E+07	0,55	1,18E+08	0,55	14202,7
0,6	2,09E+07	0,6	1,25E+08	0,6	0
0,65	4,36E+06	0,65	1,21E+08	0,65	0
0,7	2,85E+06	0,7	1,09E+08	0,7	65375
0,75	32205,7	0,75	1,06E+08	0,75	43820,4
0,8	1,54E+07	0,8	1,11E+08	0,8	0
0,85	2,61E+06	0,85	1,18E+08	0,85	32210,9
0,9	7,03E+06	0,9	1,12E+08	0,9	21659,9
0,95	2,81E+06	0,95	1,08E+08	0,95	114875
1	1,31E+07	1	1,12E+08	1	187462

Table 8.30 - 75% Radius Fracture, 1000 rad/s, outer fracture border points

"-z"	Node 30	mid	Node 17	"+z"	Node 16
X (s)	Y (Pa)	X (s)	Y (Pa)	X (s)	Y (Pa)
0	0	0	0,00E+00	0	0
0,05	0,00E+00	0,05	0,00E+00	0,05	0,00E+00
0,1	1,54E+06	0,1	3,91E+06	0,1	0
0,15	1,56E+06	0,15	8,69E+06	0,15	1,46E+06
0,2	2,42E+07	0,2	1,13E+09	0,2	1,80E+07
0,25	1,44E+07	0,25	1,10E+09	0,25	2,12E+07
0,3	2,02E+07	0,3	9,72E+08	0,3	1,10E+08
0,35	2,06E+07	0,35	9,04E+08	0,35	1,02E+08
0,4	2,42E+07	0,4	8,55E+08	0,4	8,07E+07
0,45	2,34E+07	0,45	8,71E+08	0,45	8,79E+07
0,5	2,91E+07	0,5	8,67E+08	0,5	8,80E+07
0,55	3,07E+07	0,55	8,72E+08	0,55	8,48E+07
0,6	3,45E+07	0,6	8,91E+08	0,6	9,18E+07
0,65	3,16E+07	0,65	8,96E+08	0,65	9,93E+07
0,7	2,48E+07	0,7	8,72E+08	0,7	8,75E+07
0,75	1,84E+07	0,75	8,71E+08	0,75	8,56E+07
0,8	2,66E+07	0,8	8,81E+08	0,8	9,24E+07
0,85	3,25E+07	0,85	9,04E+08	0,85	1,01E+08
0,9	3,39E+07	0,9	9,15E+08	0,9	1,31E+08
0,95	2,86E+07	0,95	9,10E+08	0,95	1,30E+08
1	3,53E+07	1	9,21E+08	1	1,28E+08

Table 8.31 - 75% Radius Fracture, 500 rad/s, near fracture line points

"-z"	Node 25	mid	Node 20	"+z"	Node 14
X (s)	Y (Pa)	X (s)	Y (Pa)	X (s)	Y (Pa)
0	0	0	0	0	0
0,05	0,00E+00	0,05	0	0,05	213,177
0,1	0	0,1	0	0,1	0
0,15	189,744	0,15	3026,2	0,15	0
0,2	572,321	0,2	10304,4	0,2	0
0,25	586,447	0,25	4983,58	0,25	0
0,3	1667,19	0,3	7030,57	0,3	26,4262
0,35	2791,85	0,35	7384,58	0,35	0
0,4	2431,94	0,4	8864,97	0,4	0
0,45	4684,78	0,45	12119,5	0,45	0
0,5	3313,05	0,5	10183,5	0,5	0
0,55	3964,87	0,55	5014,23	0,55	0
0,6	0	0,6	0	0,6	0
0,65	0	0,65	0	0,65	0
0,7	0	0,7	0	0,7	0
0,75	0	0,75	0	0,75	0
0,8	0	0,8	0	0,8	0
0,85	0	0,85	0	0,85	0
0,9	0	0,9	0	0,9	0
0,95	0	0,95	0	0,95	0
1	0	1	0	1	0

Table 8.32 - 75% Radius Fracture, 500 rad/s, mid points

"-z"	Node 29	mid	Node 19	"+z"	Node 13
X (s)	Y (Pa)	X (s)	Y (Pa)	X (s)	Y (Pa)
0	0	0	6,86E-15	0	0
0,05	0,00E+00	0,05	0,00E+00	0,05	1,37E+06
0,1	0	0,1	0	0,1	0
0,15	0	0,15	3,00E+06	0,15	0
0,2	0	0,2	8,94E+06	0,2	0
0,25	0	0,25	5,17E+06	0,25	0
0,3	0	0,3	9,91E+06	0,3	127310
0,35	0	0,35	1,63E+07	0,35	0
0,4	0	0,4	1,19E+07	0,4	0
0,45	0	0,45	1,99E+07	0,45	0
0,5	0	0,5	1,77E+07	0,5	0
0,55	0	0,55	1,73E+07	0,55	0
0,6	0	0,6	0	0,6	0
0,65	0	0,65	0	0,65	0
0,7	0	0,7	0	0,7	0
0,75	0	0,75	0	0,75	0
0,8	0	0,8	0	0,8	0
0,85	0	0,85	0	0,85	0
0,9	0	0,9	0	0,9	0
0,95	0	0,95	0	0,95	0
1	0	1	0	1	0

Table 8.33 - 75% Radius Fracture, 500 rad/s, outer fracture border points

"-z"	Node 30	mid	Node 17	"+z"	Node 16
X (s)	Y (Pa)	X (s)	Y (Pa)	X (s)	Y (Pa)
0	0	0	0,00E+00	0	0
0,05	0,00E+00	0,05	0,00E+00	0,05	0,00E+00
0,1	0	0,1	0	0,1	0
0,15	0	0,15	0	0,15	0
0,2	0	0,2	0	0,2	0
0,25	0	0,25	0	0,25	0
0,3	0,00E+00	0,3	0,00E+00	0,3	0,00E+00
0,35	0	0,35	0	0,35	0
0,4	0	0,4	0	0,4	0
0,45	0	0,45	0	0,45	0
0,5	0	0,5	0	0,5	0
0,55	0	0,55	0	0,55	0
0,6	0	0,6	0	0,6	296264
0,65	0	0,65	0	0,65	337701
0,7	0	0,7	0	0,7	471291
0,75	0	0,75	0	0,75	503396
0,8	0	0,8	0	0,8	574207
0,85	0	0,85	0	0,85	576477
0,9	0	0,9	0,00E+00	0,9	4,73E+05
0,95	0	0,95	0,00E+00	0,95	484317
1	0	1	0	1	420546

Table 8.34 - 90% Radius Fracture, 1000 rad/s, near fracture line points

"-z"	Node 23	mid	Node 17	"+z"	Node 12
X (s)	Y (Pa)	X (s)	Y (Pa)	X (s)	Y (Pa)
0	0	0	0	0	0
0,05	0,00E+00	0,05	0	0,05	0
0,1	0	0,1	0	0,1	0
0,15	0	0,15	0	0,15	0
0,2	0	0,2	0	0,2	0
0,25	0	0,25	0	0,25	0
0,3	0	0,3	0	0,3	0
0,35	0	0,35	0	0,35	0
0,4	0	0,4	0	0,4	129996
0,45	0	0,45	0	0,45	0
0,5	0	0,5	0	0,5	0
0,55	6818,85	0,55	0	0,55	0
0,6	0	0,6	0	0,6	0
0,65	0	0,65	0	0,65	0
0,7	0	0,7	0	0,7	0
0,75	0	0,75	0	0,75	0
0,8	0	0,8	0	0,8	0
0,85	0	0,85	0	0,85	0
0,9	0	0,9	0	0,9	0
0,95	0	0,95	0	0,95	0
1	0	1	0	1	0

Table 8.35 - 90% Radius Fracture, 1000 rad/s, mid points

mid	Node 17
X (s)	Y (Pa)
0	0
0,05	0,00E+00
0,1	0
0,15	0
0,2	0,00E+00
0,25	0,00E+00
0,3	3,30E+03
0,35	4,85E+04
0,4	9,35E+04
0,45	0,00E+00
0,5	0,00E+00
0,55	2,14E+03
0,6	0,00E+00
0,65	0,00E+00
0,7	0,00E+00
0,75	0,00E+00
0,8	0,00E+00
0,85	0,00E+00
0,9	0,00E+00
0,95	0,00E+00
1	0,00E+00

Table 8.36 - 90% Radius Fracture, 1000 rad/s, outer fracture border points

"-z"	Node 22	mid	Node 15	"+z"	Node 14
X (s)	Y (Pa)	X (s)	Y (Pa)	X (s)	Y (Pa)
0	0	0	0,00E+00	0	0
0,05	0,00E+00	0,05	0,00E+00	0,05	0,00E+00
0,1	0	0,1	0	0,1	0
0,15	0	0,15	0	0,15	0
0,2	3,22E+06	0,2	1,68E+07	0,2	0
0,25	0,00E+00	0,25	0,00E+00	0,25	0,00E+00
0,3	9,51E+02	0,3	4,43E+06	0,3	0,00E+00
0,35	1,38E+07	0,35	2,20E+07	0,35	1,07E+07
0,4	19600,4	0,4	2,16E+07	0,4	8,85E+07
0,45	0	0,45	0,00E+00	0,45	0,00E+00
0,5	0,00E+00	0,5	0,00E+00	0,5	0
0,55	2,24E+06	0,55	0,00E+00	0,55	0,00E+00
0,6	0	0,6	0,00E+00	0,6	0,00E+00
0,65	0	0,65	0,00E+00	0,65	0,00E+00
0,7	4,33E+06	0,7	0,00E+00	0,7	0
0,75	0	0,75	0,00E+00	0,75	0,00E+00
0,8	0	0,8	0,00E+00	0,8	0,00E+00
0,85	0	0,85	0,00E+00	0,85	0,00E+00
0,9	0	0,9	0,00E+00	0,9	0,00E+00
0,95	0	0,95	0,00E+00	0,95	0,00E+00
1	0	1	0,00E+00	1	0,00E+00

Table 8.37 - 90% Radius Fracture, 500 rad/s, near fracture line points

"-z"	Node 23	mid	Node 17	"+z"	Node 12
X (s)	Y (Pa)	X (s)	Y (Pa)	X (s)	Y (Pa)
0	0	0	0	0	0
0,05	0,00E+00	0,05	0	0,05	0
0,1	0	0,1	0	0,1	0
0,15	0	0,15	0	0,15	0
0,2	0	0,2	0	0,2	0
0,25	0	0,25	0	0,25	0
0,3	0	0,3	2579,51	0,3	0
0,35	0	0,35	13998,6	0,35	0
0,4	0	0,4	22436,5	0,4	0
0,45	262,507	0,45	23986,6	0,45	0
0,5	0	0,5	13347,9	0,5	0
0,55	0	0,55	20326,2	0,55	0
0,6	0	0,6	26852,7	0,6	0
0,65	0	0,65	35429,6	0,65	0
0,7	0	0,7	24746,9	0,7	0
0,75	0	0,75	26469	0,75	0
0,8	0	0,8	26872,4	0,8	0
0,85	0	0,85	34566,3	0,85	0
0,9	0	0,9	25294,6	0,9	0
0,95	0	0,95	16803,4	0,95	0
1	0	1	0	1	0

Table 8.38 - 90% Radius Fracture, 500 rad/s, mid points

mid	Node 17
X (s)	Y (Pa)
0	0
0,05	1,95E+03
0,1	0
0,15	0
0,2	0,00E+00
0,25	3,43E+06
0,3	6,44E+06
0,35	1,02E+07
0,4	1,16E+07
0,45	8,62E+06
0,5	1,09E+07
0,55	8,58E+06
0,6	8,75E+06
0,65	1,31E+07
0,7	1,05E+07
0,75	7,11E+06
0,8	6,50E+06
0,85	1,08E+07
0,9	9,41E+06
0,95	7,63E+06
1	1,39E+07

Table 8.39 - 90% Radius Fracture, 500 rad/s, outer fracture border points

"-z"	Node 22	mid	Node 15	"+z"	Node 14
X (s)	Y (Pa)	X (s)	Y (Pa)	X (s)	Y (Pa)
0	0	0	0,00E+00	0	0
0,05	8,49E+01	0,05	1,68E+06	0,05	0,00E+00
0,1	0	0,1	0	0,1	0
0,15	0	0,15	0	0,15	0
0,2	0,00E+00	0,2	0	0,2	0
0,25	0,00E+00	0,25	6,18E+03	0,25	5,22E+02
0,3	4,28E+06	0,3	5,68E+06	0,3	5,43E+02
0,35	3,40E+06	0,35	1,31E+07	0,35	3,48E+06
0,4	11151,3	0,4	2,54E+07	0,4	222989
0,45	436643	0,45	1,43E+07	0,45	6,64E+06
0,5	1,36E+04	0,5	2,48E+07	0,5	336357
0,55	4,16E+06	0,55	2,52E+07	0,55	9,15E+06
0,6	12155,2	0,6	1,74E+07	0,6	7,16E+06
0,65	23767,9	0,65	2,63E+07	0,65	2,25E+06
0,7	16975,7	0,7	2,26E+07	0,7	469767
0,75	13449,3	0,75	2,33E+07	0,75	9,40E+06
0,8	8130,53	0,8	1,31E+07	0,8	9,01E+06
0,85	18561,6	0,85	2,41E+07	0,85	2,08E+06
0,9	14378,7	0,9	2,38E+07	0,9	2,22E+05
0,95	13771	0,95	2,95E+07	0,95	1,07E+07
1	3789,01	1	9,05E+06	1	1,70E+07

8.2 Graphics of the tetrahedral mesh simulation

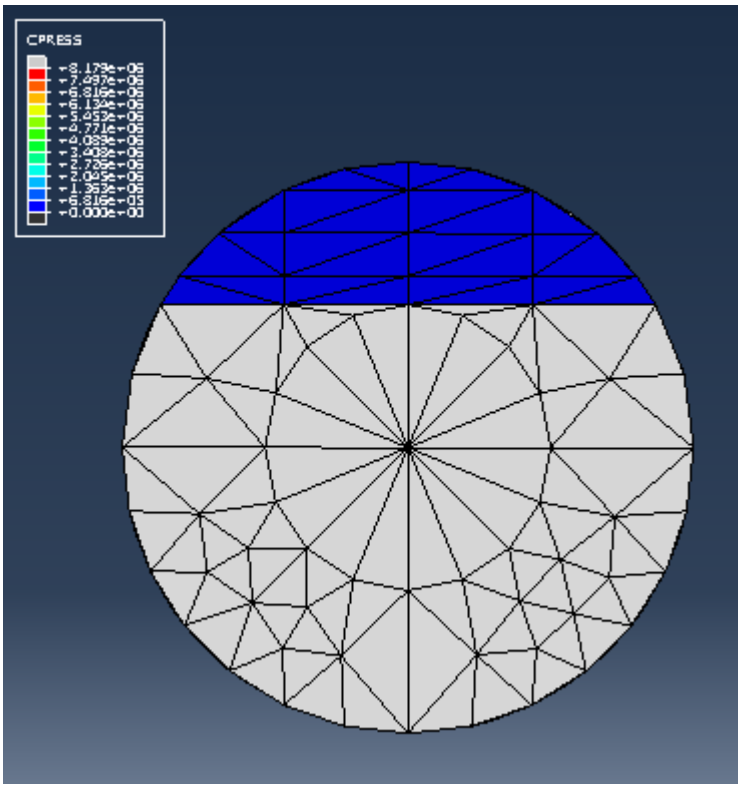

Figure 8.47 - Tetrahedral mesh, 50% Shaft fracture at 500 rad/s, step time: 0,0 s

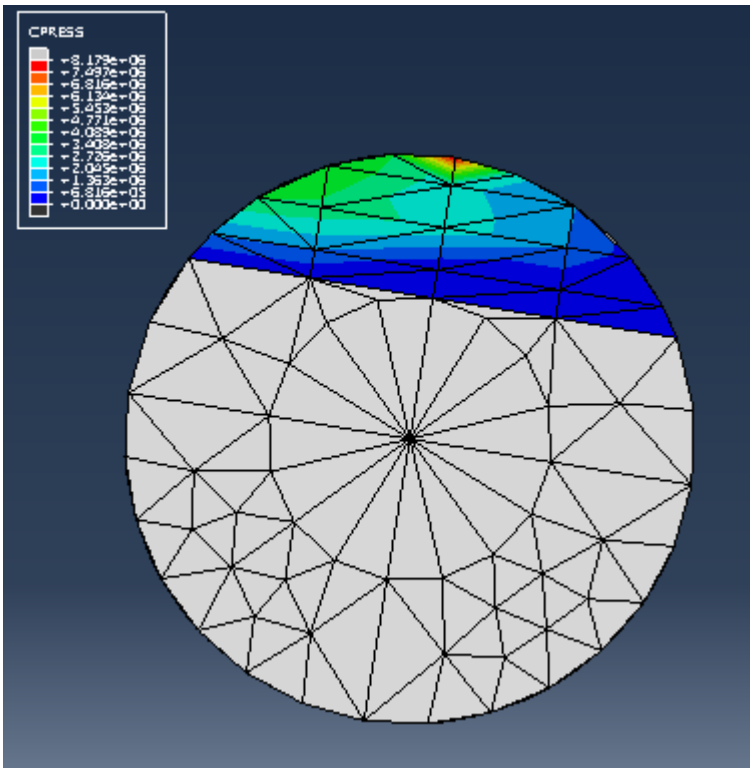

Figure 8.48 - Tetrahedral mesh, 50% Shaft fracture at 500 rad/s, step time: 0,05 s

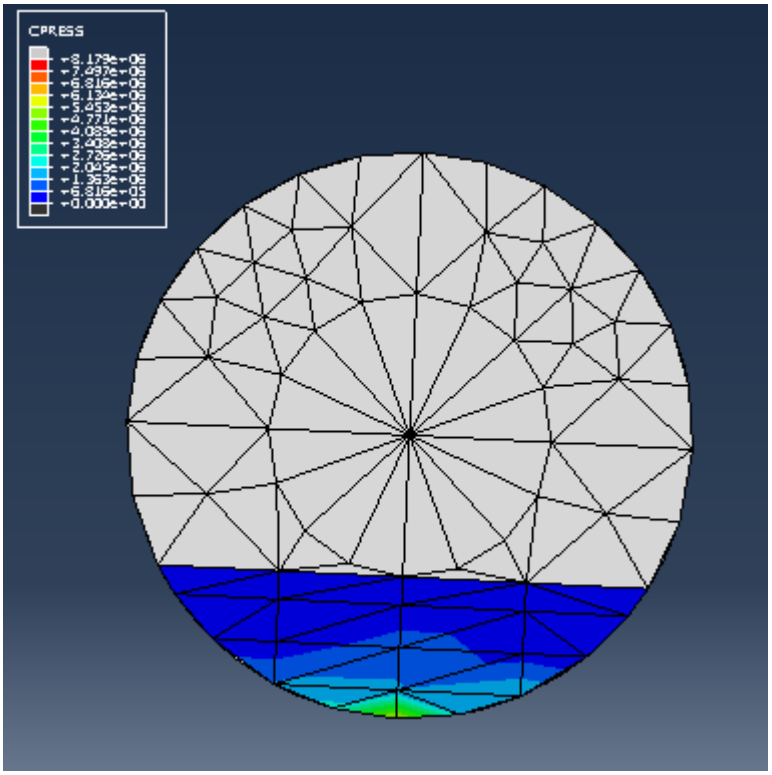

Figure 8.49 - Tetrahedral mesh, 50% Shaft fracture at 500 rad/s, step time: 0,3 s

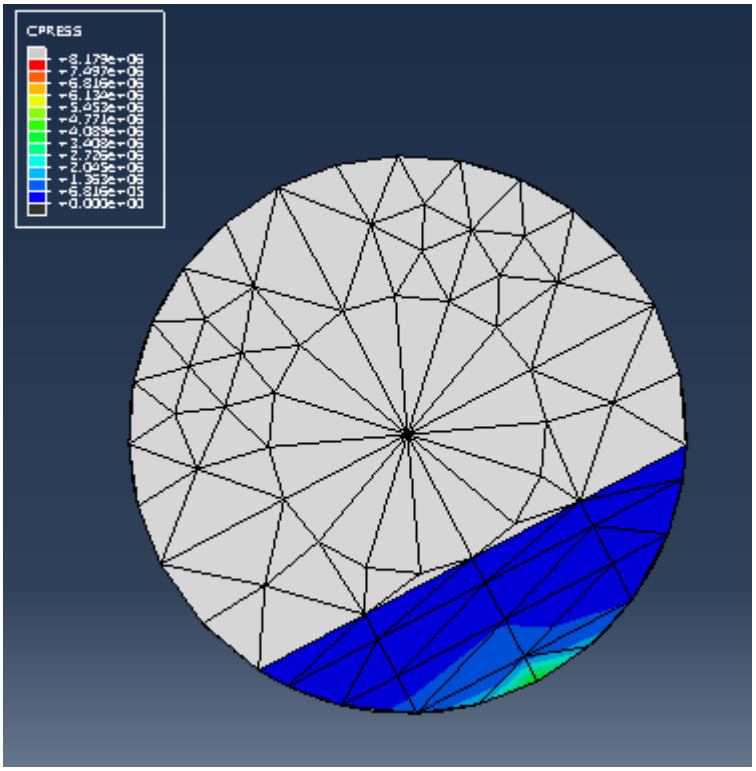

Figure 8.50 - Tetrahedral mesh, 50% Shaft fracture at 500 rad/s, step time: 0,9 s

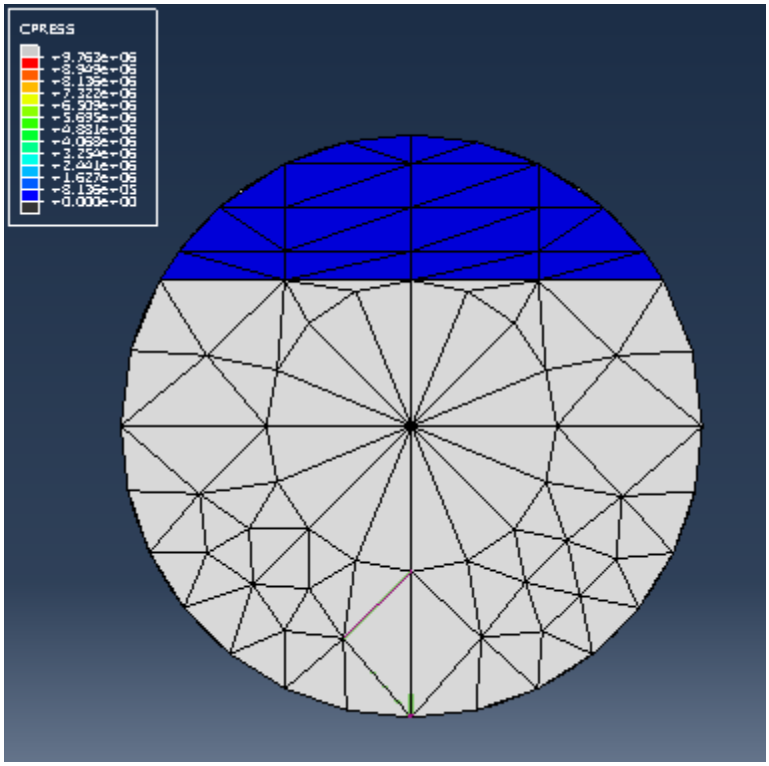

Figure 8.51 - - Tetrahedral mesh, 50% Shaft fracture at 1000 rad/s, step time: 0,0 s

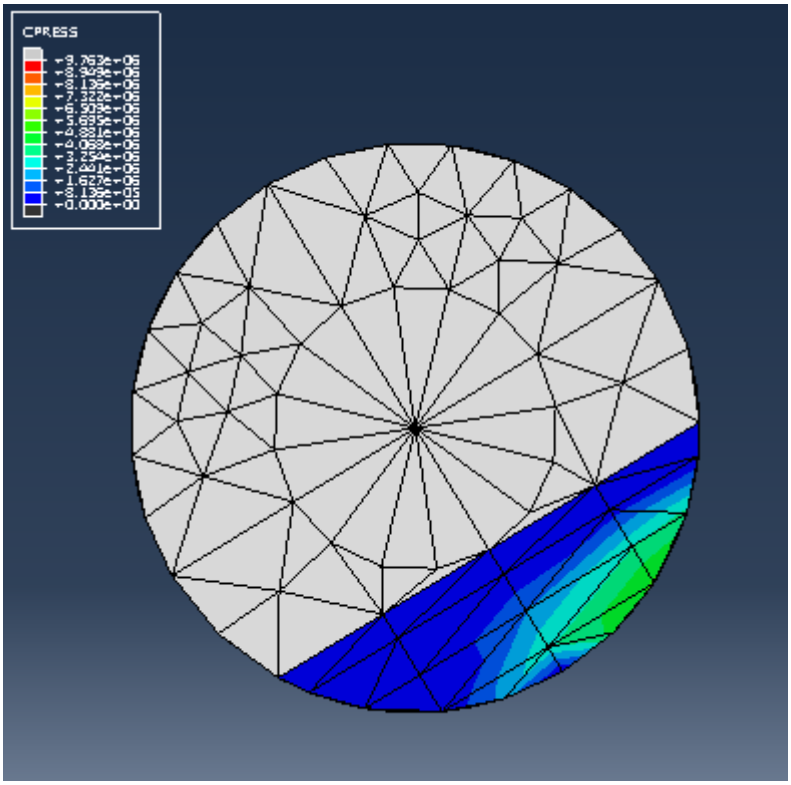

Figure 8.52 - Tetrahedral mesh, 50% Shaft fracture at 1000 rad/s, step time: 0,20 s

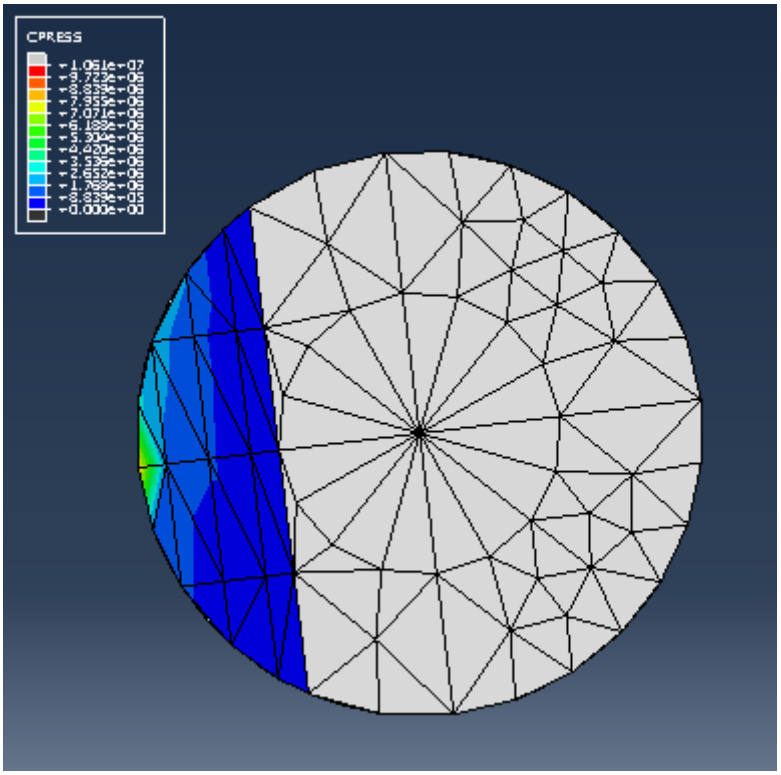

Figure 8.53 - Tetrahedral mesh, 50% Shaft fracture at 1000 rad/s, step time: 0,25 s

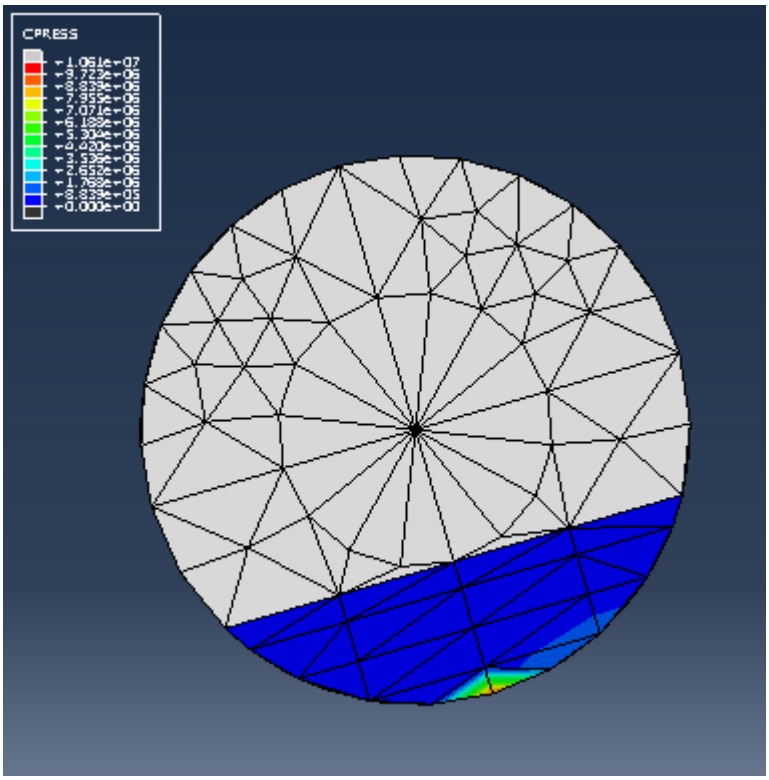

Figure 8.54 - Tetrahedral mesh, 50% Shaft fracture at 1000 rad/s, step time: 0,50 s

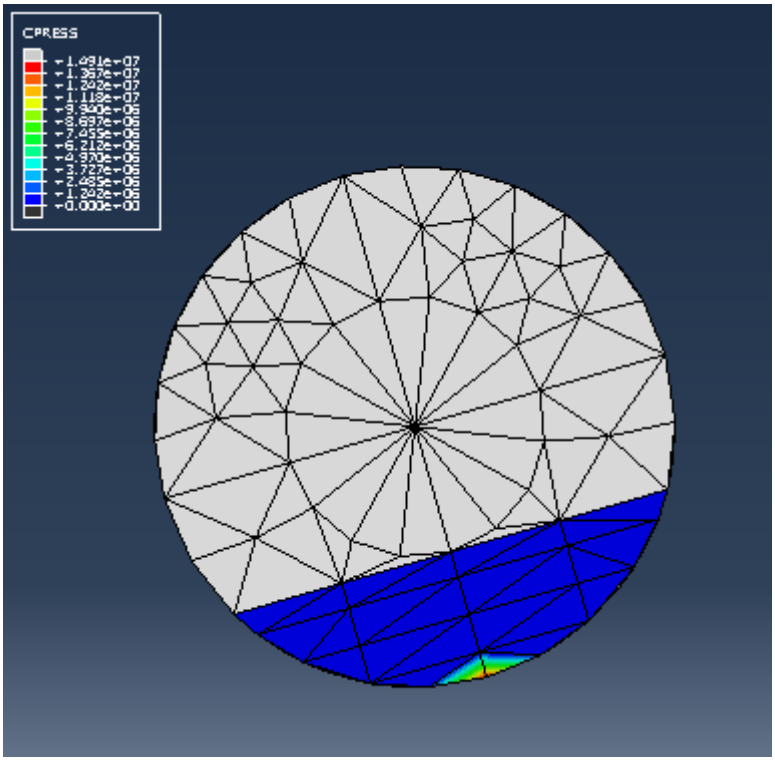

Figure 8.55 - Tetrahedral mesh, 50% Shaft fracture at 1000 rad/s, step time: 0,95 s

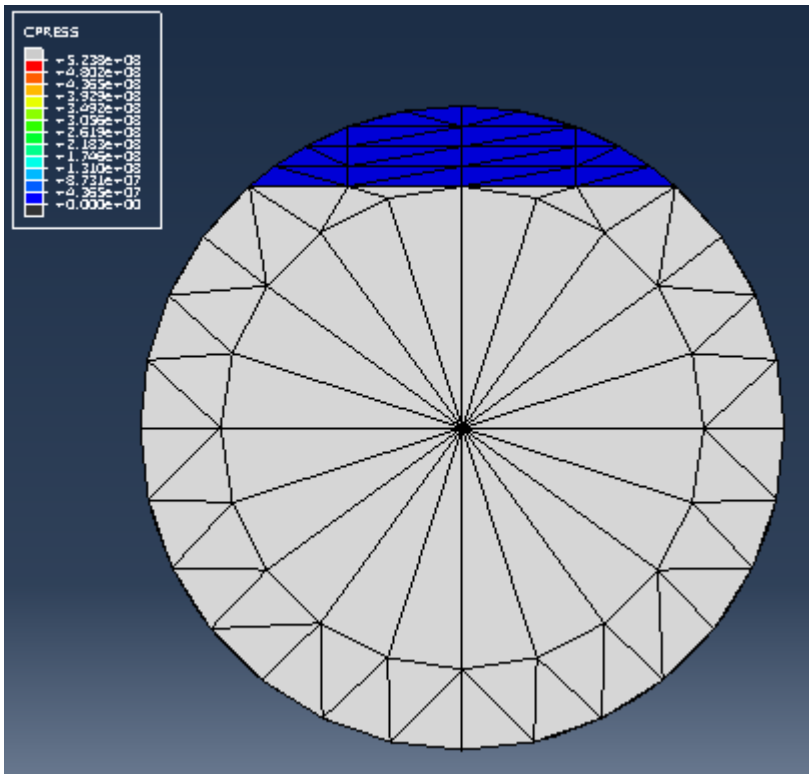

Figure 8.56 - Tetrahedral mesh, 25% Shaft fracture at 500 rad/s, step time: 0,05 s

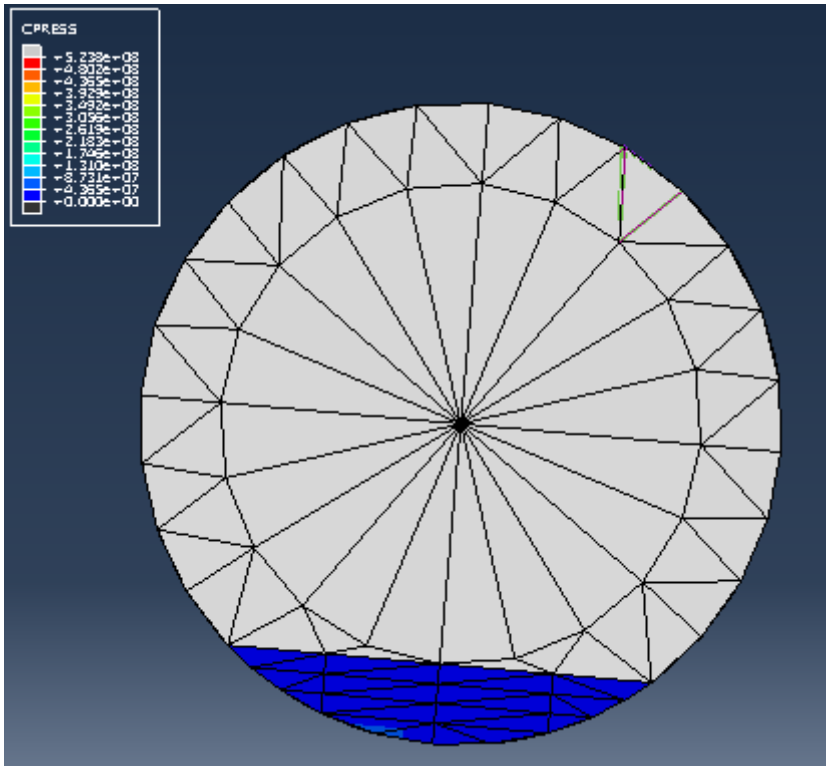

Figure 8.57 - Tetrahedral mesh, 25% Shaft fracture at 500 rad/s, step time: 0,2 s

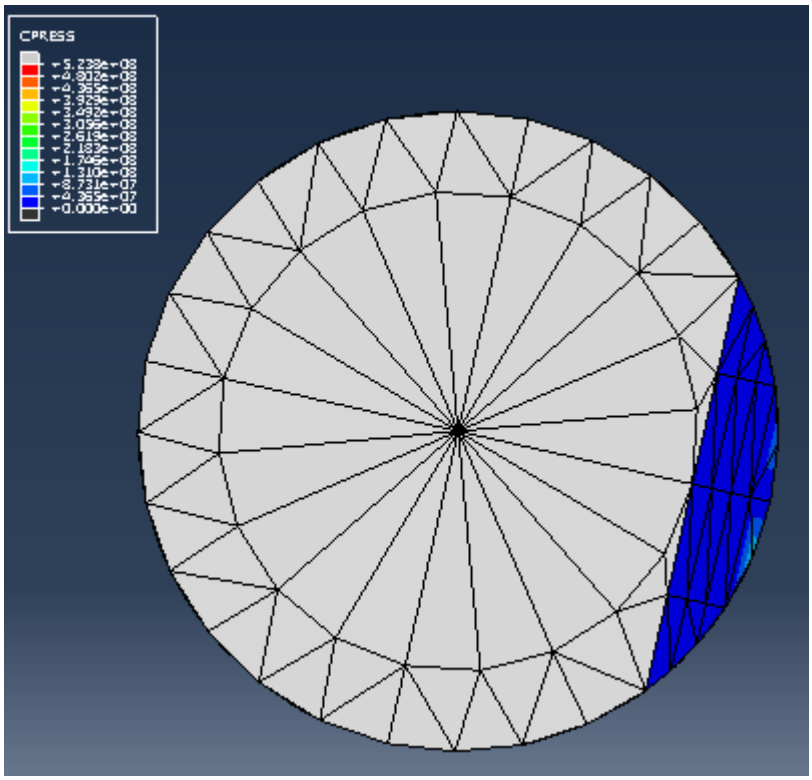

Figure 8.58 - Tetrahedral mesh, 25% Shaft fracture at 500 rad/s, step time: 0,35 s

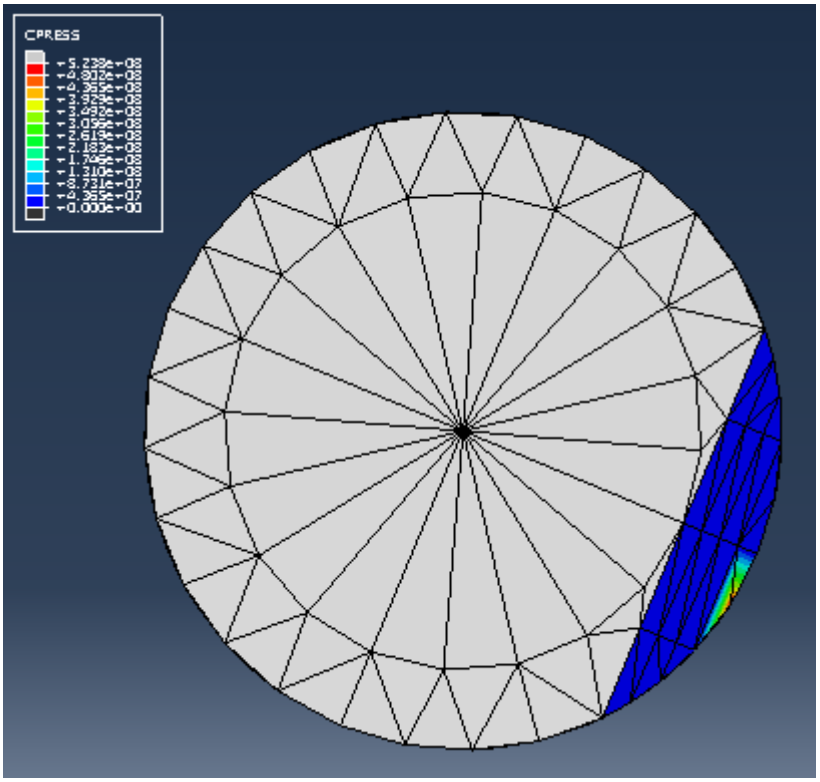

Figure 8.59 - Tetrahedral mesh, 25% Shaft fracture at 500 rad/s, step time: 0,60 s

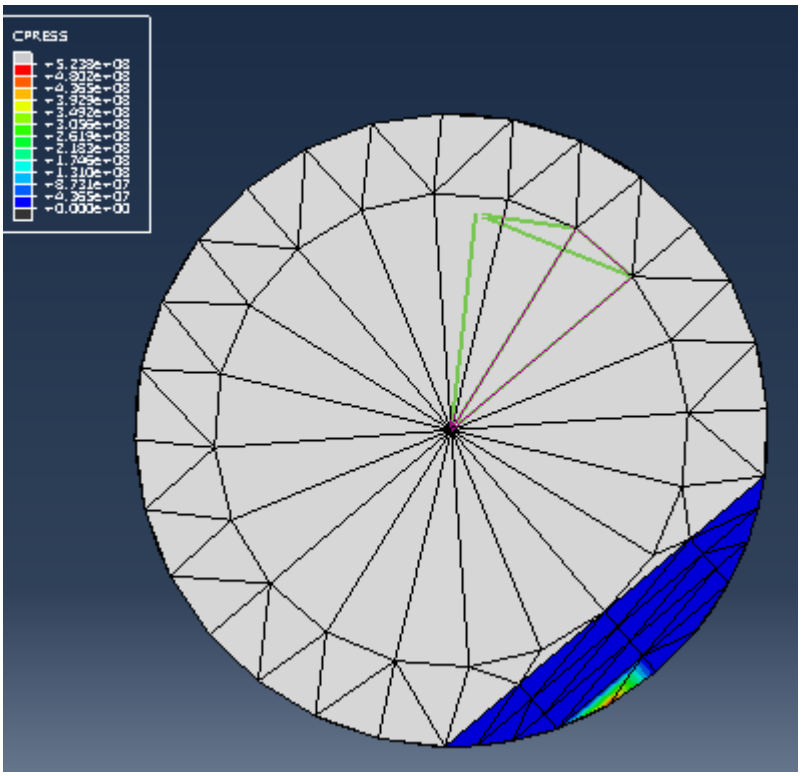

Figure 8.60 - Tetrahedral mesh, 25% Shaft fracture at 500 rad/s, step time: 1,0 s

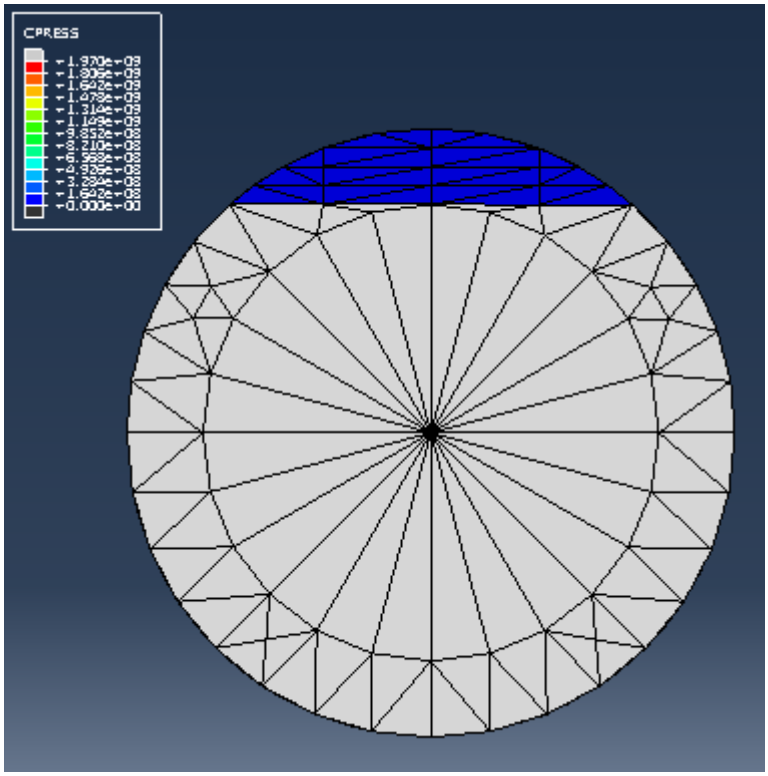

Figure 8.61 - Tetrahedral mesh, 25% Shaft fracture at 1000 rad/s, step time: 0,0 s

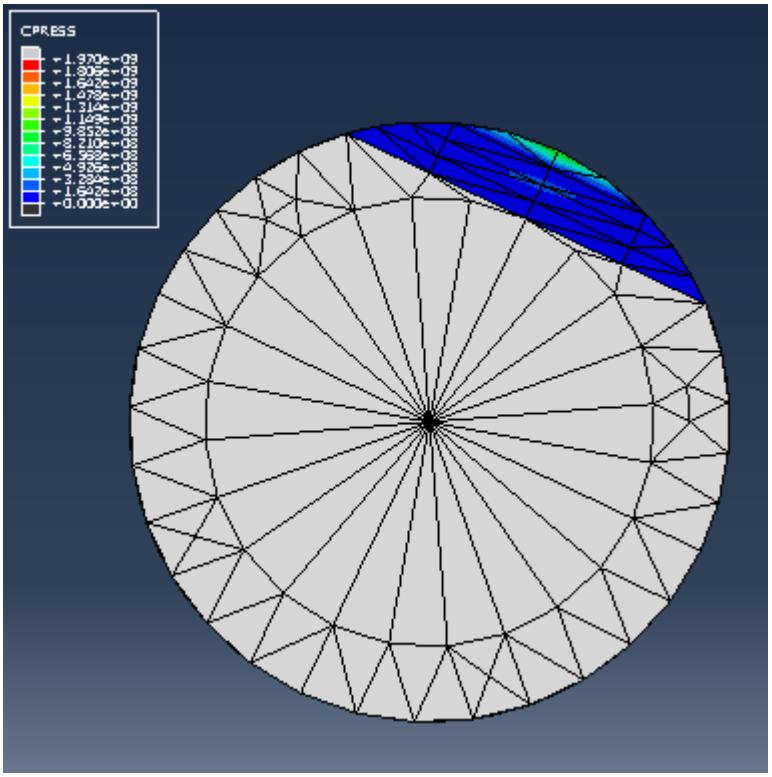

Figure 8.62 - Tetrahedral mesh, 25% Shaft fracture at 1000 rad/s, step time: 0,20 s

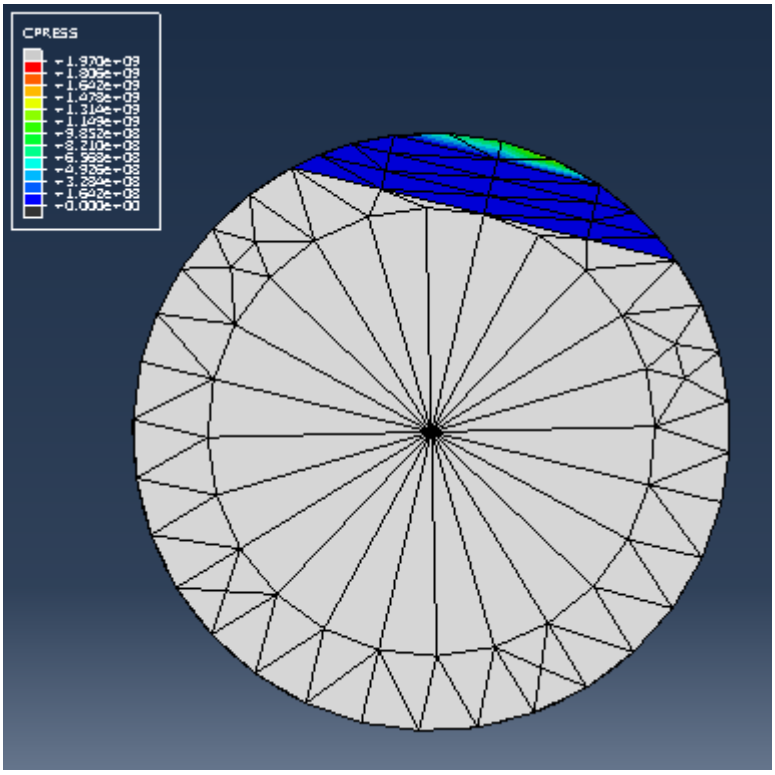

Figure 8.63 - Tetrahedral mesh, 25% Shaft fracture at 1000 rad/s, step time: 0,30 s

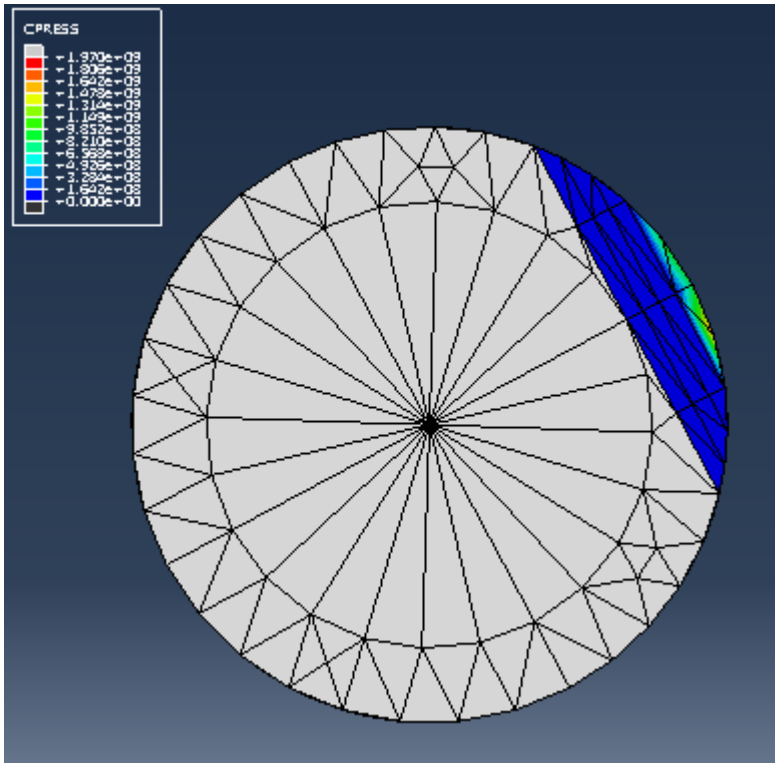

Figure 8.64 - Tetrahedral mesh, 25% Shaft fracture at 1000 rad/s, step time: 0,35 s

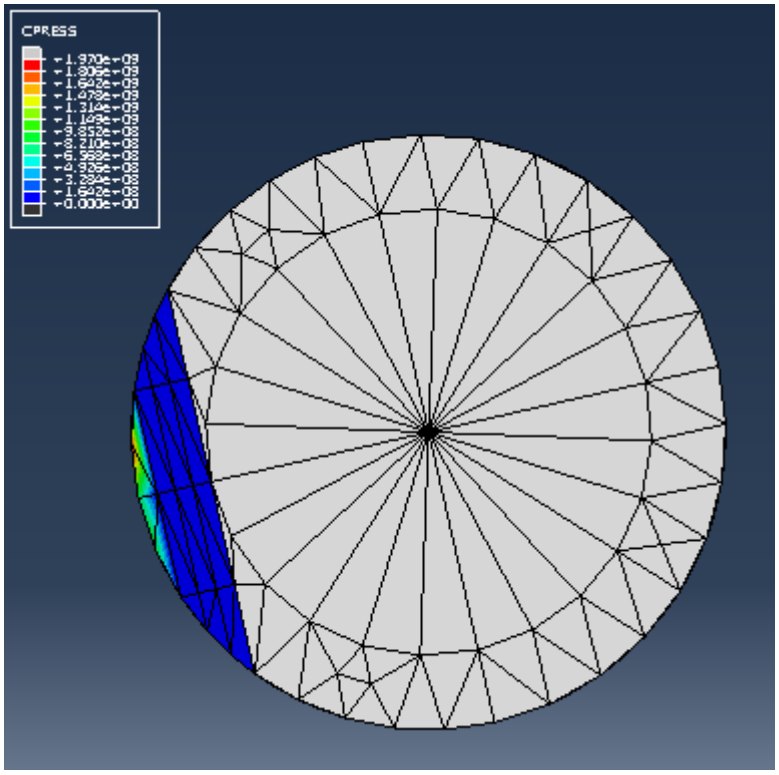

Figure 8.65 - Tetrahedral mesh, 25% Shaft fracture at 1000 rad/s, step time: 0,40 s

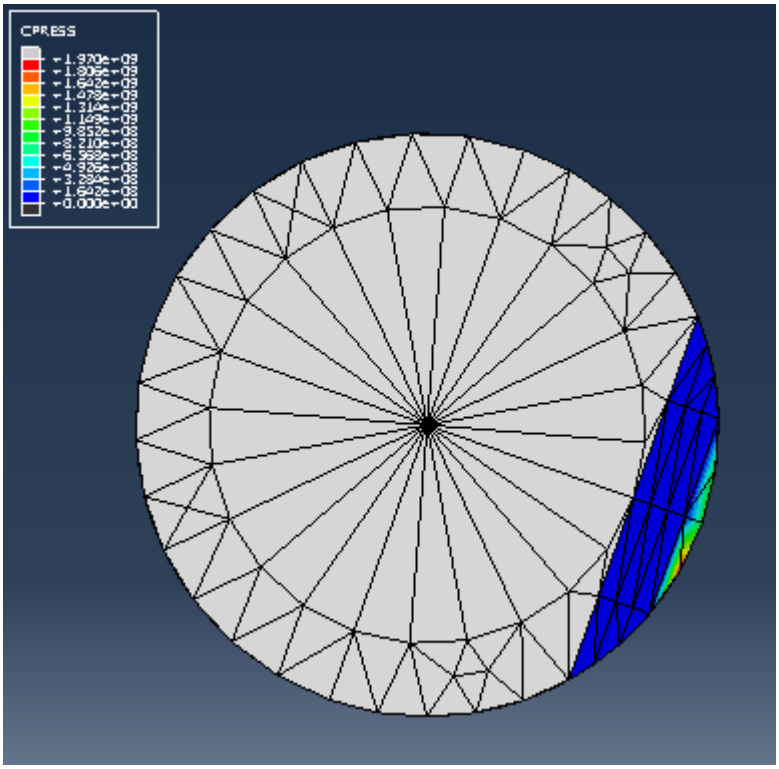

Figure 8.66 - Tetrahedral mesh, 25% Shaft fracture at 1000 rad/s, step time: 1,0 s

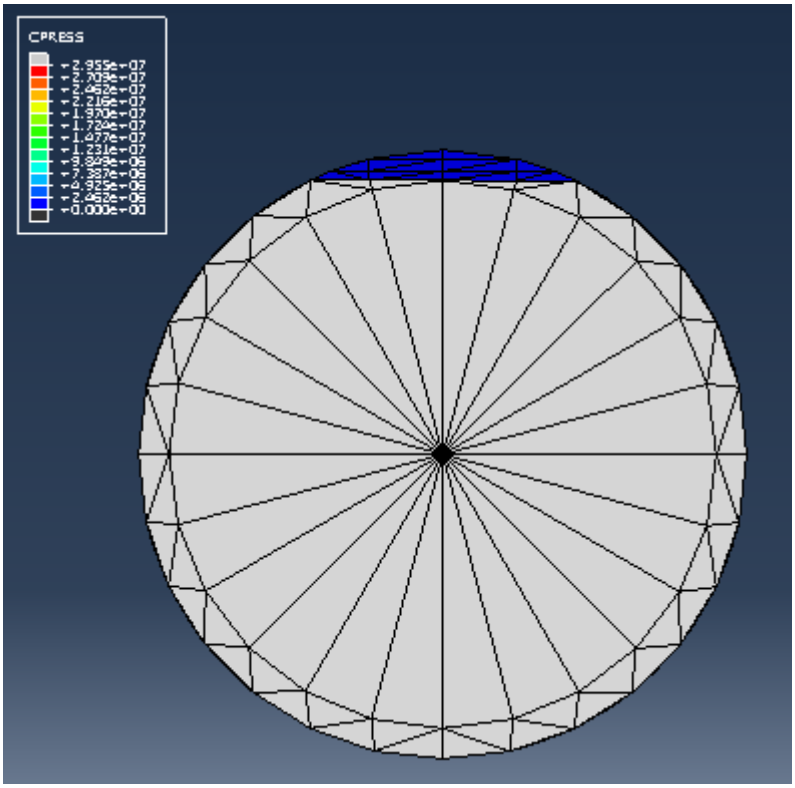

Figure 8.67 - Tetrahedral mesh, 10% Shaft fracture at 500 rad/s, step time: 0,0 s

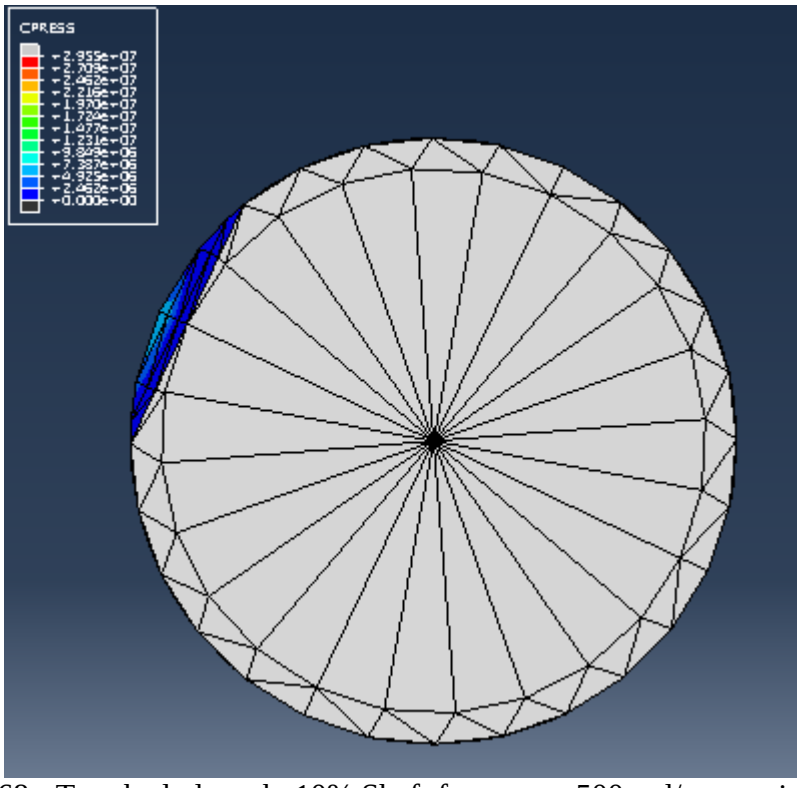

Figure 8.68 - Tetrahedral mesh, 10% Shaft fracture at 500 rad/s, step time: 0,30 s

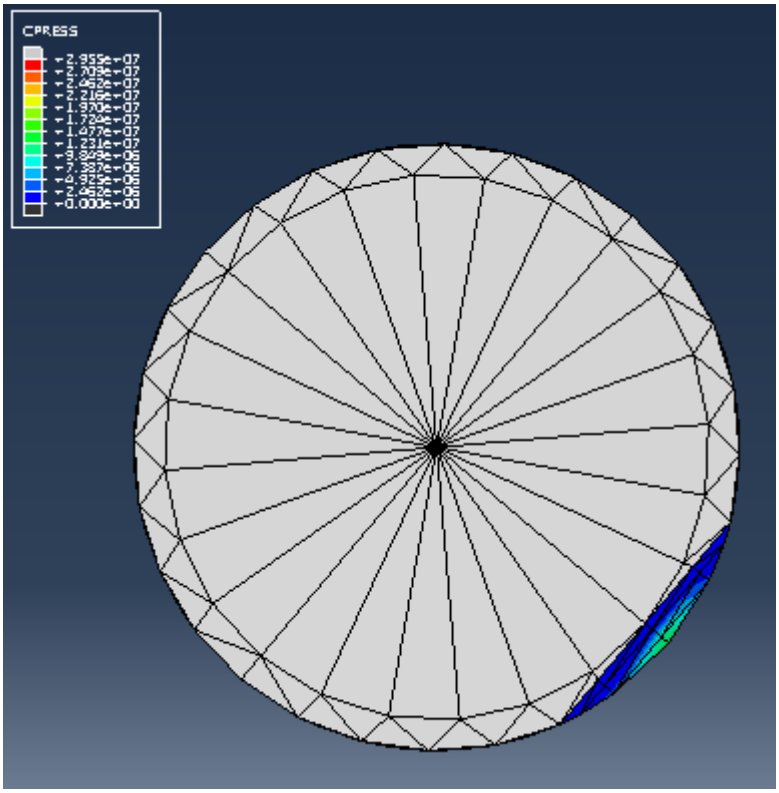

Figure 8.69 - Tetrahedral mesh, 10% Shaft fracture at 500 rad/s, step time: 0,35 s

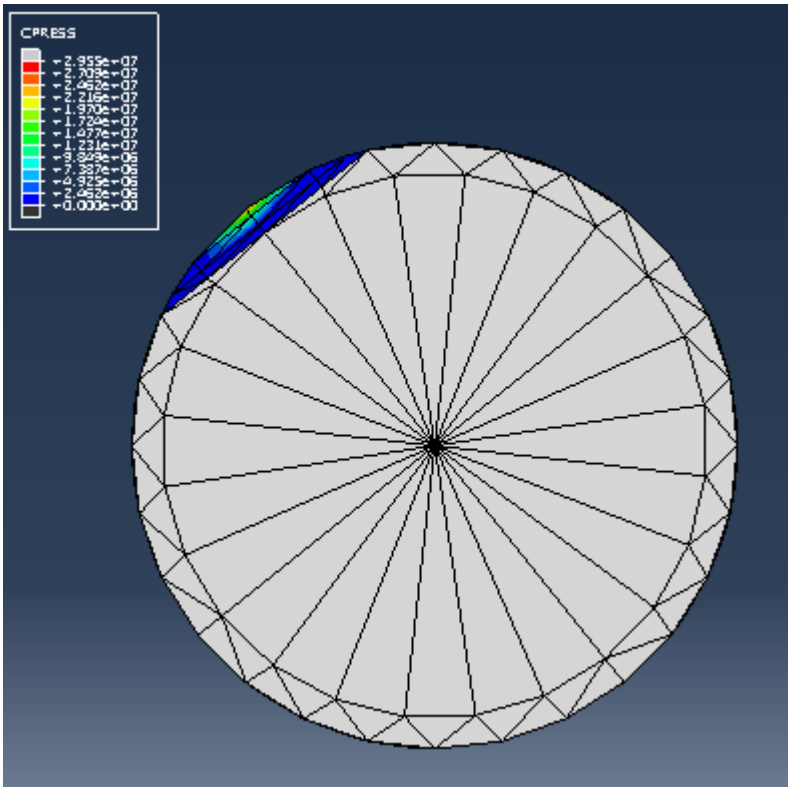

Figure 8.70 - Tetrahedral mesh, 10% Shaft fracture at 500 rad/s, step time: 0,40 s

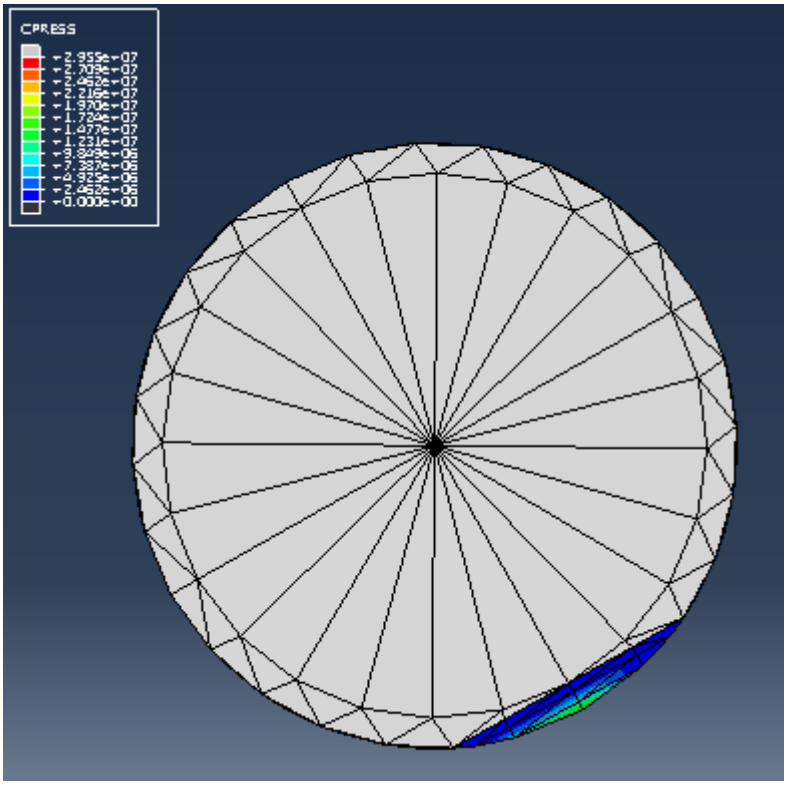

Figure 8.71 - Tetrahedral mesh, 10% Shaft fracture at 500 rad/s, step time: 0,60 s

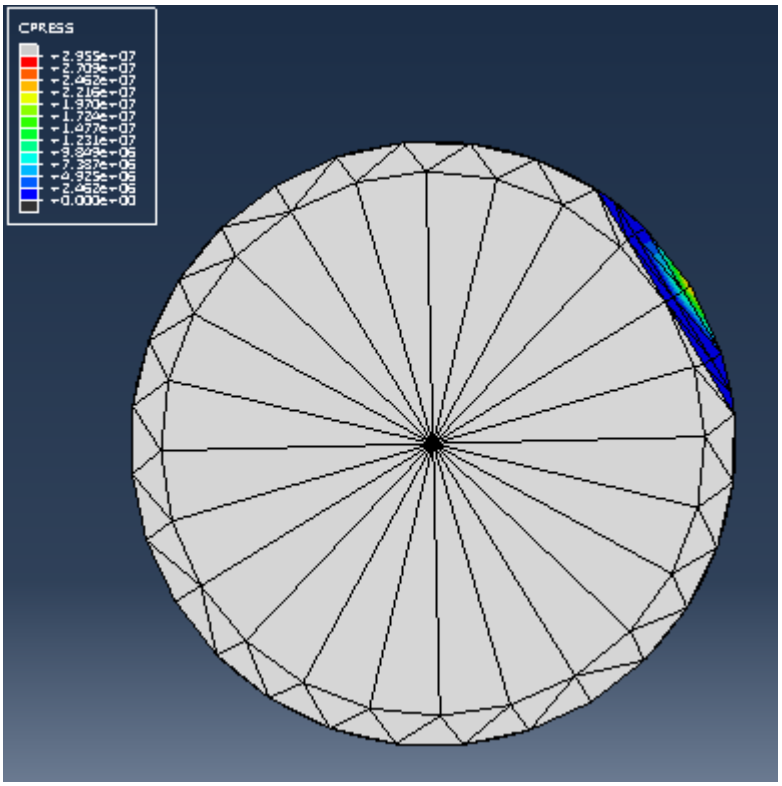

Figure 8.72 - Tetrahedral mesh, 10% Shaft fracture at 500 rad/s, step time: 0,65 s

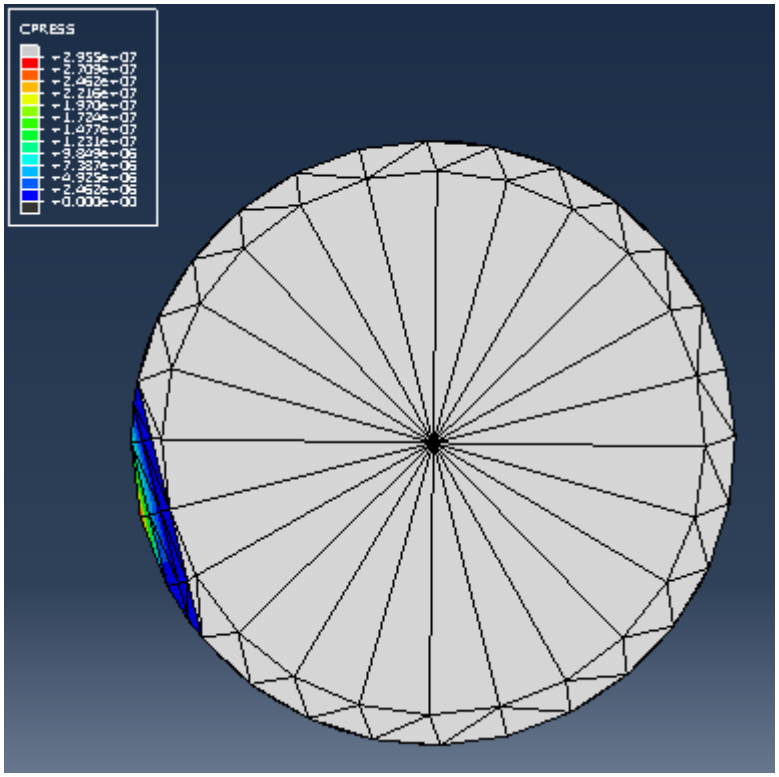

Figure 8.73 - Tetrahedral mesh, 10% Shaft fracture at 500 rad/s, step time: 0,95 s

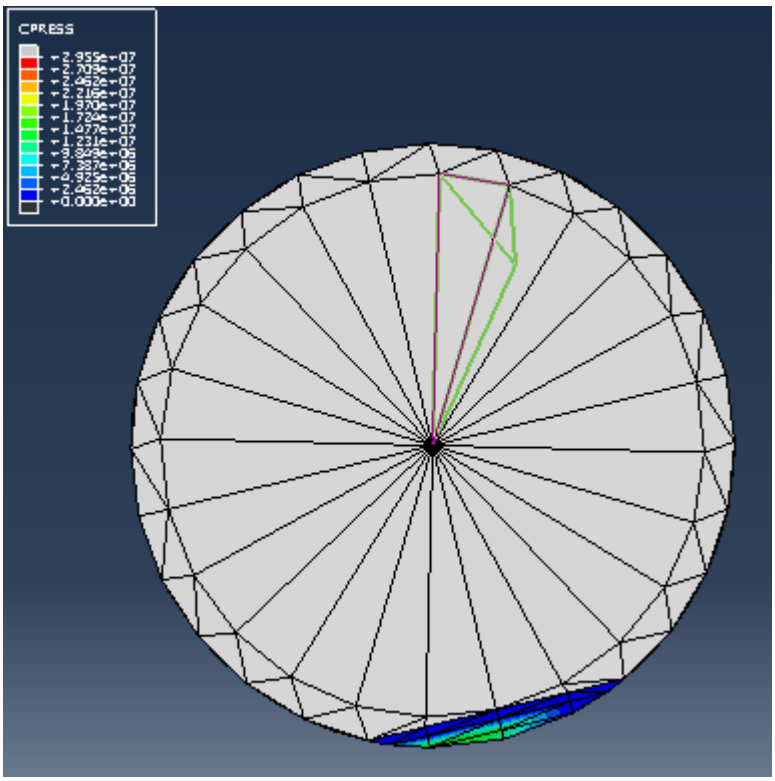

Figure 8.74 - Tetrahedral mesh, 10% Shaft fracture at 500 rad/s, step time: 1,0 s

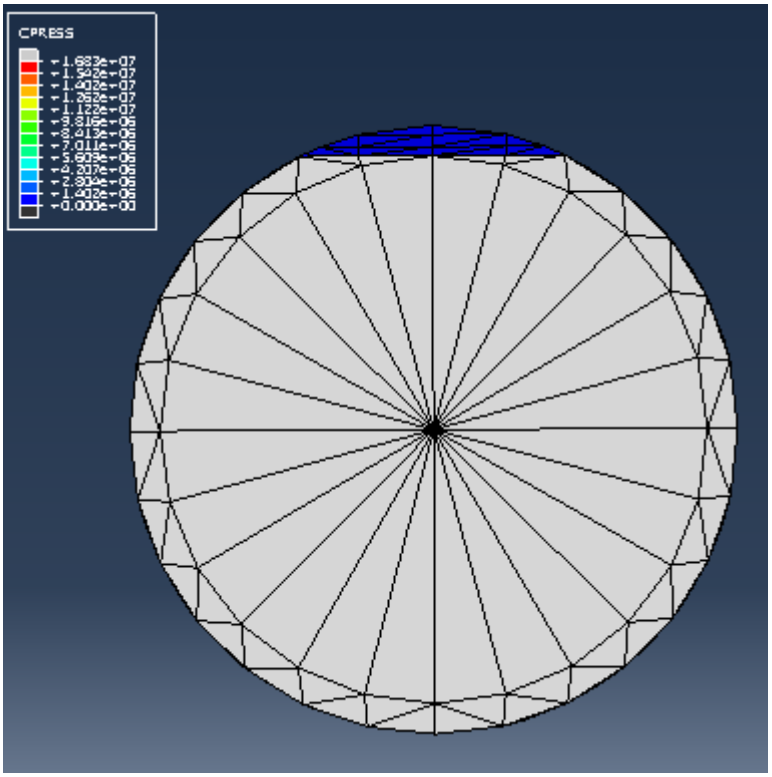

Figure 8.75 - Tetrahedral mesh, 10% Shaft fracture at 1000 rad/s, step time: 0,0 s

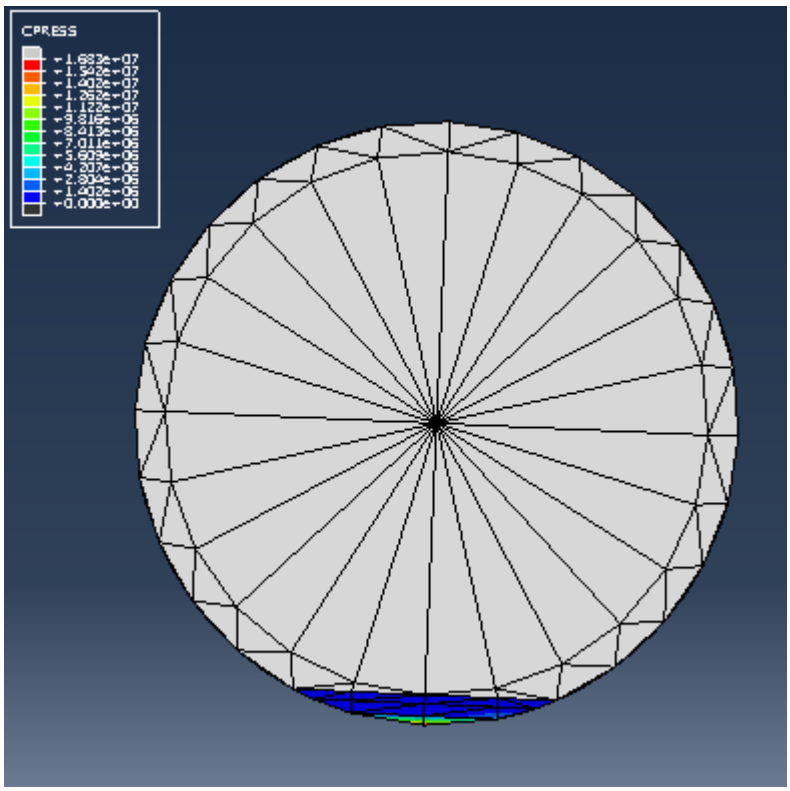

Figure 8.76 - Tetrahedral mesh, 10% Shaft fracture at 1000 rad/s, step time: 0,20 s

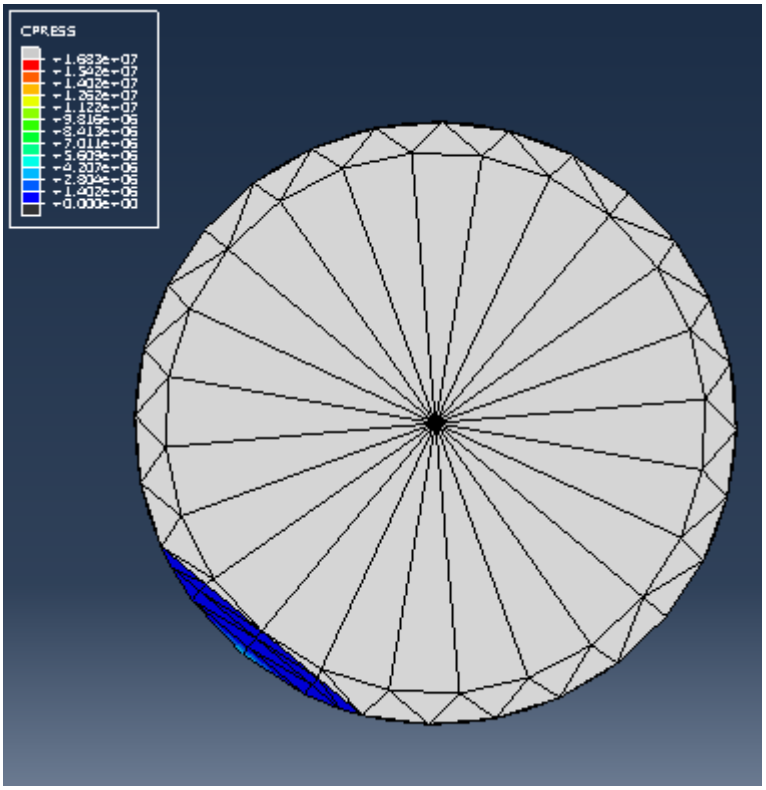

Figure 8.77 - Tetrahedral mesh, 10% Shaft fracture at 1000 rad/s, step time: 0,30 s

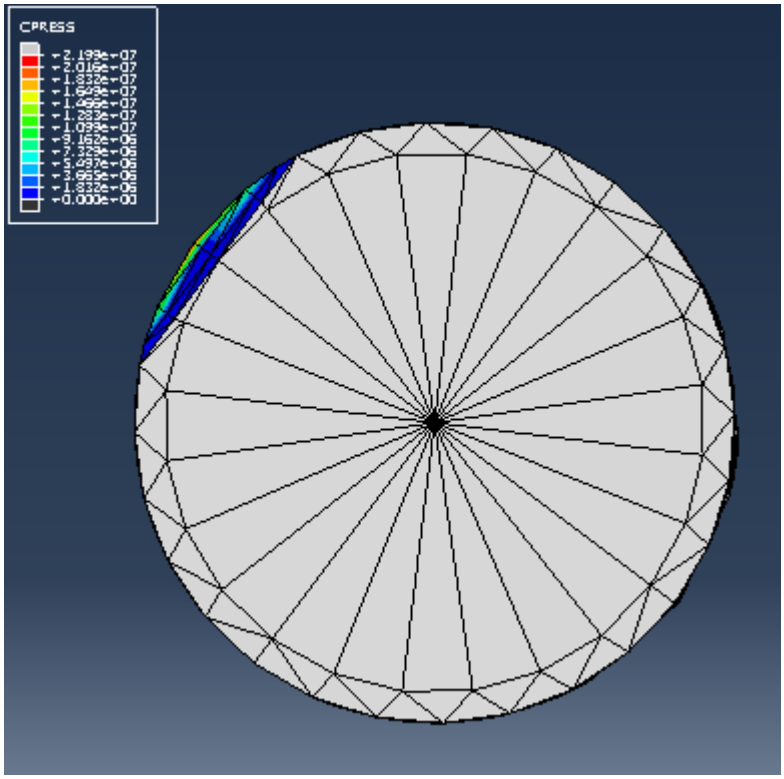

Figure 78 - Tetrahedral mesh, 10% Shaft fracture at 1000 rad/s, step time: 0,35 s

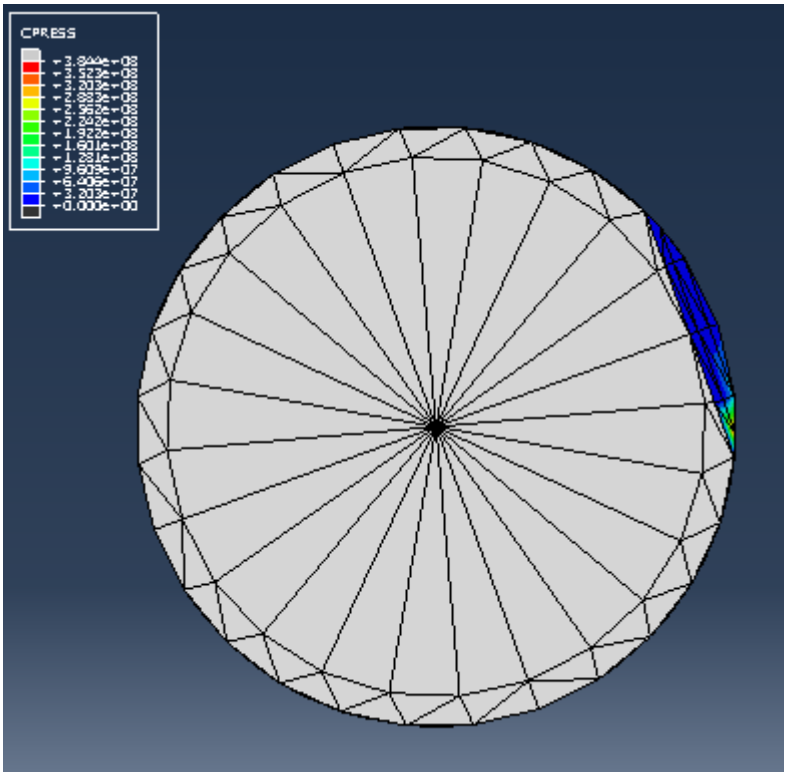

Figure 8.79 - Tetrahedral mesh, 10% Shaft fracture at 1000 rad/s, step time: 0,40 s

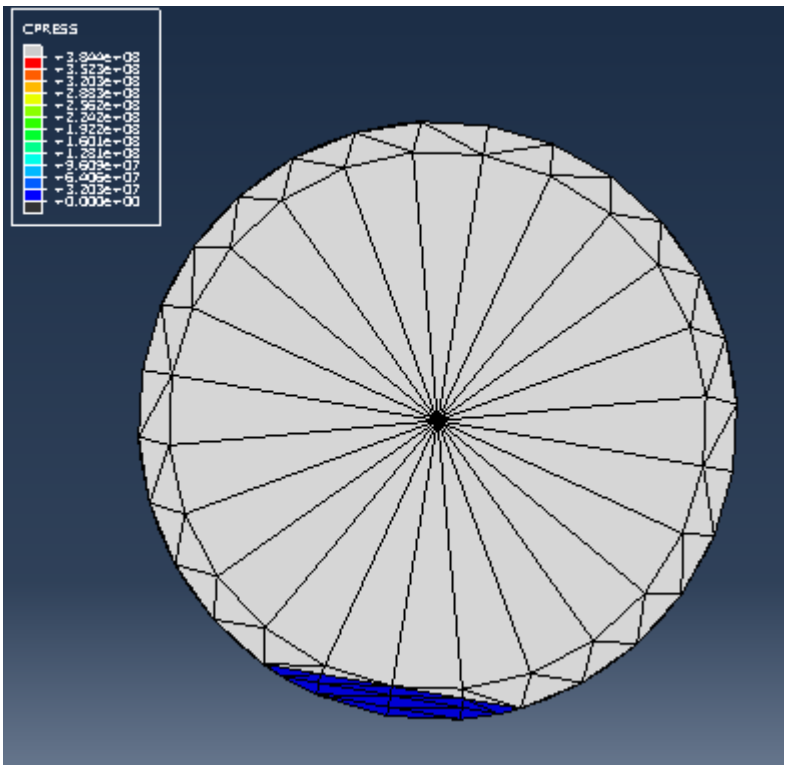

Figure 8.80 - Tetrahedral mesh, 10% Shaft fracture at 1000 rad/s, step time: 0,45 s